PROBING THE EXTREME ENVIRONMENT OF THE GALACTIC CENTER WITH SOFIA/FORCAST

A Dissertation

Presented to the Faculty of the Graduate School

of Cornell University

in Partial Fulfillment of the Requirements for the Degree of

Doctor of Philosophy

by

Ryan Lau

August 2014

PROBING THE EXTREME ENVIRONMENT OF THE GALACTIC CENTER WITH SOFIA/FORCAST

Ryan Lau, Ph.D.

Cornell University 2014

Within the inner 100 pc of the Milky Way Galaxy lies the supermassive black hole, Sgr A*, regions of recent star formation, and 3 young, massive stellar clusters: the Central, Quintuplet, and Arches clusters. In this thesis I will present images of the Circumnuclear Ring, the twin Luminous Blue Variable nebulae in and near the Quintuplet Cluster, and the Sgr A East HII Region Complex taken by the Faint Objected Infrared Camera for the SOFIA Telescope (FORCAST).

The Circumnuclear Ring (CNR) is the inner edge of the molecular torus orbiting Sgr A* with a radius of 1.4 pc. The CNR exhibits features of a classic H II region and appears consistent with the prevailing paradigm in which the dust is heated by the Central cluster of hot, young stars. We find that clumps within the ring are not dense enough to be stable against tidal shear from Sgr A* and will be sheared out before completing a full orbit ($\sim 10^5$ yrs).

Three Luminous Blue Variables (LBVs) are located in and near the Quintuplet Cluster 40 pc in projection from Sgr A*: qF362, the Pistol star, G0.120-0.048 (LBV3). Our images reveal the asymmetric, compressed shell of hot dust surrounding the Pistol Star and provide the first detection of the thermal emission from the symmetric, hot dust envelope surrounding LBV3. However, no detection of hot dust associated with qF362 is made. We argue that the Pistol star and LBV3 are identical "twins" that exhibit contrasting nebulae due to the external influence of their different environments.

G-0.02-0.07, a complex consisting of three compact HII regions (A, B, and C) and one ultracompact HII region (D), is located at the edge of a molecular cloud 6 pc in projection to the east of Sgr A* and contains the most recent episode of star formation in the inner 10 pc of the Galactic center ($\lesssim 10^5$ yrs). We probe the dust morphology, energetics, and composition of the regions to study the young stellar objects and the surrounding dense molecular cloud. The location of the heating source for region A is determined by triangulation from distances and temperatures derived from fits to spectral energy distributions of three different points around the region, and is found to be displaced to the northeast of the center of curvature near the color temperature peak. Based on total luminosities, expected 1.90 μm fluxes, and proximity to the mid-IR color temperature peaks we identify heating source candidates for regions A, B, and C.

We present imaging at 19, 25, 31, and 37 μm of the compact HII region complex G-0.02-0.07 located 6 pc in projection from the center of the Galaxy obtained with SOFIA using FORCAST. G-0.02-0.07 contains three compact HII regions (A, B, and C) and one ultra-compact HII region (D). Our observations reveal the presence of two faint, infrared sources located 23" and 35" to the east of region C (FIRS 1 and 2) and detect dust emission in two of the three "ridges" of ionized gas west of region A. The 19/37 color temperature and 37 μm optical depth maps of regions A - C are used to characterize the dust energetics and morphology. Regions A and B exhibit average 19/37 color temperatures of $\sim$ 105 K, and regions C and D exhibit color temperatures of $\sim$ 115 K and $\sim$ 130 K, respectively. Using the DustEM code we model the SEDs of regions A - D and FIRS 1, all of which require populations of very small, transiently heated grains and large, equilibrium-heated grains. We also require the presence of polycyclic aromatic hydrocarbons (PAHs) in regions A - C in order to fit the 3.6, 4.5, 5.8, and 8.0 μm fluxes observed by *Spitzer/IRAC*. The location of the heating source for region A is determined by triangulation from distances and temperatures derived from DustEM models fit to SEDs of three different points around the region, and is found to be displaced to the northeast of the center of curvature near the color temperature peak. Based on total luminosity, expected 1.90 μm fluxes, and proximity to the mid-IR color temperature peaks we identify heating source candidates for regions A, B, and C. However, for region D, the observed fluxes at 1.87 and 1.90 μm of the previously proposed ionizing star are a factor of $\sim$ 40 times too bright to be the heating source and hence is likely just a star lying along the line of sight towards region D.

BIOGRAPHICAL SKETCH

Ryan Lau was born and raised in Honolulu, Hawaii on January 21, 1988. At a young age, Ryan enjoyed watching ants crawl up and down trees, telling random strangers his name was "Dumbo," and throwing frequent tantrums when his favorite foods were not readily available. Fortunately, only one of these activities has followed him into adulthood. In his youth, he became interested in skateboarding, video games, and playing the guitar. He dreamed of pursuing a career as an electrical engineer, which was his father's career. Despite initially thinking the job entailed of running electric trains, Ryan heavily focused on his studies of math and science.

After graduating from 'Iolani School in Hawaii, Ryan chose to migrate across the Pacific Ocean to attend Reed College in Portland, OR, where he majored in physics. It was in the gradeless environment of Reed that Ryan truly began to appreciate the satisfaction that came with learning for the sake of learning; it should also be noted that having his parents cover the entirety of the $\sim$ \$40000 yearly tuition throughout all four years helped with this appreciation. The spark that ignited Ryan's interested in focusing on astronomy occurred in a passing conversation with a colleague where it was pointed out to him that "astronomy is a pretty cool field." After taking a class on astrophysics in his junior year, he participated in the National Science Foundation's (NSF) Research Experiences for Undergraduates (REU) program at the Cornell University Department of Astronomy.

Ryan chose to attend Cornell University for graduate school in Astronomy, where he was at the top of his class (which consisted of only himself). In the spring of his first year he joined Prof. Terry Herter's group using the Cornell-built Faint Object Infrared Camera for the SOFIA Telescope (FORCAST) to pur-

sue observational, infrared astronomy. Within several weeks of joining the group, he was flying aboard the Stratospheric Observatory for Infrared Astronomy (SOFIA) and participating in observations of the Galactic center. For the remainder of his graduate career, Ryan studied the Galactic center and worked with FORCAST and SOFIA. After receiving his PhD, Ryan will continue working with the FORCAST group as a postdoctoral researcher to expand on his interests in the Galactic center and infrared astronomy.

This thesis is dedicated to family, friends, and Lyann.

ACKNOWLEDGEMENTS

I would like to acknowledge some of the many people whose support and companionship have driven my academic pursuits and have played an influential role in the completion of this thesis.

To Mom, Dad, and family - You've always been there for me and have helped keep me motivated and driven to realize all of my goals and dreams–for that I can't thank you enough.

To Prof. Johnny Powell - I don't think I would have realized my potential as a student of physics and astronomy if it wasn't for your enthusiasm and direction. I hope our paths continue to cross in the future.

To Prof. Terry Herter - Looking back on the past for years I can see how much I've grown and matured as a scientist under your guidance. Thank you for your patience and for always being available whenever I needed help. I very much look forward to working together in the future.

To Prof. Mark Morris - You've been a second advisor to me throughout my entire graduate school career. Thank you for always making time to talk with me and for all of your valuable insight on our work.

To Prof. Gordon Stacey - Thank you for giving me the opportunity to work with the ZEUS-II group as an REU and for giving me my first chance to participate in research.

To the Astronomy grad students (and the other cool ones) - The community here is truly amazing–I don't think my graduate school experience would have been the same without all the TGIFs, GSPSs, BBQs in 50° F weather, and hiking/camping/city trips that we've done. I'd also like to thank the Moment Generator bandmates (Patrick, Greg, and Ben) and also our former bandmates (Steve, Dan, and Mik) for making such awesome music.

To the FORCAST Team: Terry, George, Chuck, Justin, Joe, Luke, and Matt - Thank you for answering all of my questions on the instrument and SOFIA and for being with me on all of those SOFIA flights and trips out to Palmdale. It has definitely been a very enlightening and awesome experience being a part of this group and getting the opportunity to participate in such a project.

To SOFIA Mission Ops and EPO - Thank you all for the amazing opportunities you've given me, I've had a great time working with everyone in the SOFIA community (and hope to continue to do so!). Eric Becklin, I was very honored to have worked with you on our Galactic center observations of the Circumnuclear Ring–thank you for all the support and guidance. Coral, Pamela, and Dana, thank you for giving me the chance to meet up with truly wonderful educators, they're stories continue to inspire me and drive me to become a better teacher.

Last but not least, to Lyann - I can't express how grateful I feel to have had you by my side throughout all of these years. You've always had my back, and you can be certain I'll always have yours.

This work is based on observations made with the NASA/DLR Stratospheric Observatory for Infrared Astronomy (SOFIA). SOFIA science mission operations are conducted jointly by the Universities Space Research Association, Inc. (USRA), under NASA contract NAS2-97001, and the Deutsches SOFIA Institut (DSI) under DLR contract 50 OK 0901. Financial support for FORCAST was provided by NASA through award 8500-98-014 issued by USRA.

TABLE OF CONTENTS

LIST OF TABLES

LIST OF FIGURES

CHAPTER 1

INTRODUCTION

1.1 The Center of the Milky Way Galaxy

Located 8000 pc away from us lies the center of our Milky Way Galaxy which consists of regions of recent, massive star formation, a turbulent interstellar medium, and most notably the 4 million solar mass supermassive black hole, Sgr A* (Morris & Serabyn 1996). What makes the Galactic center (GC) of great interest to us is that it is the closest Galactic nucleus, and it provides us with a standard with which we can use to study the environments of the centers of other galaxies. The GC region has been intensely studied at infrared (IR), sub-millimeter, and radio wavelengths due to intervening gas and dust that gives rise to $\sim$ 40 magnitudes of visual extinction, which makes it nearly impossible to observe in the optical and ultraviolet (UV). The region typically described as the GC is the inner $\sim$ 500 pc of the Galaxy; however, in this thesis, I primarily focus on the inner $\sim$ 60 pc, where the environment is most extreme due to the influence of the massive, young stellar clusters and Sgr A*.

The GC emits brightly in the IR due to the intense radiation field from the young, massive stars illuminating dust (Simpson et al. 1997; Lang, Goss, & Wood 1997; Latvakoski et al. 1999; Lang et al. 2001). This thermal dust emission provides an excellent probe of the stellar heating in the region and allows us to characterize the hot, young stars and their interaction with the surrounding medium. Again, significant extinction at shorter wavelengths makes it difficult to directly study the properties of these stars.

1.1.1 Airborne Astronomy

Ground-based observations in the IR face the challenge of overcoming the fluctuating emission from the atmosphere as well at the telluric absorption bands that make it nearly impossible to observe at a range of IR and sub-millimeter wavelengths. Space-based telescopes alleviate issues caused by Earth's atmosphere but typically have a fixed suite of instruments and a finite lifetime. Airborne astronomy, while not capable of achieving space-based sensitivities, provides a way to overcome atmospheric absorption due to water vapor to interchange instrumentation. SOFIA, the Stratospheric Observatory for Infrared Astronomy, is the only operating airborne observatory and has the largest primary mirror ($\sim$ 2.5 m) ever utilized for airborne astronomy. SOFIA is a joint project between NASA and the German Aerospace Center (DLR) and is currently operated and managed by the Universities Space Research Association (USRA).

The first-light instrument on SOFIA was the Cornell-built Faint Object Infrared Camera for the SOFIA Telescope (FORCAST; Herter et al. 2012). Rather than redundantly overlap with the observing capabilities of the Spitzer and Herschel space telescopes, SOFIA with FORCAST is able to perform observations of bright IR regions, which are unobservable by Spitzer due to saturation issues, at wavelengths shorter than those accessible by Herschel. SOFIA's primary mirror also has a diameter three times that of Spitzer's, which provides SOFIA with higher angular resolution in the far-IR where SOFIA is diffraction-limited. Spitzer and Herschel are no longer operating at full capacity due to their cryogens being exhausted; therefore, SOFIA is and will be the only observatory capable of observing in the mid to far-IR until the launch of JWST (scheduled for Oct. 2018).

1.1.2 Thesis Organization

In this thesis, I study the environment of three dusty regions contained in the inner ~ 60 pc of the GC by observing and analyzing the warm dust emission at IR wavelengths. The main purpose of the observations is to use the thermal emission from dust as a diagnostic for characterizing the stellar heating sources and studying the turbulent environment of the GC that is affected by the strong Galactic tidal force. The GC objects addressed are the Circumnuclear Ring (CNR), the clumpy ring of hot dust and gas surrounding Sgr A*, "twin" luminous blue variable (LBV) nebulae in and near the Quintuplet Cluster, and the Sgr A East HII regions, a site of the most recent event of star formation within the inner 10 pc of the GC.

In chapter 2, I discuss the observations of the dust emission from the CNR, which capture the structure at the highest spatial resolution in the far-IR. This work on the CNR focuses on characterizing its morphology, searching for evidence of star formation within it, and studying its interaction with the Galactic tidal forces. Chapter 3 addresses the observations of "twin" LBV nebulae associated with the Pistol star (Figer et al. 1995) and G0.120-0.048 (Mauerhan et al. 2010). Near-IR spectroscopy reveal similar emission lines from both LBVs (Figer et al. 1999; Najarro et al. 2009) suggesting they are similar in nature; however, their nebulae exhibit contrasting appearances. Although the dust and ionized gas emission reveals that both nebulae have similar size scales, the Pistol nebula is bright and asymmetric about the central star, whereas the G0.120-0.048 nebula is dim and circularly symmetric. Images of the dust emission from the nebulae help to reveal the cause of their contrasting nature. In chapter 4, I examine the Sgr A East HII regions in order to study the young stars illuminating

dust in the associated dense molecular cloud and to search for signs of young stellar objects. Models of the dust emission are fit to the observed spectral energy distributions of the HII regions to analyze the dust composition, mass, and temperature. In chapter 5, I summarize the collection of work presented in this thesis and provide my insight on future IR studies of the Galactic center.

1.2 An Infrared Astronomer's Tool-belt

Dust provides an excellent diagnostic for studying the heating conditions in molecular clouds or dust-enshrouded regions that obscure the emission from stars. Such dust-enshrouded stars may be nearly impossible to observe in the visible and ultraviolet (UV) due to the efficiency of dust absorption at those wavelengths. Dust will, however, thermally re-radiate the absorbed visible and UV radiation in the IR ($\sim 1 - 1000\ \mu$m) thus allowing astronomers to probe environments such as molecular clouds adjacent to young stars or dusty shells expelled from massive, evolved stars. In this section, I will go through an introduction on the properties of astrophysical dust and discuss the essential "tools" for an astronomer studying thermal dust emission. The content of this section is by no means a complete compilation on dust analysis techniques (I have omitted the discussion of dust polarization and the effects of non-sphericity), but rather focuses on the observational and theoretical analysis techniques utilized throughout this thesis.

1.2.1 Optical Properties of Astrophysical Dust

Dust plays a very important role in astronomical studies from galactic to extra-galactic scales. In our Galaxy, dust absorbs ~ 30% of the total starlight and re-radiates this emission in the IR (Bernstein et al. 2002). It is therefore important to understand the way light interacts with these dust grains and the manner in which these grains re-emit. Throughout this thesis I will assume dust grains are spherical since I will not focus on the consequences of non-sphericity like polarization. Each grain will have a geometric cross-section, $\sigma_{\rm geo}$, of

$$\sigma_{\rm geo} = \pi a^2, \tag{1.1}$$

where a is the radius of the grain. A dust grain will interact with light of a wavelength, λ, with the following extinction cross-section

$$C_{\rm ext}(\lambda; a, \epsilon) = C_{\rm abs} + C_{\rm sca}, \tag{1.2}$$

where $C_{\rm abs}$ and $C_{\rm sca}$ are the absorption and scattering cross-sections of a dust grain, which is a value that depends on the complex dielectric function of the of the grain, ϵ, the grain size, and the wavelength of light it interacts with. It is useful to define dimensionless scattering, and absorption efficiency factors as follows:

$$Q_{\rm ext}(\lambda; a, \epsilon) = \frac{C_{\rm ext}}{\sigma_{\rm geo}},\ Q_{\rm sca}(\lambda; a, \epsilon) = \frac{C_{\rm sca}}{\sigma_{\rm geo}},\ Q_{\rm abs}(\lambda; a, \epsilon) = \frac{C_{\rm abs}}{\sigma_{\rm geo}}. \tag{1.3}$$

The optical depth, which characterizes the attenuation of radiation at wavelength, λ, due to scattering and absorption from dust grains of density, n_d, along a line of sight, can be written as

$$\tau_{\rm d}(\lambda; a, \epsilon) = \int n_{\rm d}\, Q_{\rm ext}\, \sigma_{\rm geo}\, dl. \tag{1.4}$$

Much of the physics of the dust grain's interaction with light is captured in the complex dielectric function, ϵ, which can expressed in terms of the real and complex coefficients,

$$\epsilon(\lambda) = \epsilon_1 + i\epsilon_2. \tag{1.5}$$

The real part of the dielectric function, ϵ_1, characterizes the refractive index of the grain, and the complex part, ϵ_2, describes the damping of an electromagnetic wave through the grain. A purely scattering grain will therefore only have a real component of the dielectric function, whereas a purely absorbing grain will only have a complex component.

There are three important wavelength regimes as light interacts with a dust grain: $\lambda >> a$, $\lambda \sim a$, and $\lambda << a$. The first two of these regimes are particularly important for this thesis since much of the observations are of infrared dust emission heated by stellar sources. In the large wavelength limit ($\lambda >> a$), $Q_{\rm abs} \propto \lambda^{-2}$ and $Q_{\rm sca}$ can be characterized by Rayleigh scattering, $Q_{\rm sca} \propto \lambda^{-4}$; therefore, as long as the dust grain is not composed of a highly reflective material, absorption will dominate for large wavelengths and $\tau_{\rm d} \propto \lambda^{-2}$ (Draine 2011). For wavelengths of light that are comparable to the size of a dust grain such as optical and UV, Mie theory is required to describe the absorption and scattering (Mie 1908, Debye 1909). Solutions provided by Mie theory show that both $Q_{\rm abs}$ and $Q_{\rm sca}$ approach ~ 1 as $2\pi a/\lambda \rightarrow \infty$ and decrease sharply towards longer wavelengths. Grains with strong scattering will have $Q_{\rm abs}$ and $Q_{\rm sca}$ exhibit oscillatory behavior due to constructive and destructive interference between the transmit-

ted and diffracted light. At the high-energy, short-wavelength limit both the real and imaginary values of the dielectric function are very small and the light is primarily forward-scattered which results in a drop in $Q_{\rm ext}$ towards very short wavelengths such as x-ray (Draine 2003).

1.2.2 Observational Analysis Techniques and Tools

A majority of the work performed in this thesis is based on multi-wavelength spatially-resolved observations of continuum dust emission. These observations can directly probe the column density and temperature of the emitting dust grains. If the grain composition and size distribution is known then it is possible to estimate the total mass of the emitting dust. In this section, I discuss how our theoretical understanding of dust and radiative transfer can be directly applied to IR photometric observations of dust emission.

Color Temperature and Optical Depth

If the flux from a warm, dusty source is observed in at least two different wavelengths, such as 19 and 37 μm, it is possible to determine the color temperature and optical depth of the emitting dust. Both of these values are derived from the solution to the radiative transfer equation for "slab" in local thermodynamic equilibrium (LTE) with no incident radiation, which is a reasonable approximation in most cases of studying dust emission. The intensity of the observed dust emission, I_ν, can therefore be expressed as

$$I_\lambda = B_\lambda(T_\mathrm{d})(1 - e^{-\tau_\mathrm{d}(\lambda)})e^{-\tau_\mathrm{ISM}(\lambda)}, \tag{1.6}$$

where T_d, τ_d, and τ_ISM are the emitting dust temperature and optical depth, and the optical depth of the intervening material in the interstellar medium (ISM), respectively. If the emission can be approximated as optically thin and the extinction towards the source is known, Eq. 1.6 can be simplified to

$$I_\lambda \sim \tau_\mathrm{d}(\lambda)\, B_\lambda(T_\mathrm{d}). \tag{1.7}$$

At long wavelengths ($\lambda >> a$) and for a fixed grain size the optical depth, τ_d can be approximated as a power-law in wavelength (or frequency): $\tau_\mathrm{d} \propto \lambda^{-\beta}$, where β is typically taken to be 2 (Draine 2011). If observations are taken of the dusty source at wavelengths of λ_1 and λ_2, the dust temperature can then be solved by taking the ratio of the emission at λ_1 and λ_2:

$$\frac{I_{\lambda_1}}{I_{\lambda_2}} = \left(\frac{\lambda_1}{\lambda_2}\right)^{-2} \frac{B_{\lambda_1}(T_\mathrm{d})}{B_{\lambda_2}(T_\mathrm{d})}. \tag{1.8}$$

The temperature, T_d, derived from this method is known as the color temperature. The color temperature is most useful as a diagnostic for constraining the dust temperature when the two observed wavelengths sample the near the Wien and Rayleigh-Jeans sides of the modified, power-law blackbody peak (e.g. imaging a $\sim$ 100 K source at 19 and 37 μm).

For extended dust emission detected with an adequate signal-to-noise ratio (SNR), a map of color temperatures can be generated by solving for T_d via Eq. 1.8 at each spatial pixel element in the images at λ_1 and λ_2. It is important to note that both images must be convolved to have an identical point-spreaad function

(PSF) in order to produce accurate color temperatures. Color temperature maps of a dusty region that exhibit peaks and/or gradients can signal the presence of embedded sources or identify the location of the sources responsible for dust heating. For example, if a star is located at the center of a spatially-resolved dusty shell heated primarily by the radiation field of the star the color temperature map would reveal an azimuthal symmetry around the shell; however, if the star were offset to the northern edge of the shell the color temperature map would capture the gradient of the temperature decreasing from north to south.

With the color temperature and the intensity at a wavelength, λ, the optical depth at λ of the emitting dust can be derived from Eq. 1.7. For small optical depths, an optical depth map can be generated from the color temperature map and intensity maps by evaluating

$$\tau_{\rm d}(\lambda) = \frac{F_\lambda}{\Omega_p \, B_\lambda(T_{\rm d})} \tag{1.9}$$

at each pixel position, where Ω_p is the solid angle subtended by a pixel. An optical depth map directly traces the column density of emitting dust and can reveal the presence of density clumps, ridges, or gradients that might provide evidence on the interaction of the dust with its environment. When producing an optical depth map it is essential to be aware of what region of a dusty structure the emission at a wavelength, λ, is tracing. In this thesis, most of the observations are taken at wavelengths that trace the emission from hot ($\sim$ 100 K) dust at the HII and photo-dissociation regions of molecular clouds; therefore, the optical depth maps we generate are unlikely to account for all of the dust in the associated with the sources we detect.

Estimating Dust Mass

Total dust mass estimates can be derived with information on the color temperature, flux, composition, and size of the emitting dust grains. The flux from a dusty source located at a distance, d, from us can be written in terms of the total number of dust grains, $N_{\rm d}$ as

$$F_\lambda = N_{\rm d} \frac{Q_{\rm abs}(\lambda)\, \pi a^2 B_\lambda(T_{\rm d})}{d^2}. \tag{1.10}$$

If we assume that the dust grains have a uniform grain size of a, the total dust mass is simply

$$M_{\rm d} = (4/3)\pi a^3 \rho_{\rm b}\, N_{\rm d}, \tag{1.11}$$

where $\rho_{\rm b}$ is the bulk density of the dust grains; $\rho_{\rm b} \sim 2$ and 4 g cm^{-3} for graphite and silicate grains, respectively. Eq. 1.10 and 1.11 can be combined to provide the following expression for total dust mass:

$$M_{\rm d} = \frac{(4/3)\, a\, \rho_{\rm b}\, F_\lambda\, d^2}{Q_{\rm abs}(\lambda) B_\lambda(T_{\rm d})}. \tag{1.12}$$

As an example, let's say we detect the warm dust emission from a nebula located 8000 pc away in the Galactic center (Reid et al. 1993) at 19 and 37 μm, where $F_{19} = 10$ Jy and $F_{37} = 15$ Jy. Solving for the color temperature (Eq. 1.8) yields $T_d \sim 100$ K. Assuming this nebula is composed of 0.1 μm-sized silicate dust, the absorption efficiency at 19 (or 37) μm is ~ 0.05 (~ 0.01; Draine 2011) and its total dust mass can then be estimated from Eq. 1.12 to be $\sim 10^{-3}$ M$_\odot$.

1.2.3 Theoretical Analysis Techniques and Tools

The observational analysis techniques discussed in the previous section provide a wealth of insight into the properties of the emitting dust; however, gaining a deeper understanding of the dust and its surrounding environment requires us to substantiate these observational results with theory. In this section, I discuss the heating of dust from stellar radiation fields and how the nature of this heating differs between large ($a \sim 1000\,\text{Å}$) and very small ($a < 100\,\text{Å}$) grains. Dust can also be collisionally heated, which can dominate over radiative heating in the cores of dense molecular clouds or in the shock-heated environments of supernova remnants. In the environment of an HII region ($n_\text{e} \sim 1 - 10^4$ cm^{-3}, $T_e \sim 10^4$ K), which are studied in this thesis, collisional heating is negligible compared to radiative heating.

Dust Equilibrium Temperature

The total power absorbed by a dust grain of radius, a, heated by a stellar source with a luminosity L_*, is given by

$$P_\text{abs} = \int_\lambda Q_\text{abs}(\lambda)\,\pi a^2 \frac{L_*(\lambda)}{4\pi\, d^2} d\lambda. \tag{1.13}$$

Assuming that the emission from the star can be approximate as a blackbody, Eq. 1.13 can be rewritten as

$$P_\text{abs} = \int_\lambda Q_\text{abs}(\lambda)\,\pi a^2 \frac{R_*^2}{d^2} \pi\, B_\lambda(T_*) d\lambda, \tag{1.14}$$

where R_* and T_* are the radius and effective temperature of the star. For the sake of convenience we can define a stellar spectrum-averaged absorption efficiency,

$$\langle Q \rangle_* = \frac{\int Q_{\rm abs}(\lambda)\, \pi\, B_\lambda(T_*) d\lambda}{\int \pi\, B_\lambda(T_*) d\lambda}, \tag{1.15}$$

which allows us to express Eq. 1.14 simply as

$$P_{\rm abs} = \langle Q \rangle_*\ \pi a^2 \frac{R_*^2}{d^2} \sigma_{\rm SB} T_*^4. \tag{1.16}$$

Typical values of $\langle Q \rangle_*$ are on the order of unity for hot O and B-type stars and $\sim 0.1\ \mu$m-sized grains since the peak emission wavelength of the stellar continuum will lie in the Mie-scattering regime of the dust (i.e. $Q_{\rm abs}(\lambda_{\rm peak}) \sim 1$).

The rate at which a dust grain at a temperature, $T_{\rm d}$, loses energy by emitting in the infrared can be expressed as

$$P_{\rm em} = \int_\lambda 4\pi\, B_\lambda(T_{\rm d}) Q_{\rm abs}(\lambda)\, \pi a^2 d\lambda. \tag{1.17}$$

Note that I have written Eq. 1.17 in terms of $Q_{\rm abs}$ instead of $Q_{\rm em}$; this is because of Kirchoff's Law which implies $Q_{\rm abs} = Q_{\rm em}$. Similar to $\langle Q \rangle_*$, we define a dust-averaged emission efficiency,

$$\langle Q \rangle_{\rm d} = \frac{\int Q_{\rm abs}(\lambda)\, \pi\, B_\lambda(T_{\rm d}) d\lambda}{\int \pi\, B_\lambda(T_{\rm d}) d\lambda}, \tag{1.18}$$

The majority of the emission from dust found at temperature $T_{\rm d} \lesssim 300$ K will primarily arise from infrared or redder wavelengths. At these wavelengths, $\lambda > a$ and $Q_{\rm abs}(\lambda)$ can then be approximated as a power-law: $Q_{\rm abs}(\lambda) \propto \lambda^{-2}$ (Draine 2011). Substituting the power-law approximation for $Q_{\rm abs}(\lambda)$ in Eq. 1.18 and evaluating the integrals reveals that $\langle Q \rangle_{\rm d} \propto T_{\rm d}^2$. We can therefore define a non-temperature dependent dust-averaged emission coefficient as

$$\langle Q \rangle'_{\rm d} = \langle Q \rangle_{\rm d}\ T_{\rm d}^{-2}. \tag{1.19}$$

Now, we can combine Eq. 1.19 and 1.17 and express $P_{\rm em}$ as

$$P_{\rm em} = \langle Q \rangle'_{\rm d}\, 4\pi a^2 \sigma_{\rm SB} T_{\rm d}^6. \tag{1.20}$$

Assuming that the dust grain is in thermal equilibrium, the heating and cooling is balanced and Eq. 1.16 and 1.20 can be equated to provide an equilibrium dust temperature, $T_{\rm eq}$,

$$T_{\rm eq} = \left(\frac{\langle Q \rangle_*}{\langle Q \rangle'_{\rm d}} \frac{R_*^2\, T_*^4}{4\, d^2} \right)^{1/6} = \left(\frac{\langle Q \rangle_*}{\langle Q \rangle'_{\rm d}} \frac{L_*}{16\pi\, \sigma_{\rm SB}\, d^2} \right)^{1/6}. \tag{1.21}$$

Note that this temperature is essentially independent of grain size since $\langle Q \rangle_*$ and $\langle Q \rangle'_{\rm d}$ are roughly proportional to a. Keep in mind that Eq. 1.21 will break down when the heating source is too cool due to our assumptions on $\langle Q \rangle_*$ that the radiation at peak of the stellar emission lies in the Mie-scattering regime of the grain; it will also break down when the grain is too hot ($T_{\rm d} \gtrsim 200$ K) due to our assumptions on $\langle Q \rangle'_{\rm d}$ that the peak wavelength of the dust emission is much larger than the grain size.

Let's go back to our example at the end of Sec. 1.2.2 with the 100 K Galactic center source. An O-type star with a luminosity of $\sim 10^5$ $L_\odot$ is found to be located ~ 0.1 pc away from the 100 K dust–could this be the heating source? For an O-type star, $\langle Q \rangle_* \sim 1$, and assuming a uniform distribution of 0.1 μm-sized silicate grains $\langle Q \rangle'_{\rm d} \sim 1.3 \times 10^{-6}\ {\rm K}^{-2}$ (Draine 2011). Substituting these values into Eq. 1.21 reveals that $T_{\rm eq} \sim 100$ K, which is strongly suggestive that this O-star is indeed the heating source.

Stochastic Heating of Very Small Grains

In the previous section, we made the assumption that the illuminated dust grains are in thermal equilibrium with the radiation from the stellar heating source. This assumption is reasonable for large grains, since they have a large absorption cross-section and are struck by UV and optical photons frequently enough that they will not cool significantly in-between photon hits. Very small grains ($a \sim 10 - 100$ Å), however, have a much smaller absorption cross section as well as a much lower heat capacity, C_V, since $C_V \propto N$, where N is the total number of atoms composing the grain. The combination of these effects results in large temperature excursions far below and above the equilibrium temperature since the grain will be hit less frequently, which allows for sufficient time for cooling, and because a single UV or optical photon absorption will produce a significant increase in temperature due to its small specific heat.

In order to characterize the emission of small, transiently-heated grains, it is necessary to define a probability distribution function (PDF) for its temperature, dP/dT, where $P(T)$ is the probability that a dust grain will exhibit a temperature equal to or less than T. dP/dT can be derived through numerical simulations (Draine & Anderson 1985) or solved for directly (Guhathakurta & Draine 1989; Draine & Li 2001). Fig. 1.1 shows the PDF for small (red lines) and large (blue lines) grains as a function of temperature for dust located 0.1 (solid lines) and 0.5 (dotted lines) pc from a 10^5 $L_\odot$ and 35000 K heating source. The temperature PDF for large grains is essentially a delta function at the equilibrium temperature since it will not experience significant temperature fluctuations, whereas the PDF for small grains is much broader and includes higher temperatures ($\gtrsim$ 500 K).

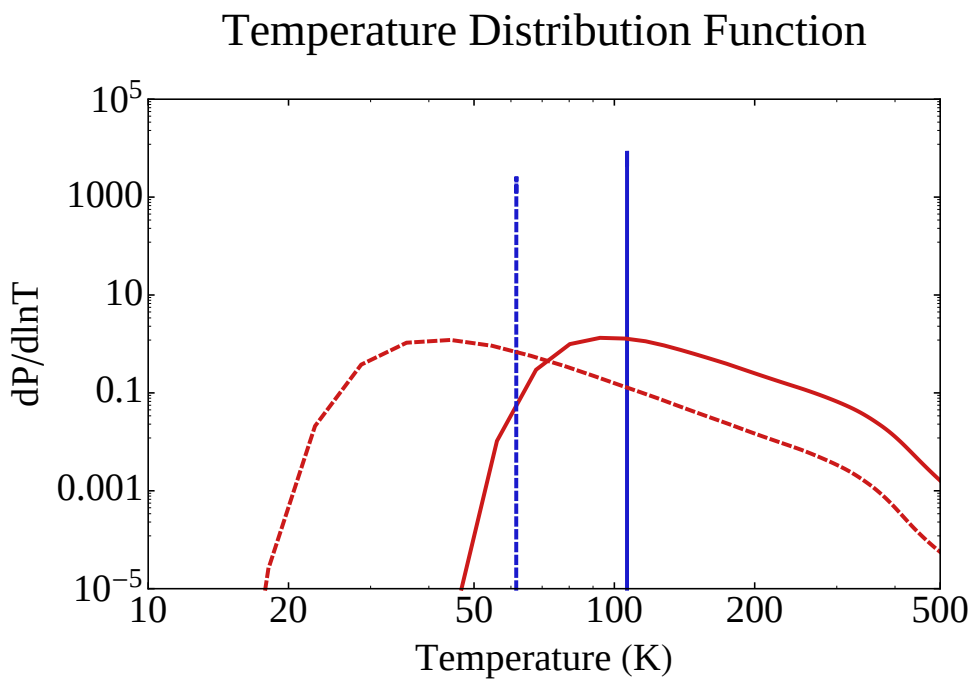

Figure 1.1: Temperature probability distribution function, dP/dT, of small (red) and large (blue) dust grains located 0.1 (solid) and 0.5 (dotted) pc from a 10^5 $L_\odot$ and 35000 K heating source.

Using the temperature PDF, the dust grain emissivity can be generalized as

$$j_\lambda = \int \mathrm{d}a \frac{\mathrm{d}n}{\mathrm{d}a} \int \mathrm{d}T \left(\frac{\mathrm{d}P}{\mathrm{d}T}\right)_a Q_{\mathrm{abs}}(\lambda)\, \pi a^2 B_\lambda(T), \tag{1.22}$$

where dn/da is the number density of dust as a function of grain size. The emission from the large and small grains described in Fig. 1.1 are plotted in Fig. 1.2. Both sets of the large and small grain SEDs in Fig. 1.2 have been normalized by the same factor such that the peak emission of the 0.1 pc distribution of dust grains is set to 1 Jy.

As expected in Fig. 1.1, the total integrated dust emission drops off by a factor of $\sim$ 25 between the dust located 0.1 and 0.5 pc away from the heating source, and the dust temperature of the large grains is consistent with what is predicted by the expression for the equilibrium temperature Eq. 1.21 where the

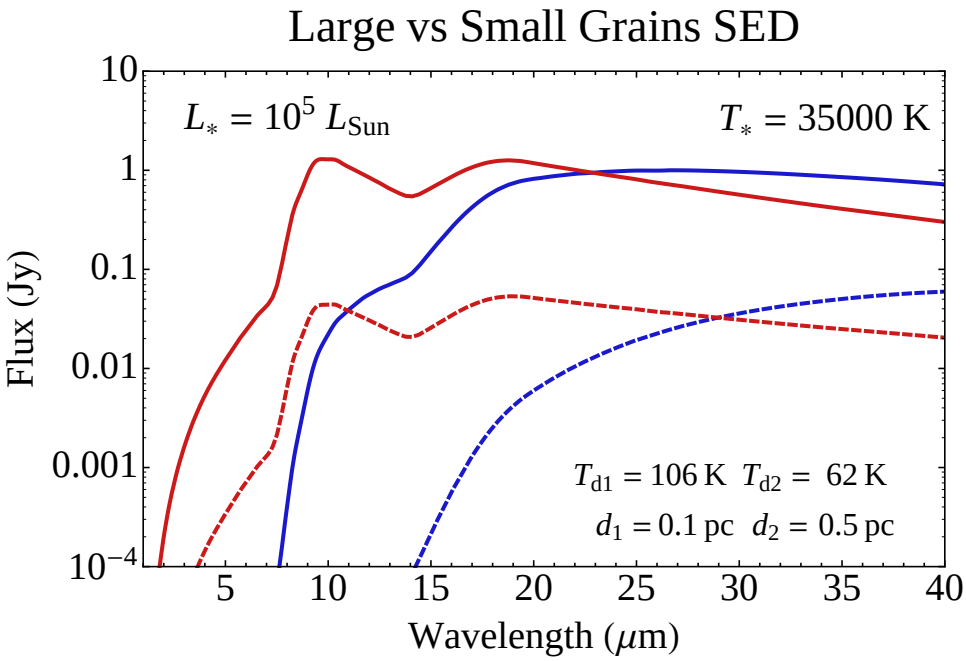

Figure 1.2: Emission from small (red) and large (blue) dust grains located 0.1 (solid) and 0.5 (dotted) pc from a $10^5\ L_\odot$ and 35000 K heating source.

0.5 pc dust will have a temperature $5^{1/3}$ (~ 1.7) times lower than the temperature of the 0.1 pc dust. The dust temperature difference between the 0.1 and 0.5 pc dust is easily noticeable by comparing the slopes of their SED; however, the shape of the small grain SEDs are very similar except for at the near-IR. The identical shapes of the 0.1 and 0.5 pc small grain SEDs are due to the width of the temperature PDF and the overlap in the higher temperatures. Although the PDF of the 0.5 pc small grains peaks at a temperature much lower than the corresponding temperature of the 0.1 pc small grain PDF peak, the emission will be dominated by the intervals when the dust is at higher temperatures. Characterizing and understanding the emission from these transiently heated small grains is therefore very important in order to properly analyze the SED from a dusty source.

CHAPTER 2

EXPLORING THE CIRCUMNUCLEAR RING AT THE GALACTIC CENTER WITH OBSERVATIONS FROM SOFIA/FORCAST

2.1 Introduction

As in many gas-rich spiral galaxies, our Galaxy has an orbiting torus of warm, dense gas circling the central, supermassive black hole: the Circumnuclear Disk (CND) (Genzel et al. 1985). Due to heavy visual extinction by interstellar dust the Galactic Center (GC) has been studied intensely at infrared and radio wavelengths. Early infrared observations taken aboard the Kuiper Airborne Observatory (KAO) revealed the presence of strong, extended IR emission from the inner few pc of the GC interpreted as a ring of hot dust (Becklin, Gatley, & Werner 1982). Radio observations revealed the compact radio source, Sgr A*, located near the center of thermal streamers of ionized gas referred to as the "minispiral", or Sgr A West, as well as emission from the non-thermal shell, Sgr A East (Balick & Brown 1974; Yusef-Zadeh & Morris 1987; Roberts & Goss 1993). Sgr A*, the dynamic center of the Galaxy ($d_{GC} \sim 8$ kpc (Reid et al. 1993)), is identified with a 4 million Solar mass (Ghez et al. 2008; Gillessen et al. 2009) supermassive black hole.

Surrounding Sgr A* and extending from 1.4 pc to beyond $\sim$ 5 pc is the clumpy torus of dense molecular gas and dust known as the Circumnuclear Disk. Atomic fine-structure line observations (63 μm [O I]) of the Sgr A West re-

Appears as Lau, Herter, Morris, Becklin, and Adams 2013, ApJ, 775, 37

gion revealed that the CND indeed circulates around Sgr A* (Genzel et al. 1984; Jackson et al. 1993). Much of the ionized gas features observed at Sgr A West are coincident with the inner edge of the CND, indicating that these features are HII regions at the inward-facing edge of the CND excited by Lyman continuum radiation from a central source; radial velocity measurements of hydrogen radio recombination lines verified that the ionized features along the Western Arc can be modeled in terms of a circular orbit around Sgr A* (Roberts & Goss 1993). Mid to far-IR observations of the warm dust emission from Sgr A West revealed dust temperatures consistent with heating from a central source (Davidson et al 1992; Telesco et al. 1996). With the Kuiper Widefield Infrared Camera (KWIC) (Stacey et al. 1993) on the KAO Latvakoski et al. (1999) captured the full ring of illuminated dust in the far-IR at the inner-edge of the CND, including the faint eastern inner-edge unobserved in the radio due to shadowing from the infalling streamers. The inconsistent appearance of the CND traced by different wavelengths arising from different physical regions has prompted us to refer to the illuminated inner edge of the CND as the "Circumnuclear Ring" (CNR). Thus, in our framework, the CNR is the ring-like structure defined by the emission from the ionized gas and hot dust at the inner edge of the CND, whereas the CND is characterized by its disk-like appearance from molecular observations.

Several different interpretations of the CNR morphology exist. Zhao et al. (2009) suggest from the radial velocity observations of the H92α recombination line that the Western Arc of the CNR as well as the Northern Arm and East-West Bar–the two streamers plunging towards Sgr A* (Lacy et al. 1980; Serabyn & Lacy 1988)–can be modeled as Keplerian orbits around Sgr A*. They find that the Western Arc exhibits a near-circular orbit, which is consistent with the morphological interpretation suggested by Latvakoski et al. (1999) from obser-

vations of hot dust emission. Latvakoski et al. (1999) treat the Northern Arm and East-West Bar as parabolic streamers with Sgr A* at the focus and having inclinations out of the plane of the CNR. Lacy et al. (1991) and Irons et al. (2012) depart from the standard circular ring interpretation of the CNR and instead present a unified model of the Northern arm and Western Arc of the CNR as a one-armed spiral density wave using velocity data from [NeII] emission.

The morphology and physical properties of the CNR (and CND) largely tie in to their interpretation as either transient or long-lived structures. Etxaluze et al. (2011) fit spectral energy distributions to their observed far-IR dust emission of the CND to determine a mass of $5 \times 10^4\,M_\odot$, which they argue is largely dominated by a distribution of cold dust ($\sim$ 20 K). The warmer dust ($\sim$ 80 K) in the CND defines the CNR; it is traced by the emission at 31 and 37 μm and implies a total mass of $\sim 1000\,M_\odot$ (Latvakoski et al. 1999). The total CNR mass is consistent between the two separate IR observations performed by Etxaluze et al. (2011) and Latvakoski et al. (1999); Etxaluze et al. (2011) determine a larger total CND gas mass because they observe at longer wavelengths and are thereby sensitive to the larger quantity of cooler dust unobserved by Latvakoski et al. (1999). Recent SOFIA work by Requena-Torres et al. (2012) study the CO rotational line transitions in the CND that imply a total CND mass of $\sim 10^4\,M_\odot$, which is comparable to that of Etxaluze et al. (2011). Observations of different molecular tracers such as HCN (Christopher et al. 2005; Montero-Castaño et al. 2009) led to a much larger estimate for the total CND mass on the order of $10^6\,M_\odot$ under the assumption that the observed clumps of molecular material in the CND are self-gravitating.

In this chapter we present 19.7, 31.5, and 37.1 μm observations tracing the

hot dust emission from the inner 6 pc of the Galactic Center taken by FORCAST aboard the Stratospheric Observatory for Infrared Astronomy (SOFIA). Our images reveal the CNR and "minispiral" at the highest spatial resolution in the mid-IR so far and allow us to study the morphology and structure of the CNR dust emission in great detail. We determine the morphological properties of the CNR and generate a dust emission ring model to compare against our observations. With our multi-wavelength coverage of the CNR we study the physical properties of the emitting dust and derive constraints to the total mass and density. At the inner edge of the CNR we resolve small ($\sim$ 0.15 pc), density-enhanced clumps that do not appear dense enough to survive the tidal shear and are therefore unlikely to be permanent features in the ring.

2.2 Observations and Data Reduction

Observations were made using FORCAST (Herter et al. 2012) on the 2.5 m telescope aboard SOFIA. FORCAST is a 256×256 pixel dual-channel, wide-field mid-infrared camera sensitive from $5 - 40$ μm with a plate scale of 0.768″ per pixel and field of view of $3.4' \times 3.2'$. The two channels consist of a short wavelength camera (SWC) operating at $5 - 25$ μm and a long wavelength camera (LWC) operating at $28 - 40$ μm. An internal dichroic beam-splitter enables simultaneous observation from both long and short wavelength cameras. A series of bandpass filters is used to image at selected wavelengths.

SOFIA/FORCAST observed the Circumnuclear Ring during Basic Science flights 63 and 64 on June 4, 2011 (altitude $\sim$ 41,000 ft.) and June 8, 2011 (altitude $\sim$ 43,000 ft.), respectively, at wavelengths of 19.7, 31.4, and 37.1 μm. The wave-

lengths 19.7 and 31.4 μm were observed simultaneously in dual channel mode, while the 37.1 μm observations were made in single channel mode. Chopping and nodding were used to remove the sky and telescope thermal backgrounds. An asymmetric chop pattern was used to place the source on the telescope axis which eliminates optical aberrations (coma) on the source. The chop throw was 7′ at a frequency of $\sim$ 4 Hz. The off-source chop fields (regions of low mid-infrared Galactic emission) were selected from KAO/KWIC images of the Galactic Center at $30-38$ μm (Latvakoski et al. 1999) and a combined Multiband Imaging Photometer for Spitzer (MIPS) 24 μm and Midcourse Space Experiment (MSX) 21 μm image of the Galactic Center that was kindly provided to us by F. Yusef-Zadeh (Yusef-Zadeh, priv. comm.). The source was dithered over the focal plane to allow removal of bad pixels and mitigate response variations. The integration time at each dither position was $\sim$ 30 sec. The quality of the images was consistent with near-diffraction-limited imaging at $19.7 - 37.1$ μm; the full width at half maximum (FWHM) of the point spread function (PSF) was 3.2″ at 19.7 μm and 4.6″ at 37.1 μm.

The acquired 30 sec integrated images were reduced and combined at each wavelength according to the pipeline steps described in Herter et al. (2013). The calibration factors that were applied to the data numbers were the average calibration factors derived from calibration observations taken over the Early SOFIA Science phase, adjusted to those of a flat spectrum (νF_ν = constant) source. The 1-σ uncertainty in calibration due to photometric error, variation in water vapor overburden, and airmass is ±7%; however, due to flat field variations ($\sim$ 15%), which we are unable to correct for, we conservatively assume a 1-σ uncertainty of ±20%.

The relatively high brightness and contrast of the CNR region on the FORCAST detectors triggered cross-talk artifacts across the images and produced some suppression of signal (i.e., a"bowl") over regions of the detector. The "bowl" is much less prominent in the images taken during flight 63 where the readout frame-rate was higher than in flight 64. We have removed much of the cross-talk artifacts using the channel subtraction algorithm, however, a residual remains along the rows that experienced the largest magnitude of the cross-talk signal. In addition to the "bowl," the images taken during flight 64 have a compact negative flux region north of the CNR due to a bright source present in the "off" position of the chop. The total absolute flux of the "bowl" and the "negative source" is $\sim$ 10% of observed flux from the CNR.

Two corrections were applied to the images to address the "negative source" and the "bowl." The images from flight 63 (where the "negative source" did not appear) were used to acquire a background flux level in the "negative source" region for flight 64. This was accomplished by subtracting the flight 64 images form the flight 63 images to characterize the flux of the "negative source" region and then remove it from the flight 64 images. By choosing regions off the source and interpolating across the source we were also able to remove the "bowl" at the penalty of removing any larger scale extended emission.

2.3 Results and Analysis

The 19.7, 31.5, and 37.1 μm images shown in Fig. 2.1 reveal the warm dust emission of the CNR) and Sgr A West in the inner 6 pc (2.6′ $\times$ 2.6′) of the Galactic Center. The coordinates of Sgr A* are $17^{h}45^{m}40^{s}.0409$, $-29°00'28.''118$ (J2000, Reid &

Brunthaler 2004), or $l = 359^\circ\,56'\,39.5''$, $b = -0^\circ\,2'\,46.3''$ in galactic coordinates. Since the spatial resolution is wavelength dependent we use Richardson-Lucy deconvolution routine to improve the spatial resolution and provide a uniform 2.5″ full-width at half maximum (FWHM) Gaussian PSF at all wavelengths. The deconvolved images have an effective resolution of 2.5″ and are shown in Fig. 2.2 along with a 19.7, 31.5, and 37.1 μm false color image in Fig. 2.3. We refer to the deconvolved images in our analyses for the rest of this chapter.

The components of the Circumnuclear Ring (CNR) and Sgr A West are clearly evident in Fig. 2.2 and 2.3. We also observe the prominent emission from the warm dust associated with the Northern Arm and East-West Bar, streamers of ionized gas falling inwards to Sgr A* (Serabyn & Lacy 1985); however, in this chapter we primarily focus on the properties of the CNR. Dust emission is observed from around the full CNR but is most prominent along the Western Arc; the flux from the eastern side of the CNR is $\sim 1/3$ of that from the Western Arc. In the cavity to the south of Sgr A* and enclosed by the southern portion of the CNR the flux drops to $\sim 10\%$ of the Western Arc flux. We observe several features around the ring extending into the southern cavity, some of which have ionized gas emission counterparts as seen in Paschen-α (Wang et al. 2010; Dong et al. 2011) and the radio continuum (Yusef-Zadeh & Morris 1987). The northern region of the CNR is much more diffuse and undefined than the southern region where the southern edge of the Western Arc defines a sharp boundary to the inner cavity. We resolve the "clumpiness" of the CNR and observe small "clumps" (FWHM $\sim 4-5''$) along the inner edge of the ring; these are discussed in greater detail in Sec. 2.4.5.

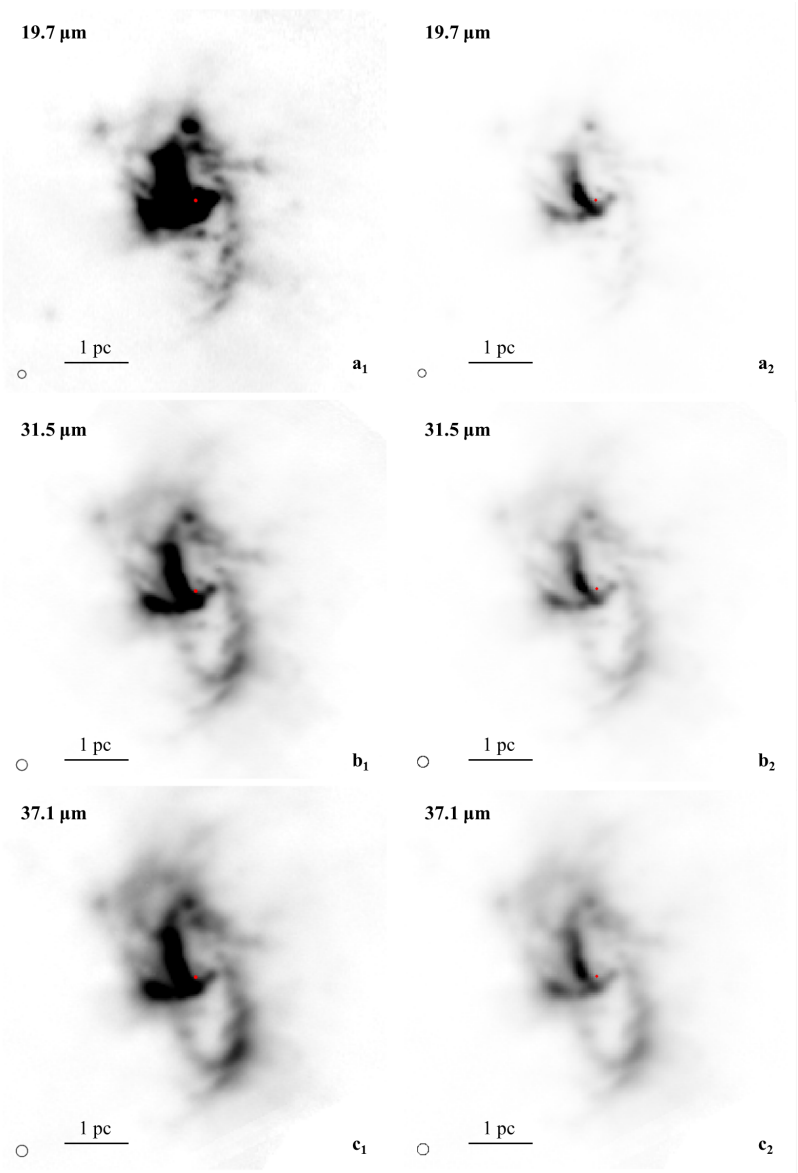

Figure 2.1: Observed 19.7 (a), 31.5 (b), and 37.1 (c) μm images of the inner 6 pc of the Galactic Center with the red dot indicating the location of Sgr A* ($17^h45^m40^s.0409$, $-29°00'28.''118$). The approximate beamsizes are shown in the lower left corner in each image. In column 1 the images are stretched linearly to show the emission from the ring. In column 2 the images are stretched linearly to show the emission from the Northern Arm and East-West Bar.

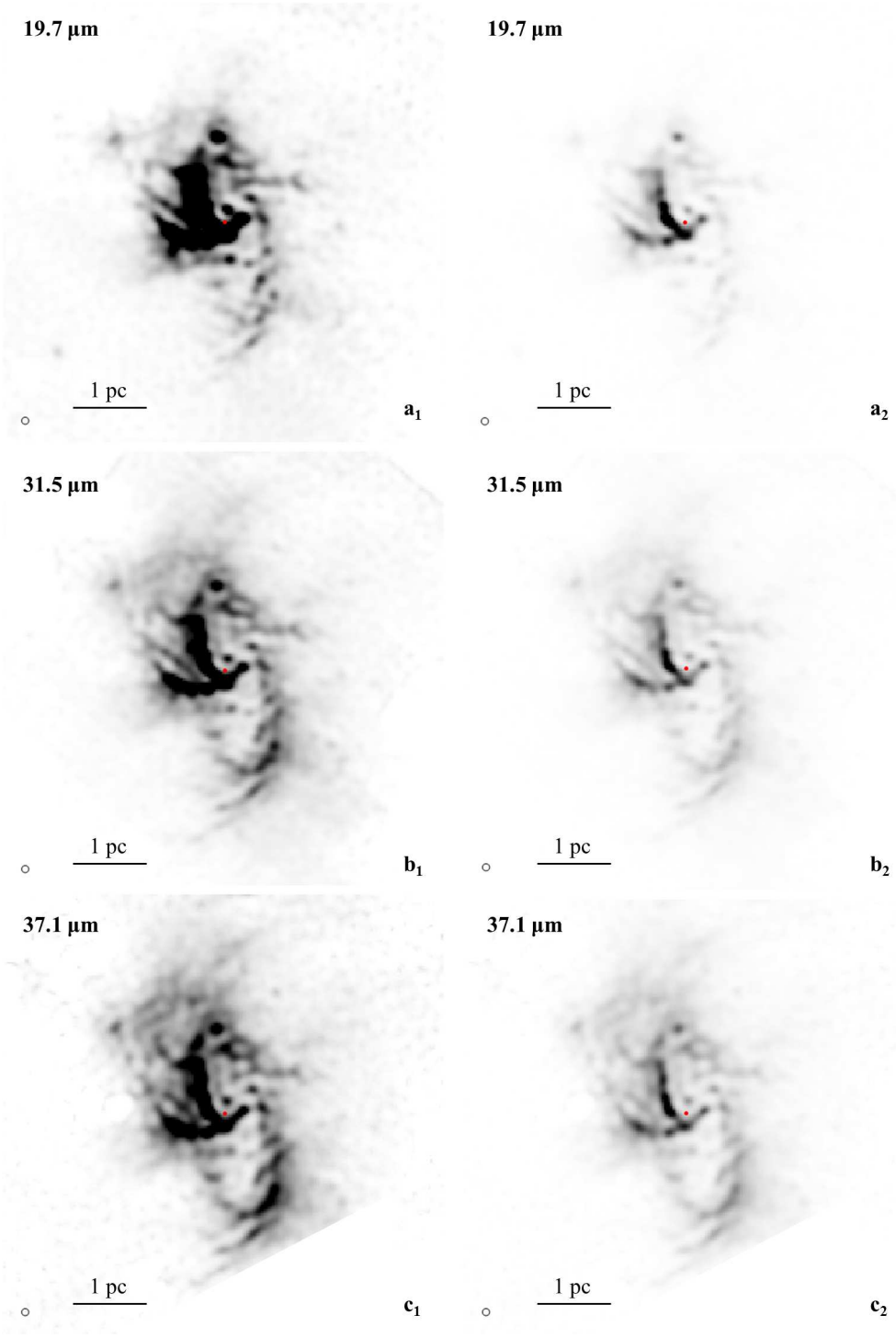

Figure 2.2: Deconvolved 19.7 (a), 31.5 (b), and 37.1 (c) μm images of the inner 6 pc of the Galactic Center to a beamsize of 2.5″ (shown in the lower left). In column 1 the images are stretched linearly to show the emission from the ring. In column 2 the images are stretched linearly to show the emission from the Northern Arm and East-West Bar.

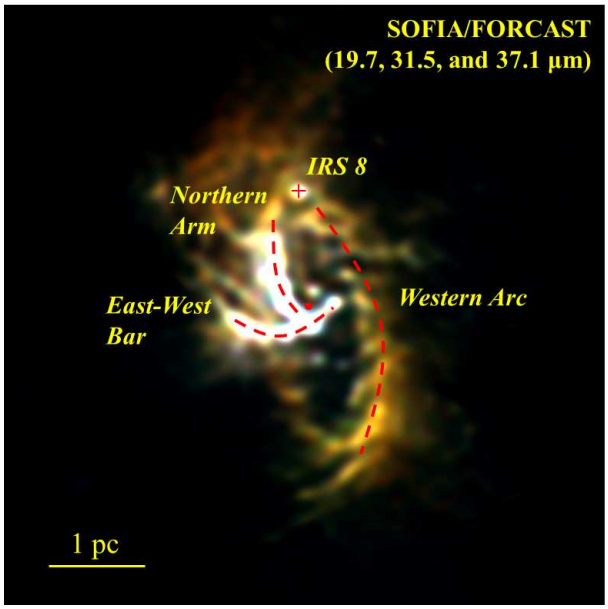

Figure 2.3: Deconvolved (2.5″ beamsize) false color image of the CNR and Sgr A West made from the three FORCAST filters: 19.7 μm - blue, 31.5 μm - green, 37.1 μm - red. The components of the CNR and Sgr A West are traced by the dotted lines. The locations of Sgr A* and IRS 8 are indicated by the dot and cross, respectively.

2.3.1 Circumnuclear Ring Morphology

The deconvolved images (Fig. 2.2) display the warm dust emission from the CNR in unprecedented detail. The schematic diagram shown in Fig. 2.4 illustrates that the CNR is observed as an ellipse due to its high inclination. Fig. 2.4 also conveys the distinct difference between the CNR and the larger, cooler distribution of gas and dust surrounding Sgr A* observed in molecular observations (Güsten et al. 1987): the CNR is the illuminated inner edge of the cool disk of gas and dust, the Circumnuclear Disk, or CND. Assuming the CNR is a circular ring centered on Sgr A* (Latvakoski et al. 1999; Zhao et al. 2009), we extract the properties of the projected CNR ellipse: the semi-minor axis is 14″ ± 2″ (0.54 pc ±0.08 pc), the semi-major axis is 36″ ± 2″ (1.4 pc ±0.08 pc), and the inclination is therefore 67° ± 5°, which is consistent with the angle derived

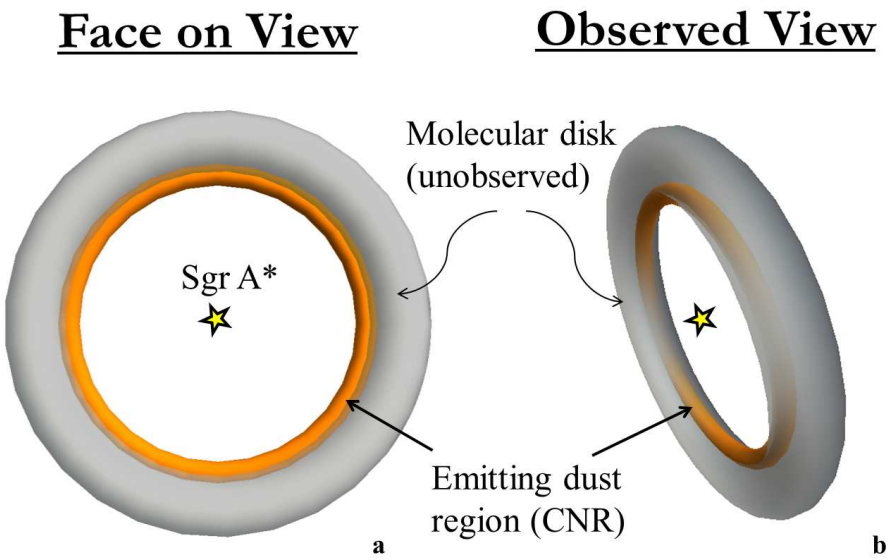

Figure 2.4: Schematic diagram of the geometry of the Circumnuclear Ring (CNR). The diagram illustrates that the CNR is the illuminated inner edge (orange) of a larger disk of cool dust and gas (grey) unobserved at our wavelengths. The face on view model (a) shows the ring-like structure of the CNR centered on Sgr A*. The observed view model (b) is the same model as (a) inclined by 67° with respect to the plane of the paper and rotated to align with the observed CNR in equatorial coordinates. The north and south regions of the CNR are brightened in (b) to reflect the effect of the inclination increasing the column density of the emitting dust along lines of sight at those regions.

by Latvakoski et al. (1999). In addition to extracting the geometric properties of the projected CNR ellipse we determine the projected width of the ring, from which we can derive its height and opening angle (Fig. 2.5). The projected width of the ring is ~ 12″ ± 1.7″ (0.45 pc) along the minor axis, which is proportional to its height, and ~ 11″ ± 1.7″ (0.4 pc) along the major axis, which is the depth of the PDR. Since the observed ring width along the major axis is the true, unprojected width of the ring we can use that and the measured minor axis ring width, assuming they are the same, to derive the opening angle and the height. We assume the geometry shown in Fig. 2.5 and determine an opening angle of ~ 12° ± 3° and a ring height of ~ 0.29 ± 0.08 pc.

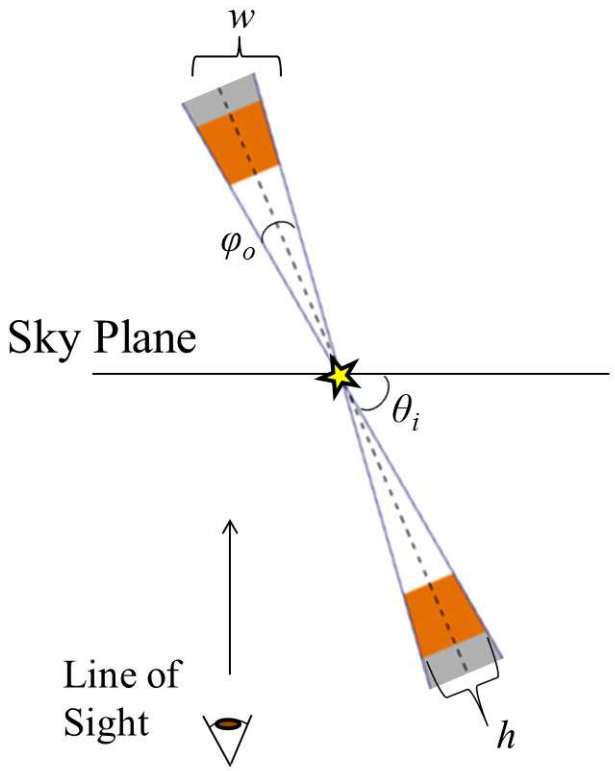

Figure 2.5: Schematic cross section through the CNR (orange) and the unobserved, cool dust and gas disk (grey). The morphological parameters shown are the observed ring width w, the opening angle ϕ_0, the inclination angle θ_i, and the ring height h.

2.3.2 CNR as a Classic HII Region

We observe a distinct shift in the location of the peak intensities amongst the 19.7, 31.5, and 37.1 μm intensity maps. The 19.7 μm intensity peak is displaced radially inward from the 31.5 and 37.1 μm intensity peaks by several arcseconds, which indicates that the heating sources of the CNR are located in its interior. An intensity line cut through the southern region of the CNR is shown in Fig. 2.6, illustrating the peak shifts. This observation strongly suggests that the CNR is identical to a classic HII region where the 19.7 μm dust emission primarily traces the ionized gas region while the 31.5 and 37.1 μm emissions extend

into the photo-dissociation region (c. f. Salgado et al. 2012). Our observations are consistent with the claim that the Western arc is the ionized inner edge of the CND excited by UV radiation from the central stellar cluster (Serabyn & Lacy 1985; Telesco et al. 1996).

In Fig. 2.7a and b we overlay CN 2 – 1 (Martín et al. 2012) and 6 cm radio continuum (Yusef-Zadeh & Morris 1987) contours on the 37.1 and 19.7 μm intensity maps, respectively. The CN contours trace the cooler material beyond the 37.1 μm emission region around most of the CNR while the radio contours are coincident counterparts to the 19.7 μm emission region. Fig. 2.7d shows the normalized intensity line cut through the southern CNR (Fig. 2.7c) across the 6 cm, 37.1 μm, and CN maps and presents the displacement of these three different emission regions, which is consistent with central heating. The region of the ionized gas emission at 6 cm lies slightly radially inward from the 37.1 μm, photo-dissociation region emission. Similarly, the 37.1 μm emission region is displaced inwards relative to the molecular emission region. The morphological arrangement of these regions strongly reinforces the picture of the CNR as a centrally heated structure.

2.3.3 Observed Dust Properties: Temperature, Optical Depth, and Luminosity

Large column densities of dust and gas lead to extreme extinction along lines of sight towards the Galactic Center ($A_V \sim 30$) (Cardelli et al 1989). The extinction towards the Galactic Center has been characterized by numerous extinction curves derived through various techniques (Cardelli et al. 1989; Rieke

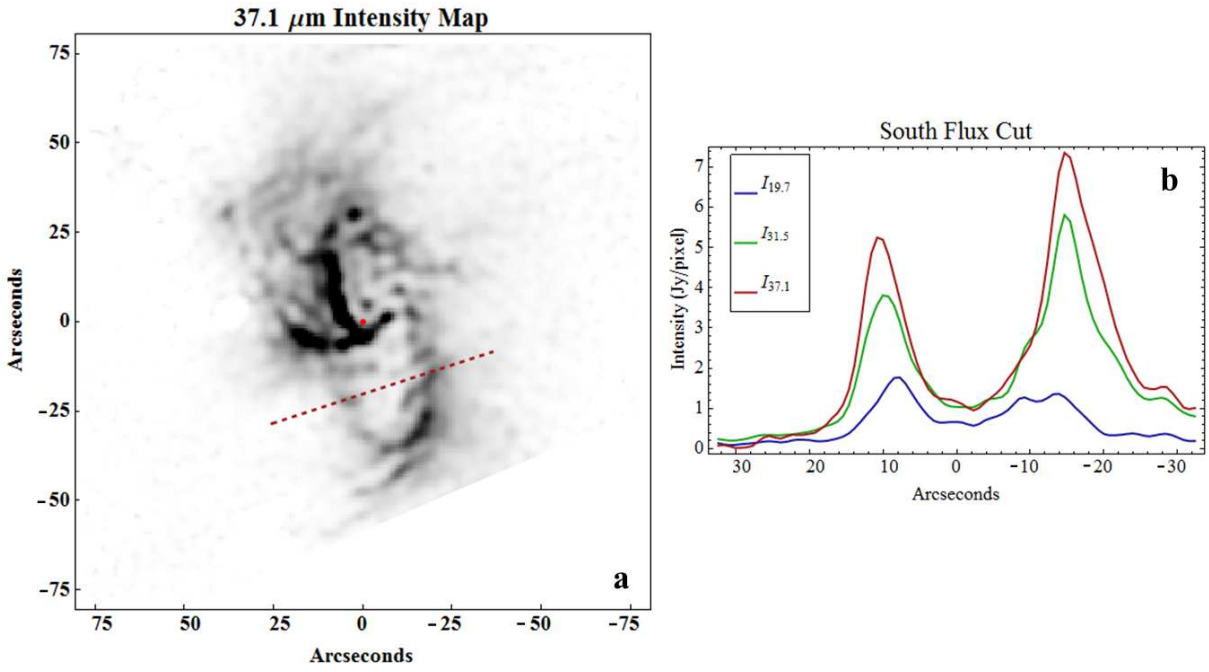

Figure 2.6: (a) Deconvolved 37.1 μm intensity map of the inner 6 pc of the GC overlaid with lines along which the intensities of the 37.1, 31.5, and 19.7 μm maps are extracted. The red dot indicates the location of Sgr A*. (b) Intensities from the 37.1, 31.5, and 19.7 μm maps along the southern line cut shown in (a) centered on (7″, -24″). The intensity plots shows noticeable shifts of the peak locations across the wavebands at the east and west regions of the CNR indicating that the observed dust in the CNR is heated centrally.

et al. 1989; Lutz et al. 1999; Fritz et al. 2011). One of the primary sources of extinction is silicate dust grains, which absorb strongly at 9.7 and 19 μm. In this chapter we adopt the curve of Fritz et al. (2011, hereafter referenced as F2011) derived from hydrogen emission lines of the minispiral from 1 - 19 μm observed by Short Wave Spectrometer (SWS) on the Infrared Space Observatory (ISO) and the Spectrograph for Integral Field Observations in the Near Infrared (SINFONI) on the Very Large Telescope (VLT). We select the F2011 extinction curve over the others because F2011 utilizes the most recent NIR (1 - 2.4 μm) observations of the Galactic Center. The F2011 curve is characterized by a -2.11 power-law slope at wavelengths shortward of 2.8 μm, absorption peaks in

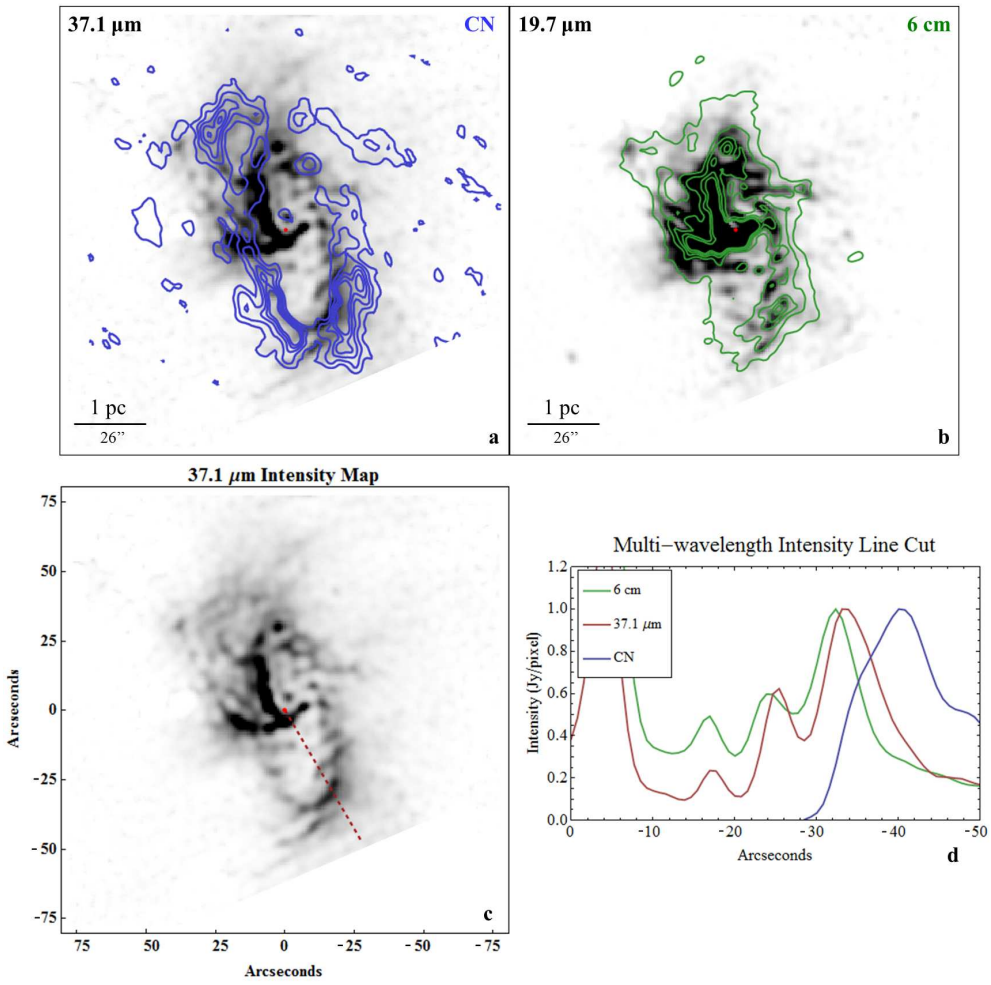

Figure 2.7: (a) Intensity map at 37.1 μm overlaid with CN 2 – 1 emission contours (Martín et al. 2012). The lowest CN contour level corresponds to 10σ with steps increasing by 15σ (σ = 2.3 Jy/Beam); the CN beam size has a FWHM of 4″ × 3″. (b) Intensity map at 19.7 μm overlaid with 6 cm radio emission contours (Yusef-Zadeh & Morris et al. 1987) with levels corresponding to 1.0, 1.7, 2.4, 3.2 and 3.9 mJy/beam; the 6 cm beam size has been convolved to the same 2.5″ FWHM Gaussian as our images. The CN emission traces the cooler material in the CNR found beyond the 37.1 μm emission region while the 6 cm emission traces the ionized gas coincident with the 19.7 μm emission. (c) 37.1 μm intensity map overlaid with a line cut intersecting the southern region of the CNR. The intensity plot in (d) shows the fluxes across the 3 wavelengths along the cut overlaid in (c) and is normalized to the peak intensity of the CNR along the cut. The outwards progression of HII region (6 cm), PDR (37.1 μm), and molecular region (CN) indicates that the CNR is being heated by a centrally located source.

the mid-IR due to composite grains (in addition to silicates and carbonaceous grains), a 9.7 μm silicate feature optical depth of $\Delta\tau_{sil} = 3.86$, and a K_S-band extinction of 2.62. Longwards of 24 μm we extrapolate from the F2011 extinction curve by adopting the Draine (2003) interstellar extinction curve defined in Fig. 10 of that paper. The extinction values at 24 microns agree between the F2011 and Draine (2003) extinction curves. From the extrapolated F2011 extinction curve, we therefore find that the ratio of the extinction at 19.7 to 31.5 μm, $e^{\tau_{19.7}}/e^{\tau_{31.5}}$, and at 19.7 to 37.1 μm, $e^{\tau_{19.7}}/e^{\tau_{37.1}}$, is 1.94 and 2.36, respectively.

After properly dereddening our images by applying the extrapolated F2011 extinction curve, we derive dust color temperature, optical depth, and total dust luminosity maps. We assume that the emission from the dust is optically thin and that the emissivity has a power-law form of ν^β and adopt an index of $\beta = 2$, which is consistent with Draine (2003). The flux from the dust at ν can be expressed as $F_\nu \propto \nu^\beta B_\nu(T_D)$, where we define T_D as the color temperature of the dust.

We use the derived color temperatures to estimate the emission optical depth, and with the power-law dust emissivity, the total dust luminosity is calculated as

$$L = 4\pi d^2 \int_{\Omega_{\rm source}} \int_0^\infty F_{\nu_{37}} \left(\frac{\nu}{\nu_{37}}\right)^\beta \frac{B_\nu(T_D)}{B_{\nu_{37}}(T_D)}\, \mathrm{d}\nu\, \mathrm{d}\Omega, \tag{2.1}$$

where $F_{\nu_{37}}$ is the observed flux at 37.1 μm, and T_D is the color temperature determined from the observed 19.7/37.1 μm emission ratio.

Color Temperature Map

The 19.7/37.1 μm color temperature map of the inner 6 pc of the Galactic Center is shown in Fig. 2.8. Given an absolute photometric error of 20% the temperatures we derive are accurate within ±8 K (ignoring uncertainties in β). The highest temperature in the field peaks at 145 K at the Northern Arm ~ 8″ to the east of Sgr A*. There is a decreasing radial temperature gradient going north along the Northern arm and going west along the East-West bar: temperatures in the Northern Arm range from 145 K to ~ 90 K where it approaches the northern edge of the CNR, and the temperatures in the East-West bar range from 140 K to ~ 90 K extending ~ 30″ to the east of Sgr A* and past the eastern edge of the CNR. The CNR exhibits a radially outwards decreasing temperature gradient except for the eastern region, where the CNR dust emission is confused with that of the East-West Bar and Northern Arm. The temperatures range from 85 K at the inner edge of the ring to ~ 65 K at the outer edge, consistent with central heating. Temperatures decrease radially due to the absorption of the dust-heating optical and UV photons. Other than the source IRS 8 (~ 30″ north of Sgr A*) we do not detect any embedded sources or large fluctuations in temperature, $\Delta T > 15$ K, along the CNR. There is therefore no evidence from our observations of star formation occurring within the CNR.

Optical Depth Map at 37.1 μm

We derive the 37.1 μm optical depth map (Fig. 2.9) from the 37.1 μm intensity map and the 19.7/37.1 color temperature map. The 37.1 μm optical depth peaks at the northern ($\tau_{37.1} \sim 0.4$) and southern ($\tau_{37.1} \sim 0.3$) edges of the CNR and decreases towards the eastern and western edges along the ring to ~ 0.05. The

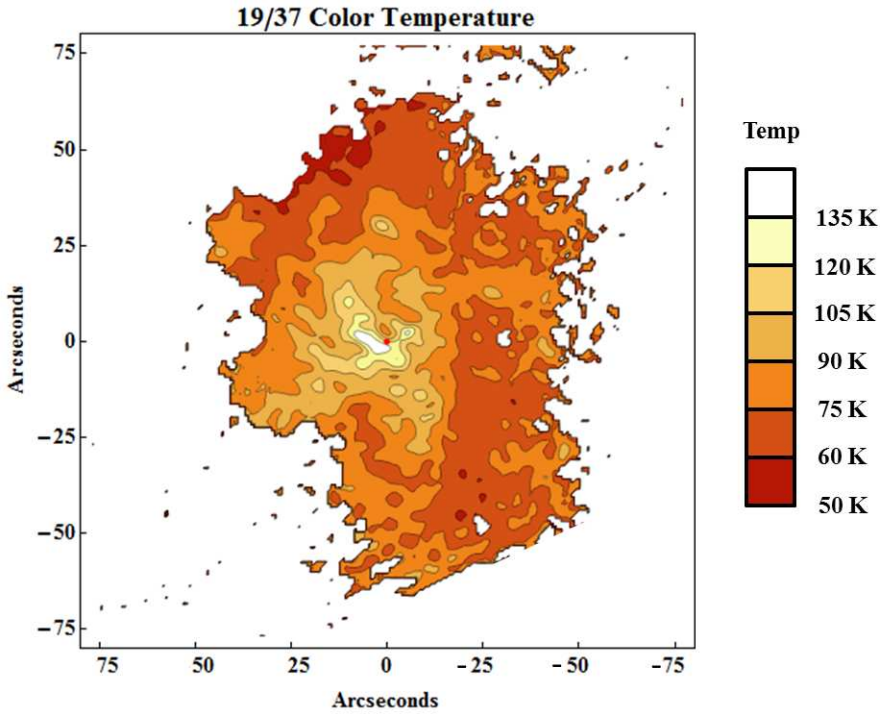

Figure 2.8: 19/37 μm color temperature contour map of the inner 6 pc of the GC, calculated for pixels with signal-to-noise greater than 2σ. The contour levels correspond to temperatures of 50, 60, 75, 90, 105, 120, 135 (white) K. The red dot indicates the location of Sgr A*. Temperatures peak at 145 K in the region near Sgr A* where the Northern Arm appears to intersect with the East-West Bar. The CNR exhibits a decreasing radial temperature gradient with temperatures ranging from 65 - 85 K. Azimuthally uniform temperatures around the CNR as well as the decreasing radial temperature gradient suggest heating of the CNR is dominated by central sources. The absence of sharp temperature fluctuations around the CNR indicates that no star formation is occurring within the ring.

increased optical depths at the north and south regions of the CNR are consistent with the enhanced column densities at those locations resulting from projection effect accompanying the high inclination of the ring, given our geometric interpretation of the ring dimensions (Fig. 2.4). Along the Northern Arm the optical depths range from 0.04 to 0.13, peaking 28″ to the northeast of Sgr A* where the Northern arm appears to intersect the northern CNR. The East-West Bar exhibits lower values of $\tau_{37.1}$, ranging from 0.03 to 0.06, and peaks at the ap-

parent intersection with the eastern CNR. Although the intensities are greatest at the Northern Arm and East-West Bar, the majority of the emitting dust in the field ($\sim$ 75%) is located in and around the CNR. We find that the 37.1 μm optical depth traces the inner edge of the molecular CN emission (Martín et al. 2012) along the Western Arc (Fig. 2.10). At the northern region of the CNR the 37.1 μm optical depth appears to closely trace the CN emission; we suggest this may be due to the shadowing caused by the Northern Arm and East-West Bar which permits CN production to occur closer to the inner edge of the CNR than in the southwest.

The total gas mass of the CNR is derived and discussed in Sec. 2.4.3.

Luminosity Map

In Fig. 2.11 we present the integrated luminosity contours derived from the 19.7/37.1 color temperature map and the 37.1 μm map. We find that the luminosity contours closely trace the 37.1 μm intensity map with the only difference being that the Northern Arm and East-West Bar appear much more prominent in the luminosity map relative to the CNR since the temperatures are much greater along those features. The luminosities of the Northern Arm and East-West Bar are $\sim 1.7 \times 10^6\,L_\odot$ and $\sim 1.8 \times 10^6\,L_\odot$, respectively. Since the Northern Arm and East-West Bar may be shadowing the eastern CNR (Latvakoski et al. 1999) we estimate the expected, total luminosity of the CNR by multiplying the Western Arc luminosity by a factor of two. We derive an expected, total CNR luminosity of $\sim 2.5 \times 10^6\,L_\odot$.

There is a "diffuse" component of the luminosity map not associated with

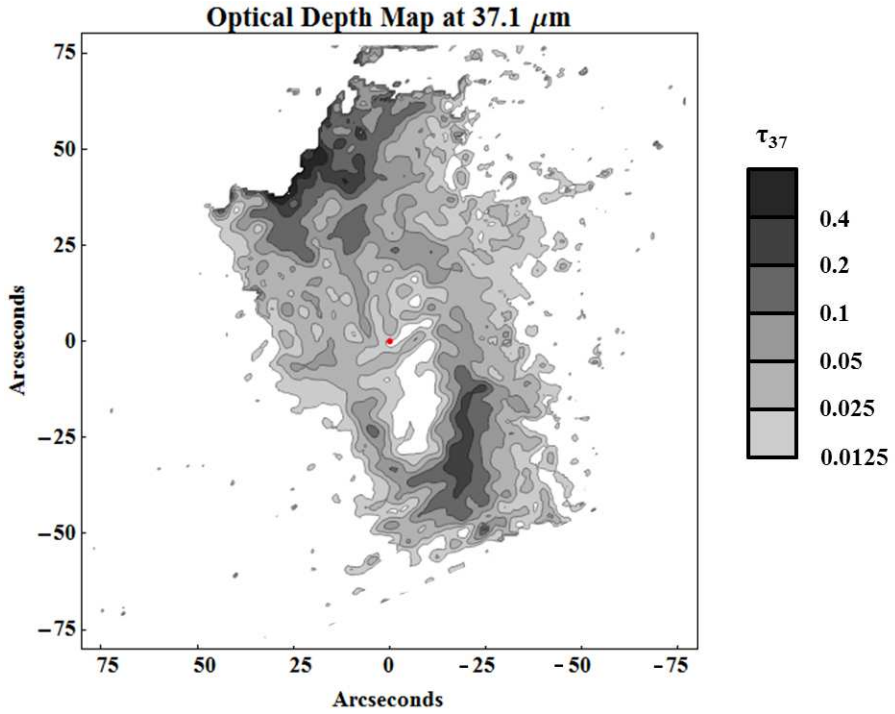

Figure 2.9: Contour plot of the optical depth at 37.1 μm of the inner 6 pc of the GC derived from the 19/37 μm color temperature map and the 37.1 μm intensity map, calculated for pixels with signal-to-noise greater than 2σ. The contour levels correspond to $\tau_{37.1}$ of 0.0125, 0.025, 0.05, 0.1, 0.2, and 0.4 (black). The red dot indicates the location of Sgr A*. Optical depths peak at 0.4 around the northern edge of the CNR. At the southern edge of the CNR the optical depths reach 0.3. The locations of the optical depth peaks are consistent with the effect of the high inclination (67 °) of the CNR increasing the column density along lines of sight at the northern and southern edges. Much of the dust in the inner 6 pc of the GC lies around the CNR and not in the Northern Arm or East-West Bar.

the CNR, Northern Arm, and East-West Bar that has a luminosity of $\sim 2.0 \times 10^6\,L_\odot$ integrated over the entire field of view. The total luminosity integrated over the inner 6 pc region is $\sim 9.7 \times 10^6\,L_\odot$. Luminosities of the various features are summarized in Table 2.1.

The stellar cluster near Sgr A* contains hot O and B stars as well as evolved Wolf-Rayet stars (Krabbe et al 1995). The combined luminosity of the central cluster is estimated by Krabbe et al. (1995) to be $\sim 2 \times 10^7\,L_\odot$. Since the outer

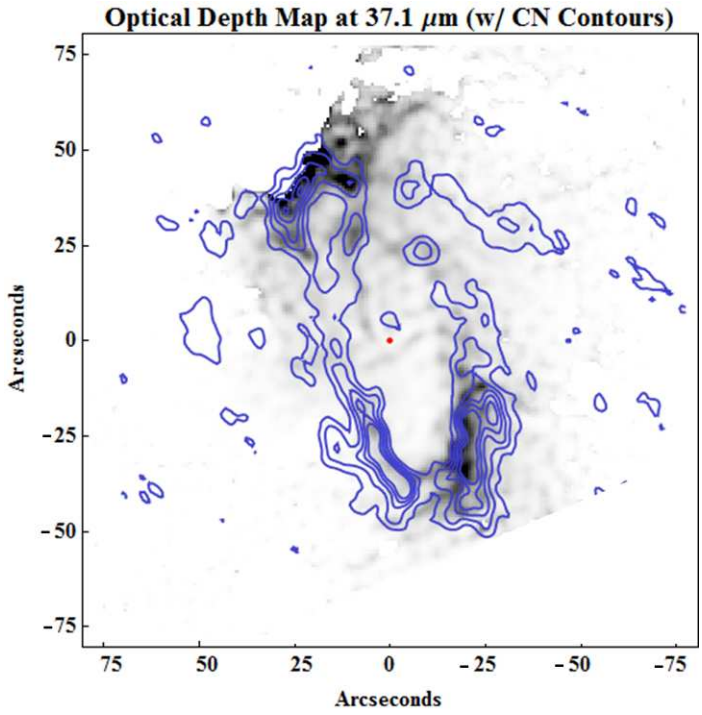

Figure 2.10: Optical depth map at 37.1 μm overlaid with CN contours (Martín et al. 2012). The contour levels are the same as in Fig. 2.7a and the optical depth map is calculated for pixels with signal-to-noise greater than 2σ. The CN contours closely trace the 37.1 μm optical depth.

Table 2.1. Sgr A West Luminosities and CNR Opening Angle

$L_{\rm bkgd}$ ($L_\odot$/pix)	$L_{\rm Tot}$	$L_{\rm Tot} - L_{\rm bkgd}$	$L_{\rm NA}$	$L_{\rm Bar}$	$L_{\rm CNR}$[a]	ϕ_0 (°)[b]
70 ± 15	9.8	7.0	1.7	1.8	2.5	14 ± 3

Note. — Units given in $10^6\ L_\odot$

[a]Expected, total CNR luminosity derived by multiplying Western Arc luminosity by a factor of two

[b]Derived from Eq. 2.2; total measured luminosity of observed stars in central cluster is $L_{\rm Cent} \sim 2 \times 10^7\ L_\odot$ (Krabbe et al. 1995)

boundary of the CNR is determined by the extinction of optical and UV photons as opposed to being limited by the amount of dust present to be illuminated, we can assume that the dust in the CNR absorbs all of the optical and UV photons emitted by the central cluster over the solid angle subtended by the inner wall of the CNR (see Fig. 2.5). This allows us to perform a consistency check on the morphology derived by the observed intensity maps. The fraction of the CNR luminosity over the luminosity of the hot central cluster stars provides an estimate of the inner wall height, h, and the opening angle of the CNR, ϕ_0,

$$\frac{L_{\rm CNR}}{L_{\rm Cent}} = \frac{2\pi R h}{4\pi R^2}, \;\; \phi_0 = 2\,\mathrm{Arctan}\left(\frac{L_{\rm CNR}}{L_{\rm Cent}}\right). \tag{2.2}$$

From the luminosity fraction we derive an inner wall height of $\sim$ 0.35 pc and an opening angle of $\sim$ 14°, which are similar to the values derived from the observed width of the CNR in the intensity map.

Inversely, the total central cluster luminosity can be derived from the observed CNR dust luminosity and opening angle. Given an opening angle of 14° and a CNR luminosity of $\sim 2.5 \times 10^6\,L_\odot$ we determine the central luminosity to be approximately $1.6 \times 10^7\,L_\odot$, which is consistent with other luminosities also derived by the dust emission and geometric analysis ($2 \times 10^7\,L_\odot$ (Davidson et al. 1992); $2.3 \times 10^7\,L_\odot$ (Latvakoski et al. 1999)).

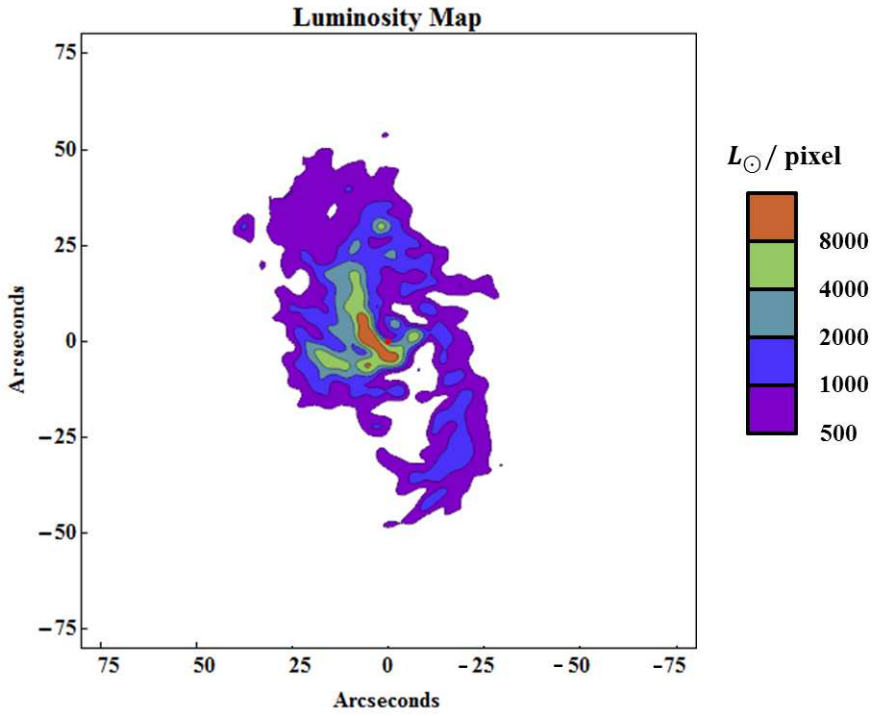

Figure 2.11: Integrated luminosity contours derived from the 19/37 μm color temperature map and the 37.1 μm intensity map, calculated for pixels with signal-to-noise greater than 2σ. The contour levels correspond to 500, 1000, 2000, 4000, 8000 $L_\odot$/pixel. The red dot indicates the location of Sgr A*. The luminosity contours closely trace the 37.1 μm intensity map. The total luminosity integrated over the inner 6 pc region is $\sim 9.7 \times 10^6$ $L_\odot$.

2.4 Discussion

2.4.1 Central Heating

In order to check the consistency of the central heating argument we calculate the theoretical equilibrium temperature of the dust in the CNR heated by the O and B stars in the central cluster. We treat the cluster as a point source at the location of Sgr A* since the size of the cluster is small compared to the radius of the CNR. The dust temperature, T_d, can then be derived from the expression shown in Eq. 2.3,

Table 2.2. DUSTY Model Parameters.

T_d (K)	$R_{\rm in}$ (pc)	$L_{\rm Source}$ ($L_\odot$)	$a_{\rm min}$ (μm)	$a_{\rm max}$ (μm)	α	m
82	1.4	2×10^7	0.1	2	-3.5	-1

Note. — T_d is the dust temperature at the inner edge, $R_{\rm in}$ is the inner radius of the CNR, $L_{\rm Source}$ is the heating source luminosity, $a_{\rm min}$ is the minimum grain size, $a_{\rm max}$ is the maximum grain size, α is the power-law index of the grain size distribution, and m is the power-law index of the radial density profile.

$$\pi a^2 Q_*(a)\, F_* = 4\pi a^2\, Q_{\rm dust}(T_d, a)\, \sigma_{\rm SB}\, {T_d}^4, \tag{2.3}$$

where $Q_{\rm dust}$ is the dust emission efficiency averaged over the Planck function of dust of size a and temperature T_d, Q_* is the dust absorption efficiency averaged over the incident radiation field, and F_* is the incident flux at the location of the dust grains. For silicate-type grains and a heating source with average temperature 35000 K (Lacy et al. 1980) we have $Q_{\rm dust}(T_d, a) = 1.3 \times 10^{-6} \left(\frac{a}{0.1\,\mu{\rm m}}\right) T_d^2$ and $Q_* \approx 1$ (Draine 2011). Assuming a distance of 1.4 pc, a total source luminosity of $\sim 2 \times 10^7$ $L_\odot$ (Krabbe et al. 1995), and a uniform size distribution of silicate-type dust grains with a standard interstellar medium grain size of ~ 0.2 μm we derive a theoretical equilibrium temperature of 90 K which is consistent with the color temperatures we observe at the inner edge of the CNR ($\sim$ 85 K).

Using the DUSTY radiative transfer code (Ivezic & Elitzur 1997) to perform an additional check on the temperature calculation, we are able to find consistent grain size parameters, that give the observed color temperatures at the inner radius of the CNR. The DUSTY model parameters are summarized in Table 2.2.

We consider the possibility of shock-driven heating by the high-velocity winds from the central cluster. The total estimated power contributed by the kinetic energy of the winds with a velocity of 700 km/s and a mass-loss rate of $10^{-2}\ M_{\odot}$/yr (Geballe et al. 1984) is $4 \times 10^5\ L_{\odot}$, which is $\sim 2\%$ of the stellar luminosity from the central cluster. We therefore conclude that the heating due to shocks is not significant compared to the radiative heating.

2.4.2 Modeling the CNR Dust Emission

Defining the outer edge of the CNR

Our picture of the CNR as the illuminated inner edge of a larger, cooler distribution of gas and dust (Fig. 2.4) allows us to calculate how deeply UV and optical photons penetrate into the ring–the point where the optical depth is ~ 1. We assume the dust properties determined by the DUSTY model shown in Table 2.2 and an inner edge gas density of $n_{H_2} = 1.0 \times 10^4\,\mathrm{cm}^{-3}$ (Davidson et al. 1992; Latvakoski et al. 1999). The distance to the $\tau_V = 1$ point can be derived as:

$$\tau_V = 1 = \int_{R_{\rm in}}^{R_{\rm in}+R_{\tau_V=1}} n(r)\,\bar{\sigma}\,\mathrm{d}r, \tag{2.4}$$

where $n(r)$ is the radial density power-law with an index of -1 (Davidson et al. 1992), $\bar{\sigma}$ is the total cross section integrated over the dust size distribution, and r is the radial distance from Sgr A*. We calculate a value of $R_{\tau_V=1} = 0.46$ pc which is similar to the observed width of the CNR along the major axis (~ 0.42 pc) in the 37.1 μm intensity map. We note that changes in the radial density power-law index do not significantly alter the value of $R_{\tau_V=1}$; for an index of 1 we have

$R_{\tau_V=1}$ = 0.35 pc.

37.1 μm Intensity Model of the CNR

We generate a 37.1 μm intensity model of the CNR assuming its morphology to be that of an inclined, circular ring (see Fig. 2.5). Instead of performing the full radiative transfer computations to determine the dust emission, we adopt a radial temperature power-law index of $-2/3$ which fits the observed temperature gradient along the major axis of the CNR in the 19/37 color temperature map. We note that a centrally heated, optically thin dust distribution would exhibit a radial temperature index of $-1/3$, assuming an emissivity power-law index of -2. The input parameters for the radius, R (1.4 pc), inner edge temperature, T_d (82 K), and inclination angle, θ_i (67°), are taken from observations, and we are free to manipulate the inner edge density, n_{H_2}, and height (opening angle), h (ϕ_0), to fit the observed intensity map. The fitted model parameters are summarized in Table 2.3. Although the emitting region of the CNR is small compared to its radius, we must treat the geometry of the emitting region in careful detail since the opening angle, ϕ_0, and the illumination depth, $R_{\tau_V=1}$, will largely determine the shape of the emission peak.

The intensity model is shown in Fig. 2.12a on the same size scale as the intensity map in Fig. 2.12b and has been convolved with a 2.5″ FWHM Gaussian to simulate the beamsize of the deconvolved images. Contours of the 37.1 μm intensity map are overlaid on the model in Fig. 2.12c. Intensities in our model range from 5 Jy/pixel along the minor axis to 10 Jy/pixel along the major axis, which is consistent with the average intensities along the minor and major axes in the observed 37.1 μm intensity map. The observed intensity contours closely

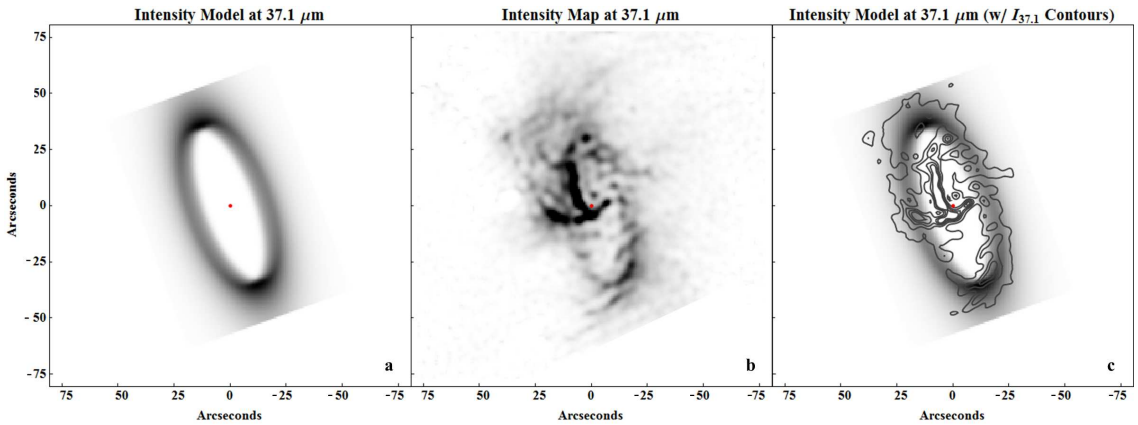

Figure 2.12: (a) 37.1 μm CNR intensity model on the same scale as the 37.1 μm intensity map shown in (b). (c) 37.1 μm intensity contours overlaid on the CNR intensity model. The intensity contours correspond to 3, 6, 9, 12, and 15 Jy/pixel. The red dot indicates the location of Sgr A*

trace the model; however, the southern emission peak in the Western Arc is shifted several arcseconds to the north-west of the corresponding model peak.

A series of intensity line cuts across the model and observed CNR is shown in Fig. 2.13. The line cuts were positioned to avoid intersecting the "clumps" at the inner edge of the CNR which is discussed in the following section. The location and amplitude of the model peaks at the Western Arc agree with the peaks from the observed intensity map. In the central (Fig. 2.13d) and southern (Fig. 2.13e) intensity line cuts even the widths of the model peaks closely agree with the observed intensity peak widths. The southern intensity line cut is the only cut that intersects with the observed eastern CNR; the emission at the eastern peak is ~ 60% of the western peak hypothetically because the Northern Arm and East-West Bar absorb some of the UV and optical photons from the central cluster (Latvakoski et al. 1999). We do not observe the eastern CNR peak in the north and central line cuts due to confusion with the emission from the Northern Arm and East-West Bar.

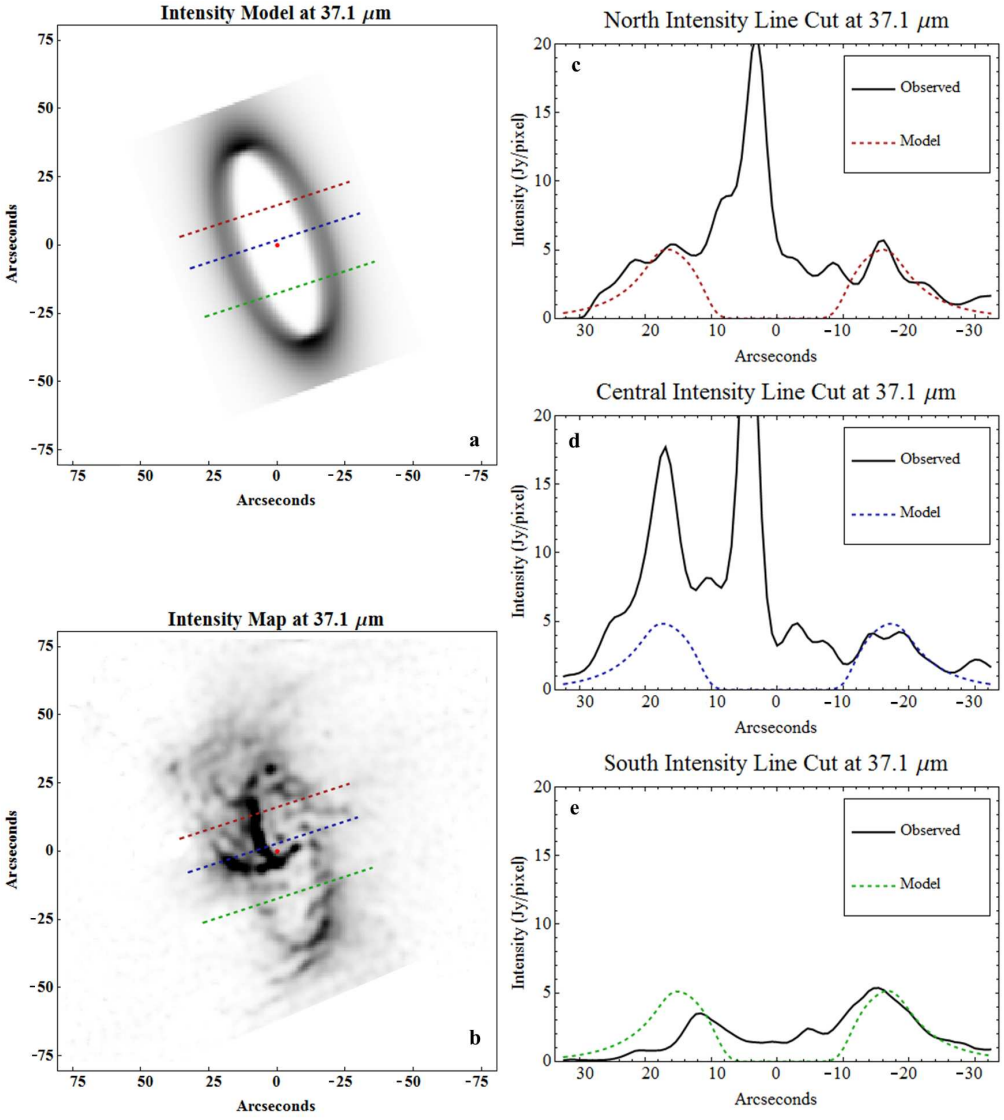

Figure 2.13: (a) 37.1 μm CNR intensity model overlaid with line cuts perpendicular to the CNR along which the intensities are extracted. (b) 37.1 μm intensity map overlaid with the same line cuts as (a). (c) Northern intensity line cut centered on the point (-6″, 19″). (d) Central intensity line cut centered on the point (-2″, 3″). (e) Southern intensity line cut centered on the point (5″, -21″). The intensity, location, and shape of the western model peaks closely follow that of the observed peaks at the Western Arc. The peak near the origin of the intensity profiles in (c) and (d) corresponds to the emission from the Northern Arm. The intensity profiles in (e) show the difference ($\sim$ 60%) in the emission from the western and eastern regions of the CNR. (Note the line cuts are intentionally placed to avoid intersecting the "clumps" at the inside edge of the CNR)

Table 2.3. Observed and Model-Derived CNR Properties.

R (pc)	h (pc)	θ_i	T_d (K)	q	n_{H_2} ($\times 10^4$ cm^{-3})	Mass from τ_{37}[a]($M_\odot$)
1.4	0.34	67°	82	-2/3	1.0	$\sim$ 610

Note. — The radius, R, temperature, T_d, radial temperature index, q, inclination angle, θ_i, and the mass are taken from observations. The CNR inner radius density, n_{H_2}, and height, h, are derived from the model.

[a]Assuming a gas to dust mass ratio of 100

2.4.3 CNR Dust Mass and Density

We derive the total dust mass of the CNR using the 37.1 μm optical depth map and the grain parameters from our 37.1 μm intensity model (Table 2.2) and assuming a gas-to-dust mass ratio of 100. Integrating over the ring in the 37.1 μm optical depth map we find a total CNR mass of $\sim$ 610 $M_\odot$, which is roughly $\sim$ 1/2 of the mass derived by Latvakoski et al. (1999) who observed the CNR at 31 and 37 μm. The discrepancy with Latvakoski et al. (1999) is due to assuming different grain parameters. Our derived mass is two orders of magnitude less than the mass derived by Etxaluze et al. (2011) and Requena-Torres et al. (2012), and roughly four orders of magnitude less than the mass derived by Christopher et al. (2005). This inconsistency can be attributed to difference in the tracers we used to study the CNR and, in the case of Christopher et al. (2005), the assumption of virialized clumps. Our observed dust emission does not trace the distribution of cooler material outside the CNR (deeper into the CND).

The CNR gas density derived by our model ($n_{H_2} = 10^4$ cm^{-3}) is consistent with the density derived observationally from our 37.1 μm optical depth map. Assuming the morphological parameters of our model the apparent thickness

along the line of sight through the major axis of the CNR is ~ 1 pc with a corresponding 37.1 μm optical depth of ~ 0.3, which implies a density of ~ 1.4×10^4 cm^{-3}. The gas densities we find are similar to those of other works studying the CNR dust emission (Davidson et al. 1992; Latvakoski et al. 1999).

2.4.4 Differential Extinction Along the Western Arc

In our analysis we assumed that the total extinction towards the CNR is constant around the ring; however, there is local extinction from the molecular component of the CND which, whose effect along the line of sight varies around the ring due to its inclined geometry. Christopher et al. (2005) suggest that the dust emission from the CNR does not trace all of the dust in the region due to extinction from high-density material in the molecular region. In this section, we therefore check for significant variations in our results when addressing the local, differential extinction.

The effect of local, differential extinction can be seen by comparing the emission from the southern region of the Western Arc between the 6 cm and Paschen-α (Wang et al. 2010, Dong et al. 2011) intensity maps (Fig. 2.14a and b). The emission at the southern Western Arc drops significantly between the 6 cm and the Paschen-α maps. Using the ratio of observed Paschen-α line flux to 6 cm radio free-free emission, we derive an absolute extinction map that agrees with that of Scoville et al. (2003). We find that the absolute extinction is greater along the Western Arc than toward the inner cavity and peaks at the southern portion of the CNR. After subtracting the interstellar extinction (A_V = 30) we produce a map that represents only the local extinction (Fig. 2.14d) towards the CNR.

The local extinction along the Western Arc ranges from $A_{P\alpha} \sim 1$ to 2 after correcting for interstellar extinction; this translates into a 19.7 μm (and 37.1 μm) extinction of less than one at the regions of peak extinction. Therefore, as a first approximation, the local, differential extinction derived by the Paschen-α and 6 cm maps is not significant at our wavelengths.

As mentioned in Sec. 2.3.2, the 19.7 μm emission primarily traces the ionized gas region of the CNR, which is where the Paschen-α and radio free-free emission originate. Unlike for Paschen-α, we do not have a relation that provides us with the intrinsic 19.7 μm emission given the 6 cm emission. We therefore produce an extinction map relative to the extinction towards a fiducial region in the 19.7 μm and 6 cm maps (the red circle in Fig. 2.14c and d). We assume that the intrinsic, unextinguished emission at 19.7 μm and 6 cm are directly proportional at all locations around the ring: $I^{\rm Int}_{19\,\mu{\rm m}} \propto I^{\rm Int}_{6\,{\rm cm}}$. The relative extinction at 19.7 μm is $\tau^{\rm (x,y)}_{19\,\mu{\rm m}} - \tau^{\rm (ref)}_{19\,\mu{\rm m}}$, where $\tau^{\rm ref}_{19\,\mu{\rm m}}$ and $\tau^{\rm (x,y)}_{19\,\mu{\rm m}}$ are the extinction values towards the reference region and towards an arbitrary position on the map, respectively. Assuming the extinction at 6 cm is negligible, the relative extinction can be derived from the relation shown in Eq. 2.5 provides the relative extinction, where we have taken the extinction at 6 cm to be negligible.

$$\left(\frac{I^{\rm Obs}_{19\,\mu{\rm m}}}{I^{\rm Obs}_{6\,{\rm cm}}}\right)_{\rm ref} = \left(\frac{I^{\rm Int}_{19\,\mu{\rm m}}}{I^{\rm Int}_{6\,{\rm cm}}}\right)_{\rm (x,y)} e^{\tau^{\rm (x,y)}_{19\,\mu{\rm m}} - \tau^{\rm ref}_{19\,\mu{\rm m}}} \tag{2.5}$$

We produce a map of the local extinction (Fig. 2.14c) by referring to the local extinction map derived from the Paschen-α/6 cm ratio (Fig. 2.14d) to determine the value of $\tau^{\rm ref}_{19\,\mu{\rm m}}$. The local extinction derived from the 19.7 μm/ 6 cm ratio ranges from $A_{P\alpha} \sim 2.5$ to ~ 4 (or $A_{19} \sim 1$ to ~ 1.7) along the Western Arc, which is somewhat larger than obtained using Paschen-α and 6 cm maps (see below).

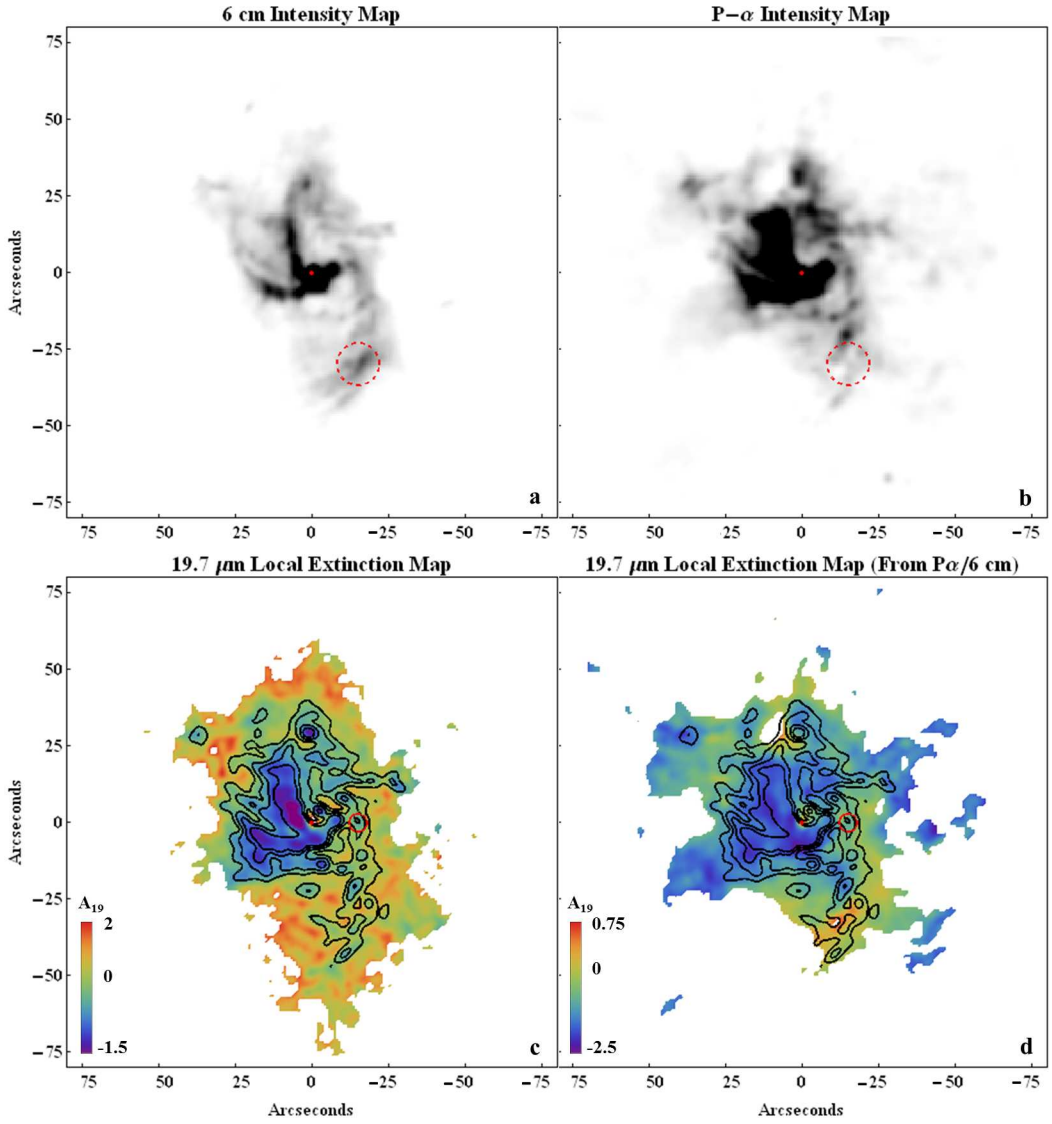

Figure 2.14: (a) 6 cm and (b) continuum-subtracted Paschen-α (1.87 μm) intensity maps convolved to a 2.5″ FWHM Gaussian PSF. The Paschen-α emission at the circled region (-15″, -30″) decreases significantly relative to the intensity from the central Western Arc and indicates the presence of local, differential extinction. (c) 19.7 μm local extinction map derived from the 19 μm and 6 cm intensity maps. (d) 19.7 μm local extinction map derived from the Paschen-α and 6 cm intensity maps. Both (c) and (d) have the 19.7 μm intensity contours overlaid, with levels corresponding to 1, 2, 4, 8, and 16 Jy/pixel. The solid red circle (-15″, 0″) shows the reference region where the relative extinction was determined. The visual magnitude assumed for the interstellar extinction is $A_V = 30$.

We apply this local extinction correction to the dereddened 19.7 and 37.1 μm images and find that the total flux along the Western Arc increases by $\sim$ 60% and $\sim$ 15%, respectively. The corrected 19.7/37.1 color temperature map does not exhibit deviations greater than $\pm$10 K ($\sim$ 15%) from the uncorrected color temperature map, which is on the order of our estimated error. Since the 37.1 μm flux and the color temperature do not change significantly we choose to ignore the effect of differential extinction and stand by our original analysis. Of course the assumptions of a constant 19.7 μm to 6 cm ratio likely introduces additional uncertainty to the intensity maps corrected this way.

As noted above, the local extinction derived from the 19.7 μm and 6 cm maps deviates from the extinction derived using the Paschen-α and 6 cm maps (Fig. 2.14d) by a factor of $\sim$ 2. This suggests that the extinguishing material in the molecular region of the CND is very porous and "clumpy" since the Paschen-α map will reveal only the emission unabsorbed by the intervening clumps, whereas the emission at 19.7 μm can penetrate through these same clumps and appear in the 19.7 μm map. The evidence of clumpiness is consistent with the analysis of the CND performed by Genzel et al. 1989 and Davidson et al. 1992.

2.4.5 Characterizing the CNR "Clumps"

At the inner edge of the Western Arc of the CNR (Fig 2.15) we observe several small "clumps" that have a FWHM of $\sim$ 4 – 5" ($\sim$ 0.15 pc). The clumps are regions of enhanced density relative to the CNR as opposed to being temperature peaks heated by an embedded source. The clumps are displaced radially inward

from the CNR; however, radial velocity observations indicate that the clumps are indeed part of the CNR (Irons et al. 2012). We identify three clumps along the central, inner edge of other CNR labeled "A", "B", and "C" from north to south. Clump B has a strong radio counterpart (Yusef-Zadeh and Morris 1987) while clump A has a prominent molecular counterpart observed in HCN emission (Christopher et al. 2005). We derive the masses and densities of the clumps from the 37.1 μm optical depth map and assume their volume can be estimated by $\sim \frac{4}{3}\pi\,(\mathrm{FWHM}/2)^3$. The clump properties are summarized in Table 2.4. We find that the clumps exhibit densities ranging from 5 to 9 $\times$ 10^4 cm^{-3} which are consistent with the low-excitation clump densities derived by Requena-Torres et al. (2012) in their large velocity gradient analysis of CO observations at the northern and southern regions of the CND. Requena-Torres et al. (2012) derive slightly larger clump sizes ($r \sim 0.3$ pc) than we do but their estimate is not well constrained since it is partly degenerate with the kinetic temperature. Under the assumption that the clumps are virialized, Christopher et al. (2005) determine a mass and density for clump A (core V in Christopher et al. 2005) of $\sim 2400\,M_\odot$ and $n \sim 10^7$ cm^{-3} from the HCN emission. In order for the clumps to be tidally stable, they must have densities of $n_{\mathrm{H_2}} \sim 10^7$ cm^{-3} (Christopher et al. 2005). The virial density estimate would imply that the clumps are stable against tidal disruptions; however, our density estimates, as well as those of Requena-Torres et al. (2012), suggest the clump densities are a factor of $\sim 10^3$ too low to meet the stability requirement.

We perform a simple calculation to estimate the lifetime of the clumps assuming that they are not virialized, so that their lifetime is limited by the rate at which they are azimuthally sheared as the CNR undergoes differential, Keplerian rotation around Sgr A*. Given the approximate extent of the clumps in the

Table 2.4. Observed Clump Properties.

Clump	d (pc)	FWHM (pc)	T_d (K)	n_{H_2} ($\times 10^4$ cm^{-3})	Total Mass ($M_\odot$)[a]
A	1.14	0.13	90	5	~1.5
B	1.25	0.15	86	9	~2.0
C	1.13	0.13	80	5	~2.5

[a]Assuming a gas to dust mass ratio of 100

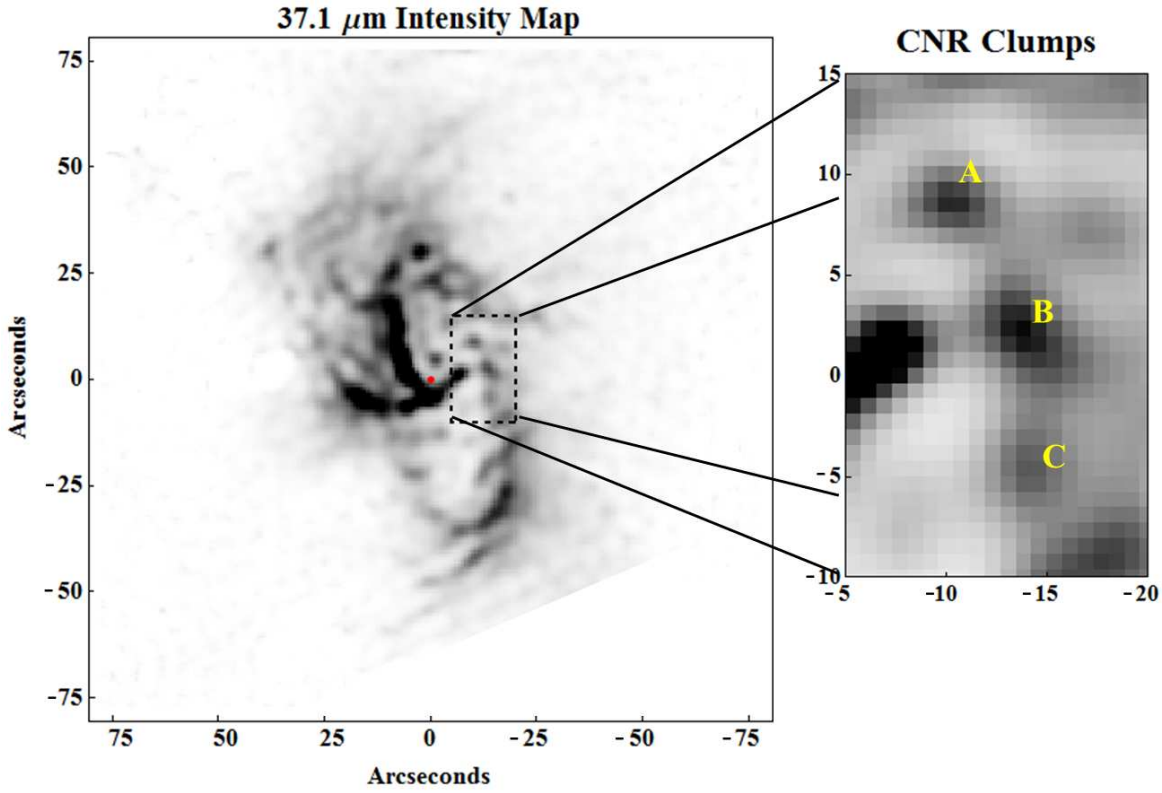

Figure 2.15: 37.1 μm intensity map of the inner 6 pc of the GC overlaid with the subregion containing three prominent clumps at the inner edge of the CNR labeled "A", "B", and "C."

radial direction from Sgr A* (~ 0.15 pc), we identify the recognizable lifetime of a clump with the time required for its opposite sides to separate azimuthally by a distance equal to the azimuthal separation of the clumps, ~ 0.3 pc. This yields a clump lifetime of ~ 40000 years, or about half of the orbital period of the CNR.

Fig. 2.16 shows the observed 37.1 μm intensity residuals after subtracting the 37.1 μm intensity model (Fig. 2.12). The clumps appear prominently at the inner edge of the Western Arc where the emission is greater than that predicted by the model, while inbetween the clumps along the ring the residuals are near zero. Interestingly, we find that the intensity model over-predicts the emission "behind" the clumps implying that they are likely shadowing the material further within the CNR. Given our derived dust grain parameters and assuming a clump density of 5×10^4 cm^{-3} we calculate that the distance to the point at which $\tau_V = 1$ within the clump is ~ 0.08 pc which is on the order of the projected clump width; therefore, the clumps may indeed be shadowing the CNR material.

While the CND is not a fully relaxed system, its relatively high degree of order and symmetry (e.g., Jackson et al. 1993) suggest that it has undergone at least a few rotations since its formation. Consequently, the very existence of such clumps is difficult to understand if they are not self-gravitating. We will turn to this key question in a subsequent paper.

2.5 Conclusions

We have presented images of the inner 6 pc of the Galaxy with a spatial resolution of 3.2 - 4.6" (2.5" deconvolved) at 19.7, 31.5. and 37.1 μm. From the images we determine the morphology and structure of the CNR to be that of an inclined (67°) 1.4 pc radius ring centered on Sgr A*. The CNR is thin relative to its radius with an inner wall height of $\sim$ 3 pc. Our morphological interpretation agrees with the previous 31 and 37 μm dust emission analysis done by Latvakoski et al. (1999). The progressively outwards physical locations of the 6 cm, 37.1 μm,

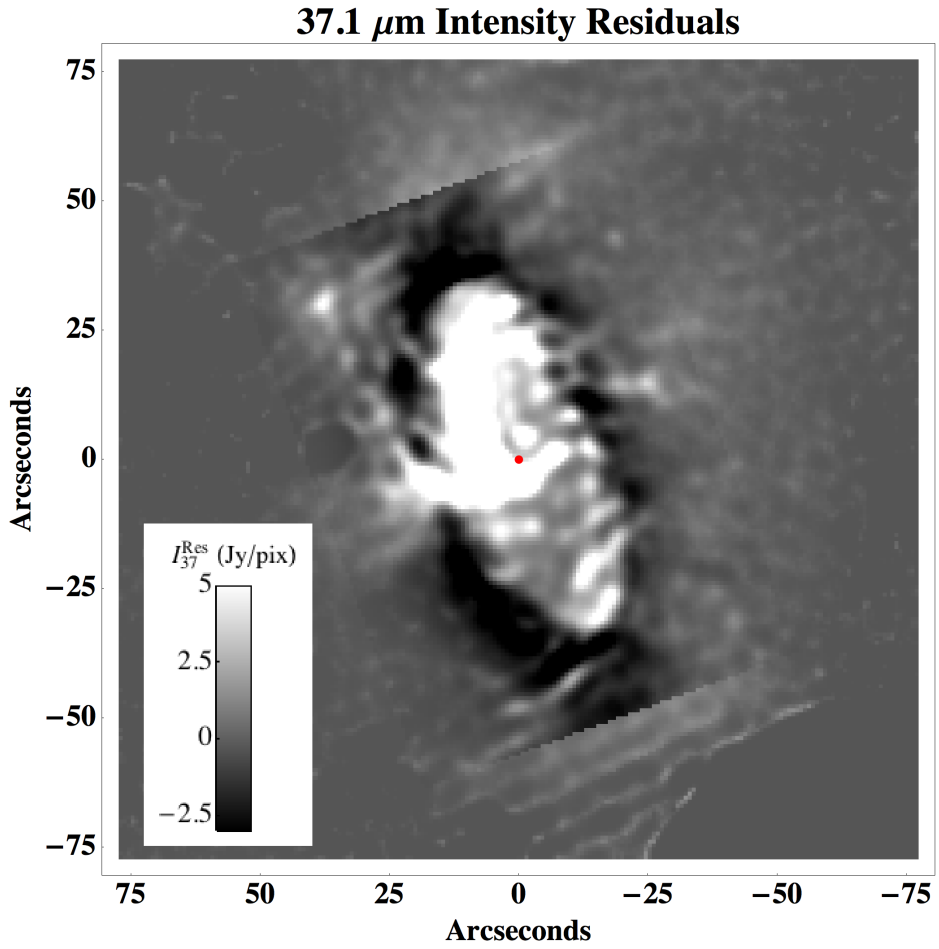

Figure 2.16: Intensity residuals from subtracting the 37.1 μm intensity model from the 37.1 μm map. Light and dark regions correspond to positive and negative intensity residuals, respectively. The intensity model is based on the Western Arc and hence oversubtracts from the shadowed eastern and northern sections of the ring. Along the inner edge of the CNR are the clumps which exhibit excess emission compared to the CNR. Behind almost every clump is a region of negative intensity indicating that the clumps shadow the CNR material behind them whereas between the clumps in the CNR the residual intensities are close to zero.

and CN emission regions show that the CNR is ionized and heated by central sources. Our temperature maps verify this picture and reveal a slightly decreasing radial temperature gradient with an inner ring temperature (85 K) consistent with theoretical calculations assuming a central point source of 2×10^7 $L_\odot$ with a temperature of 35000 K. We generate a 37.1 μm intensity model of the CNR by adopting the observed temperatures and morphological properties. We find that our intensity model agrees with the observed 37.1 μm emission from the Western Arc.

We have addressed the issue of local, differential extinction along the ring by comparing both the Paschen-α and 19.7 μm intensity maps to the 6 cm radio map, and have concluded that it did not result in a significant change to the observed intensity at our wavelengths. We however discovered an inconsistency in the magnitude of extinction between the Paschen-α and 19.7 μm-derived extinction maps: the 19.7 μm-derived extinction values were a factor $\sim$ 2 to 3 times greater than the Paschen-α derived values when converted to the extinction at identical wavelengths. We resolved this discrepancy by invoking the clumpiness of the material in the molecular region of the CND.

Our optical depth maps of the CNR reveal that the clumpiness of the ring is due to density enhancements rather than embedded sources or sites of star formation. The density of the CNR between the clumps is $\sim$ 10^4 cm^{-3}, which agrees with previous density estimates derived from the dust emission (Davidson et al. 1992; Latvakoski et al. 1999). We find that the densities and sizes of the clumps along the inner edge of the CNR ($\sim$5 to 9 $\times 10^4$ cm^{-3} and $\sim$ 0.15 pc) are consistent with the densities of low-excitation molecular clumps observed by Requena-Torres et al. (2012) at the southern and northern regions of the CNR.

Clumps of this density and size will be sheared out by the tidal forces from the supermassive black hole on timescales of half an orbital period ($\sim$ 40000 yrs) at a distance of 1.4 pc from Sgr A*. The existence of these clumps at such a close distance to Sgr A* therefore presents an interesting problem which we will further investigate.

CHAPTER 3

NATURE VERSUS NURTURE: LUMINOUS BLUE VARIABLE NEBULAE IN AND NEAR MASSIVE STELLAR CLUSTERS AT THE GALACTIC CENTER

3.1 Introduction

Stars classified as Luminous Blue Variables (LBVs) exist in a very brief ($< 10^5$ yrs) and extreme evolutionary phase nearing the end of their lifetimes. Given the brevity of their lifetimes, LBVs are extremely rare and only ~ 10 have been confirmed within the Milky Way (Clark et al. 2005). Of the known Galactic LBVs, only a few have been found to be associated with their birth-cluster (Pasquali et al. 2006). Remarkably, three LBVs are located in the vicinity of the "Quintuplet" Cluster in the Galactic Center, a site of recent massive star formation (Mauerhan et al. 2010; Figer, McLean & Morris 1999). The Quintuplet Cluster also hosts several Wolf-Rayet and dozens of O and B stars, all of which are believed to have formed coevally (Figer, McLean & Morris 1999). Since LBVs are thought to be the intermediate link between massive O stars and Wolf-Rayet stars (Langer et al. 1994), studying these three LBVs in the context of the Quintuplet Cluster provides unique insight into the evolution of massive stars.

The three LBVs in the $3' \times 3'$ vicinity of the Quintuplet Cluster are qF362 (Figer, McLean & Morris 1999; Geballe et al. 2000), the Pistol Star (Figer et al.

Appears as Lau, Herter, Morris, and Adams 2014, ApJ, 785, 120

1998), and G0.120-0.048 (Mauerhan et al. 2010) (hereafter referred to as LBV3). Although these LBVs exhibit similar luminosities ($\sim 10^6\ L_\odot$) and wind velocities ($\sim$ 100 km/s) the nature of their outflows varies drastically. LBVs are typically surrounded by nebulae composed of material from their outflows (Nota et al. 1995); however, qF362 exhibits no observable nebular emission from gas or dust whereas the Pistol Star and LBV3 have surrounding shells of gas and dust (Yusef-Zadeh & Morris 1987; Figer et al. 1999b; Mauerhan et al. 2010). The morphology and fluxes observed from the ionized gas emission in the nebulae surrounding the Pistol Star and LBV3 are notably dissimilar: the Pistol nebula appears compressed and asymmetric about the Pistol Star and shows strong emission from ionized gas at its northern edge while the LBV3 nebula is circularly symmetric about LBV3 and appears to have a uniform emission measure (Mauerhan et al. 2010). From Paschen-α observations, Figer et al. (1999) argue that the preferential ionization of the Pistol nebula is due to the proximity of the hot O and B stars of the Quintuplet Cluster located to the north of the nebula, and that the Pistol Star itself contributes less than 8% of the total ionizing flux to the nebula. The compression of the Pistol nebula at the northern edge and the northern displacement of the Pistol Star from the center of the nebula are attributed to the interaction with the winds of the Wolf-Rayet Carbon (WC) stars in the Quintuplet Cluster. Figer et al. (1999) also confirm from radial velocity observations of the Pistol nebula that it was formed from material in the outflows from the Pistol star.

LBV3 and its nebula are located approximately $\sim 2.8'$ south-west of the Pistol Star and the Quintuplet Cluster. The LBV3 nebula was recently discovered by Mauerhan et al. (2010) from the HST/NICMOS Paschen-α survey of the Galactic Center (Dong et al. 2011; Wang et al. 2010). K-band spectroscopy of LBV3

revealed its spectral similarities to the Pistol Star and qF362 and confirmed its nature as a true LBV. The spherical symmetry and uniform ionization of the LBV3 nebula strongly suggests that it is composed of material from its outflow. Like the Pistol nebula, LBV3 does not produce enough Lyman-continuum photons to ionize the nebula and is likely externally ionized primarily by the hot stars in the Arches Cluster. Although the LBV3 and Pistol nebulae exhibit different morphologies and fluxes in Paschen-α emission their near-identical size scale (r$\sim$ 200″) and wind velocities indicate that their nebular ages are very similar ($\sim 10^4$ yrs).

The thermal infrared dust emission from the Pistol and LBV3 nebulae provide important insight into the differences and similarities between the two sources. From observations with ISOCAM-CVF Moneti et al. (1999) first characterized the thermal mid-IR emission from the dust composing the Pistol nebula. The dust in the Pistol nebula appeared much more uniformly illuminated than the ionized gas; it more closely resembles a compressed sphere than the shape of a "pistol." Spitzer/IRAC 8 μm observations of the Pistol nebula (Stolovy et al. 2006) revealed a morphology identical to that found by Moneti et al. (1999). In the case of LBV3, no detection was made of the nebular dust component with Spitzer/IRAC (and no observations were made with ISOCAM-CVF). This non-detection of the dust in the LBV3 nebula at 8 μm presents an interesting dichotomy in the dust properties of the two LBV nebulae in this region. Coupled with the absence of any form of nebular emission from qF362, the differences between the two LBV nebulae can be attributed to the impact of the influence of the hot Quintuplet Cluster stars and/or differences in the local ambient medium.

In this chapter we present 19.7, 25.2, 31.5, and 37.1 μm observations tracing the warm dust emission of the Pistol nebula and the first detection of the warm dust emission of the LBV3 nebula taken by FORCAST aboard the Stratospheric Observatory for Infrared Astronomy (SOFIA). We compare and contrast the dust properties, morphology, and energetics of the nebulae and address the cause of the apparent differences between the three LBVs in this $3' \times 3'$ region of the Galactic Center.

3.2 Observations and Data Reduction

3.2.1 FORCAST Imaging

Observations were made using FORCAST (Herter et al. 2012) on the 2.5 m telescope aboard SOFIA. FORCAST is a 256×256 pixel dual-channel, wide-field mid-infrared camera sensitive from 5 – 40 μm with a plate scale of 0.768'' per pixel and field of view of $3.4' \times 3.2'$. The two channels consist of a short wavelength camera (SWC) operating at 5 – 25 μm and a long wavelength camera (LWC) operating at $28-40$ μm. An internal dichroic beam-splitter enables simultaneous observation from both long and short wavelength cameras. A series of bandpass filters is used to image at selected wavelengths.

SOFIA/FORCAST observations of the Pistol nebula and partial observations of the LBV3 nebula were made on Basic Science Flight 64 on June 8, 2011 (altitude $\sim$ 43,000 ft.) at 19.7, 31.5, and 37.1 μm. Follow-up images of both the Pistol and LBV3 nebulae were taken on the OC1-B Flight 110 on July 1, 2013 (altitude $\sim$ 39,000 ft.) at 19.7, 25.2, 31.4, and 37.1 μm. Measurements at 19.7

and 31.4 μm, as well as 25.2 and 31.5 μm for Flight 110, were observed simultaneously in dual-channel mode, while the 37.1 μm observations were made in single-channel mode. Chopping and nodding were used to remove the sky and telescope thermal backgrounds. An asymmetric chop pattern was used to place the source on the telescope axis, which eliminates optical aberrations (coma) on the source. The chop throw was 7′ at a frequency of ~ 4 Hz. The off-source chop fields (regions of low mid-infrared Galactic emission) were selected from the Midcourse Space Experiment (MSX) 21 μm image of the Galactic Center. The source was dithered over the focal plane to allow removal of bad pixels and to mitigate response variations. The integration time at each dither position was ~ 20 sec. The quality of the images was consistent with near-diffraction-limited imaging at 19.7 – 37.1 μm; the full width at half maximum (FWHM) of the point spread function (PSF) was 3.2″ at 19.7 μm and 3.8″ at 37.1 μm.

The acquired images were reduced and combined at each wavelength according to the pipeline steps described in Herter et al. (2012). The total on-source integration time with each 19.7, 25.2, and 37.1 μm filter configuration for the Flight 110 observations of the Pistol and LBV3 nebulae was ~ 100 sec and ~ 50 sec, respectively, and ~ 200 sec and ~ 100 sec at 31.5 μm for the Pistol and LBV3 nebulae, respectively. For the Flight 64 observations, the total on-source integration time was ~ 100 sec for both nebulae. The calibration factors that were applied to the data numbers were the average calibration factors derived from calibration observations taken over the OC1-B Flight series, adjusted to those of a flat spectrum (νF_ν = constant) source. The 1-σ uncertainty in calibration due to photometric error, variation in water vapor overburden, and airmass is ±7%; however, due to flat field variations (~ 15%), which we are unable to correct for, we conservatively assume a 1-σ uncertainty of ±20%.

3.2.2 ISOCAM-CVF Flux Discontinuity

The Infrared Space Observatory Camera (ISOCAM) Circular Variable Filter (CVF) observations of the Pistol nebula cover wavelengths ranging from 8 - 17 μm. The observations from ISOCAM-CVF have a plate scale of 1.5″ and a field of view of 48″ $\times$ 48″. There is a factor of $\sim$ 2.5 discontinuity between the flux from the nebula at $\leq$ 17 μm and $\geq$ 19.7 μm as determined by ISOCAM-CVF and FORCAST, respectively. Spitzer/IRAC observations of the Pistol at 8 μm also exhibit a discrepancy in flux when compared to ISOCAM. The Spitzer/IRAC 8 μm flux of the nebula and the star are factor of $\sim$ 1.5 and $\sim$ 2 greater than the ISOCAM flux measurements, respectively; however, another star in the field, qF 76 (Figer et al. 1999b), exhibits a consistent flux between the two observations. The 2.38 - 40 μm ISOCAM Short-Wavelength Spectrometer (SWS) spectrum of the Pistol nebula is used as a reference for the expected 17/19.7 μm flux ratio. To normalize the ISOCAM and FORCAST fluxes with the ISO-SWS spectrum the ISOCAM fluxes are scaled up by a factor of 1.4.

The consistent flux from qF 76 suggests that the discrepancy is unlikely due to issues with calibration. We attribute the flux discrepancy to variability in the Pistol Star luminosity over the 9 yr time interval between the ISOCAM-CVF and Spitzer/IRAC observations. Based on the dust heating models where the Pistol Star contributes to $\sim$ 15% of the heating of the nebula (Sec. 3.3.2), decreasing its luminosity by a factor of 2 will decrease the 8 μm flux by a factor of $\sim$ 1.4. This is consistent with the observed flux discrepancy between Spitzer/IRAC and ISOCAM-CVF.

3.3 Results and Analysis

The 19.7, 25.2, 31.5, and 37.1 μm images shown in Fig 3.1 reveal the warm dust emission from the Pistol nebula (a) and the LBV3 nebula (b). The equatorial coordinates (J2000) of the Pistol star and LBV3 are (266.563502, -28.834328) and (266.523436, -28.858866), respectively (Mauerhan et al. 2010). Fig. 3.2 shows the 25.2 (blue), 31.5 (green), and 37.1 (red) μm false color image of the Quintuplet Cluster region containing the three LBVs: qF362, the Pistol Star, and LBV3. We focus our analysis on the Pistol and LBV3 nebulae since we do not detect any obvious dust emission associated with qF362. The high signal-to-noise ratio of the Pistol nebula allows us to use a Richardson-Lucy deconvolution routine to improve the spatial resolution and provide a uniform 2.5″ full-width at half maximum (FWHM) Gaussian PSF at all wavelengths. For the deconvolution we derived the PSF to be Gaussian with the FWHM of the source GCS-4. In our analyses of the Pistol nebula we refer to the deconvolved images for the remainder of this chapter. Given the lower signal-to-noise ratio of the LBV3 nebula we utilize the observed images in their native resolution in our analyses.

In this section we present and analyze our results on the morphology and physical properties of dust contained in the Pistol and LBV3 nebulae. Their morphological and physical properties are summarized in Tab. 3.1. For this chapter, we assume that the Quintuplet Cluster is located in the Galactic center region at a distance of 8000 pc (Reid 1993).

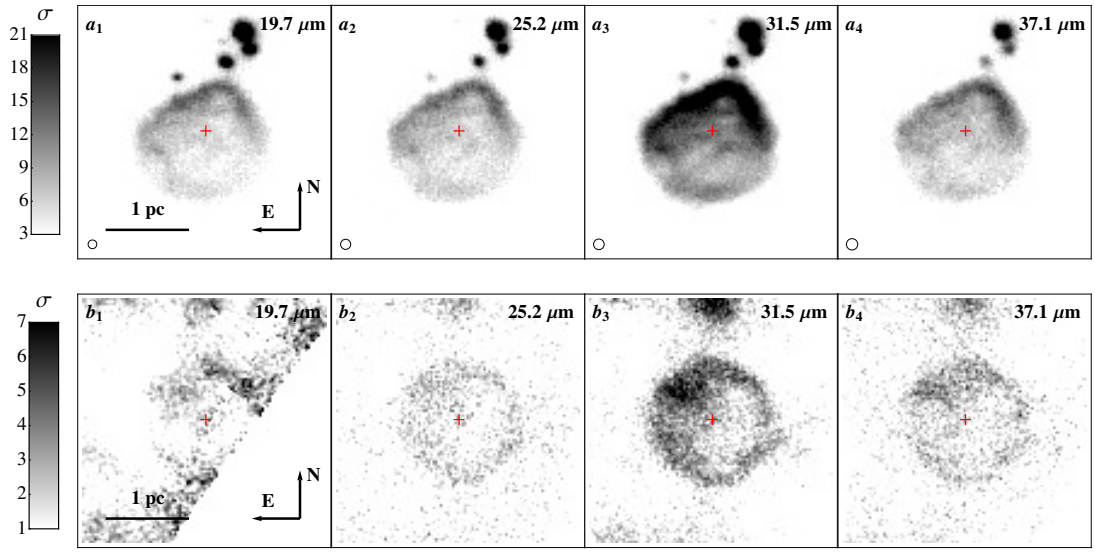

Figure 3.1: Observed 19.7, 25.2, 31.5, and 37.1 μm images of the Pistol nebula (a) and the LBV3 nebula (b) with the positions of the respective stars marked by the red cross. The emission shown is above the 3-σ flux for the Pistol nebula and above the 1-σ flux for the LBV3 nebula. 3-σ flux levels for the Pistol nebula images are 0.06, 0.09, 0.048, and 0.07 Jy/pixel at 19.7, 25.2, 31.5, and 37.1 μm, respectively; 1-σ flux levels for the LBV3 nebula images are 0.007, 0.0275, 0.0172, and 0.032 Jy/pixel at 19.7, 25.2, 31.5, and 37.1 μm, respectively. The approximate beamsizes are shown in the lower left corner in each image of (a).

3.3.1 Interstellar Extinction

Large column densities of dust and gas along lines of sight towards the Quintuplet Cluster at the Galactic Center lead to a large extinction ($A_V \sim 30$) (Cardelli et al. 1989). In this chapter we adopt the extinction curve constructed by Moneti et al. (2001, hereafter referred to as M2001) and utilize it at wavelengths longwards of 8 μm. An emissivity profile of the silicate features is used to define the M2001 curve between 8 and 24 μm. The silicate emissivity profile is a combination of the 9.7 feature derived by μ Cep observations (Roche & Aitken 1984) and the 18 μm feature derived by the late type supergiant observations (Pegourie &

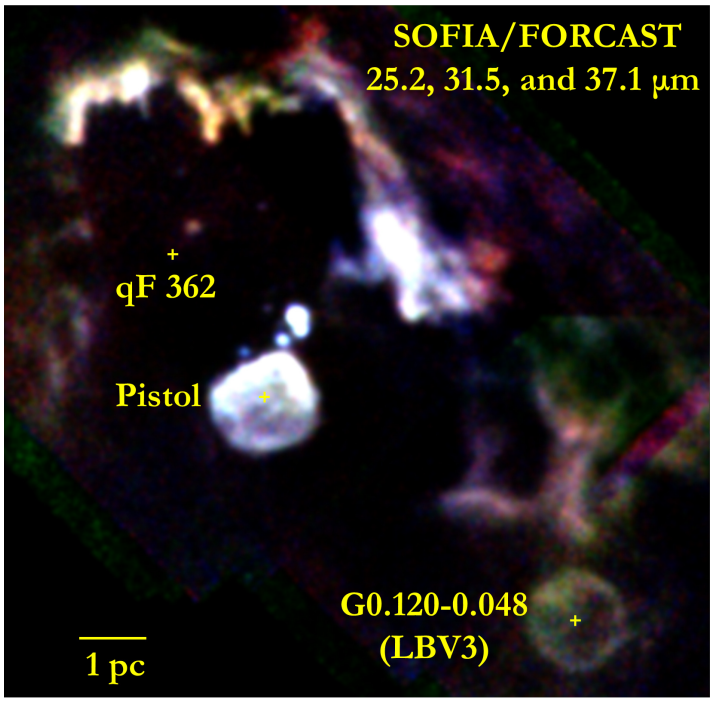

Figure 3.2: 25.2 (blue), 31.5 (green), and 37.1 (red) μm false color image of the Quintuplet Cluster containing the three luminous blue variables (LBVs) whose locations are marked by crosses.

Papoular 1985) where the peak amplitude of the 9.7 μm optical depth is 2.9 and the ratio of the 9.7 and 18 μm optical depth amplitudes is $\tau_{18}/\tau_{9.7} = 0.4$ (Simpson 1991). Longwards of 24 μm the M2001 curve follows a λ^{-2} power law (Draine & Lee 1984), which is typically assumed for Galactic Center extinction curves.

We additionally considered the Galactic Center extinction curve derived by Chiar & Tielens (2006) from the Infrared Space Observatory (ISO) Short Wavelength Spectrometer (SWS) 2.38 - 40 μm spectra of GCS 3-I, one of the five Quintuplet Proper Members. Between 8 and 24 μm in their curve, Chiar & Tielens (2006) adopt a silicate extinction profile with 9.7 and 18 μm strengths derived from fits to the spectrum of GCS 3-I assuming the underlying continuum emission can be approximated by a fourth-order polynomial. However, due to the large angular size of the ISO-SWS apertures ($14'' \times 20''$ and $14'' \times 27''$) the spec-

Table 3.1. Summary of Pistol and LBV3 Nebulae Properties

	d (pc)	$T_{\rm d}$ (K)	$L_{\rm IR}$ ($L_\odot$)	L_* ($L_\odot$)	$M_{\rm dust}$[a] ($M_\odot$)	$M_{\rm gas}$[b] ($M_\odot$)
Pistol	1.2 - 1.4	100 -180	5.2×10^5	3.3×10^6	0.03	9.3
LBV3	1.4	100	$\sim 10^5$	4×10^6	~ 0.02	6.2

[a]Determined by DustEM model fit to observed SED

[b]Derived from free-free/Paschen-α emission

trum of GCS 3-I is contaminated with the prominent IR emission from the three other adjacent Quintuplet Proper Members. In their curve the extinction falls approximately as λ^{-1} rather than the generally assumed λ^{-2} power law.

3.3.2 The Pistol Nebula

Pistol Morphology and Flux

Fig. 3.1a shows that the location of the Pistol Star, which is indicated by the red cross, is slightly displaced to the northwest of the center of the nebula. The nebula itself appears compressed along the northern and western edges and has East-West and North-South dimensions of 1.4×1.2 pc. The nearest distance in projection between the compressed northern and western edges of the nebula and the Pistol Star is $\sim$ 0.4 pc, whereas the projected distance to the eastern and southern edges is $\sim$ 0.8 pc. Dust emission from the nebula peaks along the northwest edge at all wavelengths; however, as can be seen in Fig. 3.1a, the region of peak emission migrates from the north to the west with increasing wavelength. Unlike a typical HII region (Salgado et al. 2012), we find that the

emission from the nebula appears nearly identical at each wavelength, which confirms its shell-like morphology. Normalized intensity line cuts through the nebula at each wavelength are shown in Fig. 3.3. Fig. 3.3b and c reveal the multi-wavelength similarities of the filaments and structures within the nebula. We also note that on the eastern edge of the nebula there is a faint "ridge" of enhanced emission resembling a bow shock that possibly indicates an interaction with the winds of another nearby star.

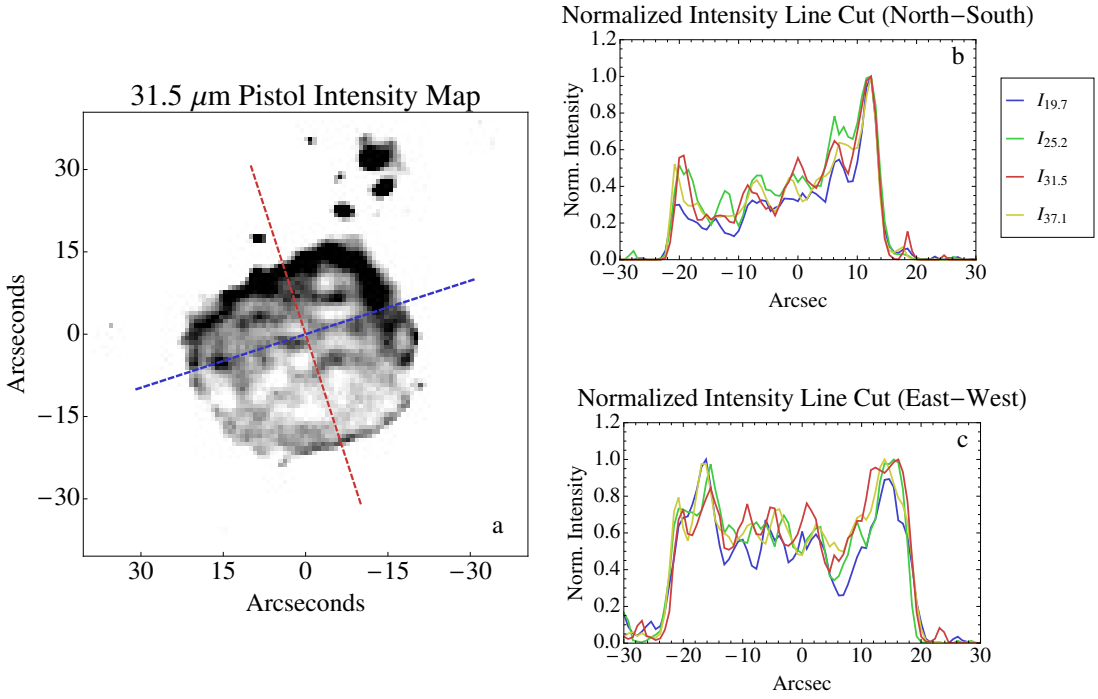

Figure 3.3: (a) 31.5 μm image of the Pistol nebula overlaid with lines centered on the Pistol Star along which intensities of the 19.7, 25.2, 31.5, and 37.1 μm maps are extracted. (b) North-South and (c) East-West intensity profiles through the nebula normalized at the peak intensity.

Paschen-α contours (Dong et al. 2011) overlaid on the 31.5 μm intensity map (Fig. 3.4a) show that the ionized gas emission from the nebula closely traces the dust along the northern and western edges. The total Paschen-α flux from the

Table 3.2. Observed Flux (Jy) from the Pistol and LBV3 nebulae

	$F_{19.7}$	$F_{25.2}$	$F_{31.5}$	$F_{37.1}$
Pistol	339	585	600	516
LBV3	40	106	158	165

Note. — Flux is given in units of Jy. 1-σ error is 20%.

nebula is $\sim 4.6 \times 10^{-10}\, ergs\, cm^{-2}\, s^{-1}$. We note that Paschen-$\alpha$ emission is more sensitive to density variations than dust emission since $I_{P\alpha} \propto n_e^2$ and $I_{Dust} \propto n_e$. As a first order correction to relate the two emission maps we "square-root" the Paschen-α intensity. Since all of the dust in the nebula is illuminated, the fact that the "square-root" Paschen-α intensity map closely traces the dust emission throughout the entire nebula suggests the nebula is fully ionized as well. The Pistol Star, which has a luminosity and effective temperature of $3.3 \times 10^6\, L_\odot$ (Mauerhan et al. 2010) and $\sim$ 12000 K (Najarro et al. 2009), is incapable of ionizing the entire nebula; therefore, we require the ionizing flux from the nearby hot, Quintuplet Cluster stars to fully ionize the nebula (Figer et al. 1999).

Observed and Predicted Pistol Dust Properties

We derive the 19.7/37.1 μm dust temperature map of the nebula (Fig. 3.4b) assuming that the emission is optically thin and can be approximated by a blackbody power-law modified by an emissivity of the form ν^β. Since the Pistol Star is oxygen-rich, the dust in the nebula is likely composed primarily of silicate-type grains; therefore, we adopt a power-law index of $\beta = 2$ which is consistent with the emissivity curve of silicates at wavelengths of $\lambda > 19\, \mu$m (Draine 2011). This

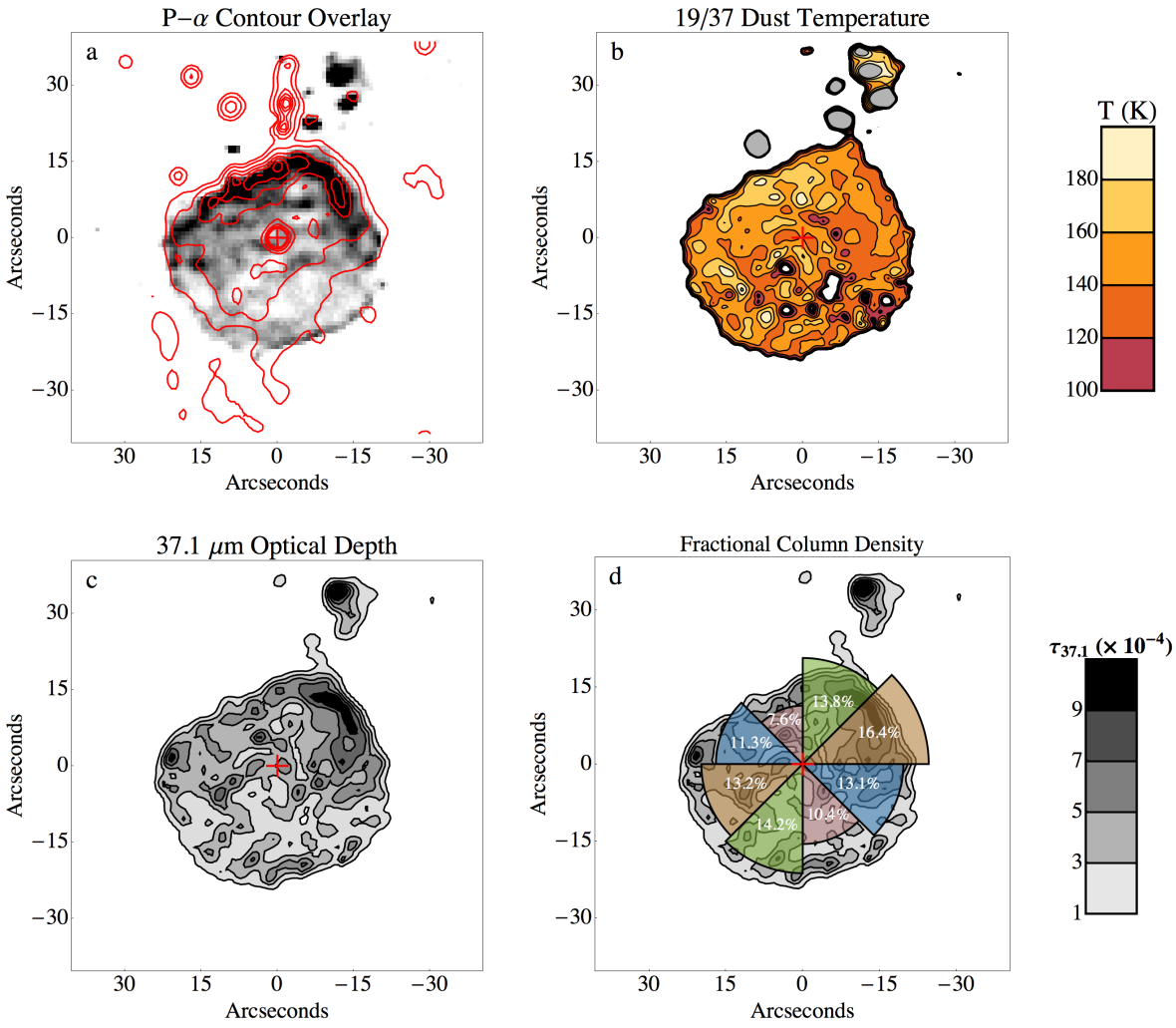

Figure 3.4: (a) 31.5 μm image of the Pistol nebula overlaid with linear Paschen-α emission contours with levels corresponding to 150, 250, 500, 750, 1000, and 1250 μJy/pixel. (b) 19/37 dust temperature map of the Pistol nebula. (c) 37.1 μm optical depth map of the Pistol nebula. (d) same as (c) with the fractional column density overlaid. The length of the wedges correspond to the fractional integrated column density within the octant.

leads to temperatures ranging from 100 - 180 K throughout the nebula, with an average of 150 ±10 K, assuming a photometric error of 20%. The temperature peaks along filaments southeast of the projected location of the Pistol star. There is also a slight temperature gradient that gradually decreases from the northeast ($T_d \sim 160K$) edge to the southwest edge ($T_d \sim 140K$).

The optical depth at 37.1 μm for optically thin emission can be expressed as

$$\tau_{37.1} = \frac{F_{37.1}}{\Omega_p \, B_\nu(T_d)}, \tag{3.1}$$

where $F_{37.1}$ is the 37.1 μm flux of the dust per pixel solid angle, Ω_p, and $B_\nu(T_d)$ is the Planck function at dust temperature, T_d. We produce a 37.1 μm optical depth map (Fig. 3.4c) using Eq. 4.1 and applying the values from the 19.7/37.1 μm temperature and the 37.1 μm intensity maps. The 37.1 μm optical depth peaks along the northwest edge of the nebula, with the largest value of $\tau_{37} \sim 10^{-3}$, and decreases to the southeast to values of $\tau_{37} \sim 3 \times 10^{-4}$. The average 37.1 μm optical depth throughout the nebula is $\sim 5 \times 10^{-4}$. We find that the compressed edges of the nebula at the north and west are consistent with the regions of increased column density, which suggests that its morphology is influenced externally by winds from the nearby carbon-dominated Wolf-Rayet (WC) stars in the Quintuplet Cluster (Figer et al. 1999) and/or density gradients in the ambient medium. This claim is reinforced by the regions of low column density at the south and east of the nebula that are on the opposite side of the projected location of the Quintuplet Cluster. Fig. 3.4d shows the fractional column density integrated over the 8 octants about the Pistol Star and overlaid on the 37.1 μm optical depth map. We observe a slight north-south asymmetry in the column density in a sense that $\sim$ 13% more dust lies in the southern four octants of the

nebula.

Under the assumption that the dust in the nebula is solely heated by the Pistol Star and is in radiative equilibrium we can estimate a theoretical dust temperature, T_d, to compare with the observed temperatures. By balancing the power input from the Pistol Star and output by the dust grains we obtain the following expression for assumed spherical grains:

$$\pi a^2 Q_*(a)\, F_* = 4\pi a^2\, Q_{\rm dust}(T_d, a)\, \sigma_{\rm SB}\, {T_d}^4, \tag{3.2}$$

where $Q_{\rm dust}$ is the dust emission efficiency averaged over the Planck function of dust grains of size a and temperature T_d, Q_* is the dust absorption efficiency averaged over the incident radiation field, and F_* is the incident flux at the location of the dust. We assume a 12000 K Kurucz model star with a log surface gravity of 4.5 and two times the solar metallicity (Kurucz 1993) as the heating source and a single-sized dust distribution of $a = 50\,$Å silicate-type grains, which will provide an upper limit on the equilibrium temperature estimate since smaller grains exhibit higher temperatures. For these heating parameters and dust properties, we have $Q_{\rm dust}(T_d, a) = 6.5 \times 10^{-8} \left(\frac{a}{50\,\text{Å}}\right) T_d^2$ and $Q_*(a) \sim 0.04 \left(\frac{a}{50\,\text{Å}}\right)$ (Draine 2011). Assuming a distance of 0.7 pc from the star to the nebula and a total source luminosity of $3 \times 10^6\,L_\odot$ (Mauerhan et al. 2010) we derive a theoretical equilibrium temperature of 88 K, which is significantly cooler than the observed 150 K. We note that since both $Q_{\rm dust}$ and Q_* are approximately proportional to the grain size, a, the derived equilibrium temperature is not sensitive the grain size. The radiation from the star itself therefore does not provide enough energy to heat the dust in the nebula to the observed temperature.

When including the radiation from the Quintuplet Cluster stars, which we approximate as a 35000 K blackbody source with a total luminosity of $2 \times 10^7\ L_\odot$ (Figer et al. 1999b) at a distance of 2.0 pc from the center of the nebula, we derive a dust equilibrium temperature of 130 K for the 50 Å-sized silicate grains. The equilibrium temperature is slightly cooler than the observed temperature derived from the 19/37 flux ratio, which may be partially due to uncertainties in the stellar models; however, we argue that the discrepancy arises due to the stochastic heating of very small grains, an effect that enhances the flux at shorter wavelengths that is not captured by the equilibrium temperature estimates. Our calculations therefore show that the observed dust temperatures are consistent with radiative heating by both the Pistol Star and Quintuplet Cluster stars, with the QC stars dominating the heating (85%).

We find that the observed emission from the nebula at $\lambda < 10\ \mu$m is a factor of ~ 5 greater than the flux predicted by a blackbody of temperature $T_{\rm dust} = 130$ K multiplied by the silicate dust emission efficiency $Q_{\rm Sil}(\lambda, a)$ (Draine & Li 2001) fit to the observed FORCAST intensities (Tab. 3.2). Again, we attribute the enhanced intensity at the shorter IR wavelengths to the transient heating of very small ($a < 100$ Å) in the nebula. Very small grains (VSGs) can reach temperatures much greater than equilibrium-heated large grains since they have small heat capacities that result in large temperature spikes after absorbing single photons. The emissivity of small grains can be characterized as

$$j_\nu = \int \mathrm{d}a \frac{\mathrm{d}n}{\mathrm{d}a} \int \mathrm{d}T \left(\frac{\mathrm{d}P}{\mathrm{d}T}\right)_a \sigma_{\rm abs}(\nu, a) B_\nu(T), \tag{3.3}$$

where n is the dust density and $\frac{\mathrm{d}P}{\mathrm{d}T}$ is a probability distribution function with $P(T)$ being the probability that a grain will have a temperature less than or equal

to T. For large grains in radiative equilibrium the probability distribution function is simply a delta function at the equilibrium temperature. The steady state probability distribution function for small grains, which is much broader than the large grain function, can be solved for analytically (Guhathakurta & Draine 1989; Draine & Li 2001).

Pistol SEDs and IR Luminosity

We utilize the DustEM (Compiègne et al. 2011) code to model the SEDs from the northern, central, southern, and full regions of the nebula. The apertures used to extract the fluxes are overlaid on the 31.5 μm image of the nebula, as in Fig. 3.5a. DustEM can model the emission from small, transiently heated grains and uses the formalism in Desert et al. (1986) to derive the temperature probability distribution function. In the models, we assume the dust is heated by both the Pistol Star and the hot stars in the Quintuplet Cluster, the latter of which also dominates the contribution of ionizing photons (Figer et al. 1999).

Since the 3-dimensional spatial distribution of the Quintuplet Cluster stars with respect to the Pistol is not known we treat the cluster's radiation field in the DustEM models in two different ways: first, as arising from a point source-like distribution having a radiation field that declines as r^{-2}, and second, as an extended distribution that produces a plane-parallel field. The distance between the Quintuplet Cluster and the Pistol Star must be greater than the projected separation ($\sim$ 1.5 pc) since the back side of the nebula, the side furthest from the observer, has been decelerated more than the front side due to interactions with the winds from the nearby WC stars (Figer et al. 1999). We therefore adopt a factor of $\sqrt{2}$ to account for the distance projection, implying a 3D separation of

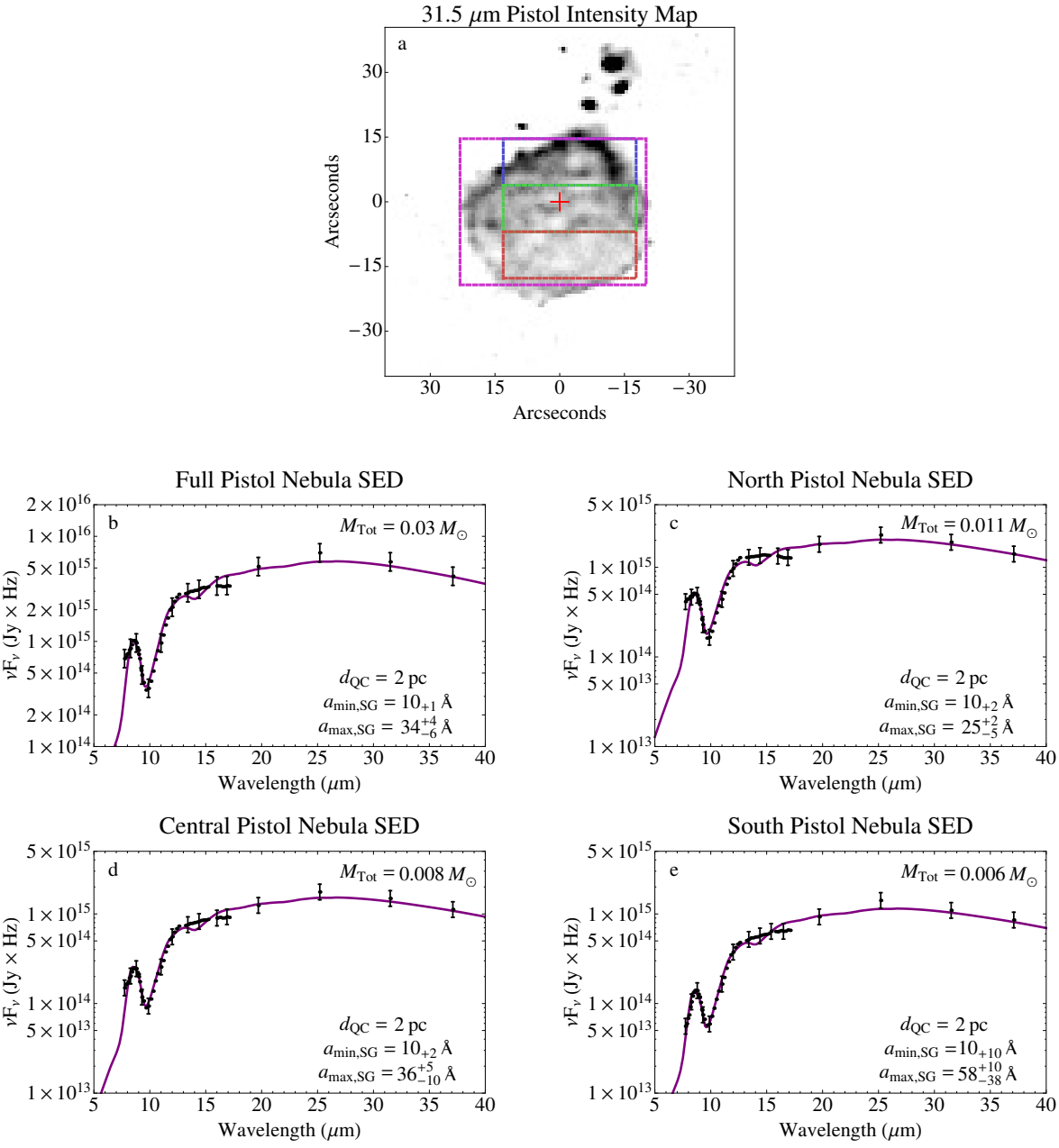

Figure 3.5: (a) 31.5 μm image of the Pistol nebula overlaid with the north, central, south, and full apertures used to extract the fluxes. (b) - (e) Plane-parallel radiation field DustEM fits to the observed ISOCAM-CVF (7 - 17 μm) and FORCAST (19.7 - 37.1 μm) fluxes in units of Jy × Hz. M_{Tot}, d_{QC}, $a_{min,SG}$, and $a_{max,SG}$ are the total dust mass, distance to Quintuplet Cluster, minimum grain size, and maximum grain size, respectively. The errors in the grain size correspond to a 3-σ deviation from the χ^2_{min}.

Table 3.3. DustEM Fitting Parameters.

	d_* (pc)	d_C (pc)	L_* ($L_\odot$)	L_C ($L_\odot$)	a_{min} (Å)	a_{max} (Å)
Pistol (PP)	0.5 - 0.7	2.0	3.3×10^6	3×10^7	10	25 - 60
Pistol (r^{-2})	0.5 - 0.7	1.8 - 2.7	3.3×10^6	3×10^7	10	26 - 40
LBV3	0.7	14	4×10^6	6×10^7	170^{+430}_{-160}	210^{+1490}_{-170}

$\sim$ 2 pc. For the plane-parallel field model we assume the entire nebula is heated by a radiation field identical to as the one expected at the center of the nebula in the r^{-2} case (d = 2.0 pc). Assuming the separation distance of 2.0 pc we find that the Pistol Star contributes an average of $\sim$ 15% to heating the dust. The best DustEM model fits to each nebular region, assuming the plane-parallel field, are shown in Fig. 3.5b - e with the minimum and maximum sizes of the small grains, $a_{min,SG}$ and $a_{max,SG}$, respectively. The r^{-2} QC field case provides nearly identical results. The fitting parameters for both models are summarized in Tab. 3.3.

We find that the nebula is composed of a distribution of VSGs with sizes ranging from 10– $\sim$ 35 Å. In addition to a gradient of decreasing flux from the north to the south of the nebula we also observe a decreasing $F_{8\mu m}/F_{25.2\mu m}$ ratio. The decreasing $F_{8\mu m}/F_{25.2\mu m}$ ratio in the plane parallel field case suggests the presence of increasingly larger grains towards the central and southern regions of the nebula. Since the total dust mass, M_{Tot}, is proportional to the dust flux we also observe a north-south gradient of decreasing mass in the plane-parallel radiation field case. A nearly identical north-south gradient is observed in the 37.1 μm optical depth map (Fig. 3.4c). We derive a total dust mass of 0.03 $M_\odot$ and an integrated IR luminosity of 5.2×10^5 $L_\odot$.

We interpret the radiation field of the Quintuplet Cluster as plane-parallel

since the Pistol Star is a member and the other cluster members are distributed within a region having an extent comparable to the distance separating them from the Pistol Star. The gradient of decreasing mass from the north to the south regions of the nebula from the models is also consistent with the observed 37.1 μm optical depth gradient. As mentioned previously, treating the Quintuplet Cluster as a point-like source with an r^{-2} field does not result in significant quantitative and qualitative differences from the plane-parallel case.

DustEM fits were attempted with the addition of an independent population of large, equilibrium-heated dust grains with a = 1000 Å. The fits indicate that in the central and southern regions of the nebula a population of large grains that comprises $\sim$ 25% of the total dust mass may be present. The peak flux contribution of the large grain population, however, is more than an order of magnitude smaller than that of the VSG population at the same wavelength. This suggests that even if large grains exist in the nebula, the total mass and IR luminosity are dominated by the VSGs.

3.3.3 The LBV3 Nebula

LBV3 Morphology and Flux

The dust emission from the LBV3 nebula shown in Fig. 3.1b appears circularly symmetric about LBV3. Although the nebula exhibits a different morphology from the compressed, asymmetric Pistol nebula they share a similar size scale: the LBV3 nebula has a diameter of $\sim$ 1.3 pc. The consistent limb-brightening at all wavelengths indicates that the nebula has a shell-like morphology. Fig. 3.6a shows the normalized and azimuthally-averaged radial intensity profiles at

25.2, 31.5, and 37.1 μm centered on LBV3. The intensity throughout the nebula is not perfectly symmetric; Fig. 3.1b shows that the intensity from the northeast quadrant is greater than the rest of the cavity by a factor of ~ 2. The enhanced emission may be due to external heating contributions from other hot stars in the region or the asymmetric ejection of material from LBV3. Due to the low signal-to-noise ratio it is difficult to accurately map out the 2-dimensional temperature structure of the nebula to resolve this issue. Given the relative isolation of LBV3, we expect that LBV3 itself is the dominant source of heating of the dust in the nebula.

Paschen-α contours (Dong et al. 2011) overlaid on the 31.5 μm intensity map (Fig. 3.6b) reveal that the emission from the ionized gas closely traces the dust around the entire nebula, including the enhanced emission from the northeast quadrant. The dust and ionized gas are therefore likely confined to the same physical region within the nebula. The total Paschen-α flux from the nebula is $\sim 2\times10^{-10}\, ergs\, cm^{-2}\, s^{-1}$, which is a factor of 2.3 less than that of the Pistol nebula.

The uniformity of the Paschen-α emission and its strong similarities to that of the dust strongly suggest that the nebula is primarily ionized by a central stellar source. Since there are currently no direct radio observations of the nebula we scale the 6 cm flux of the Pistol nebula by the ratio of the Paschen-α fluxes from the nebulae to estimate the free-free emission at 6 cm from the LBV3 nebula. Lang, Goss, & Wood (1997) find the 6 cm emission from the Pistol nebula to be 0.5 Jy, which implies from our assumptions that the 6 cm emission is 0.22 Jy for the LBV3 nebula.

The observed ratio of the Pistol nebula Paschen-α emission to that of the LBV3 nebula implies that $\sim 2\times10^{48}$ Lyman-continuum photons s^{-1} are required

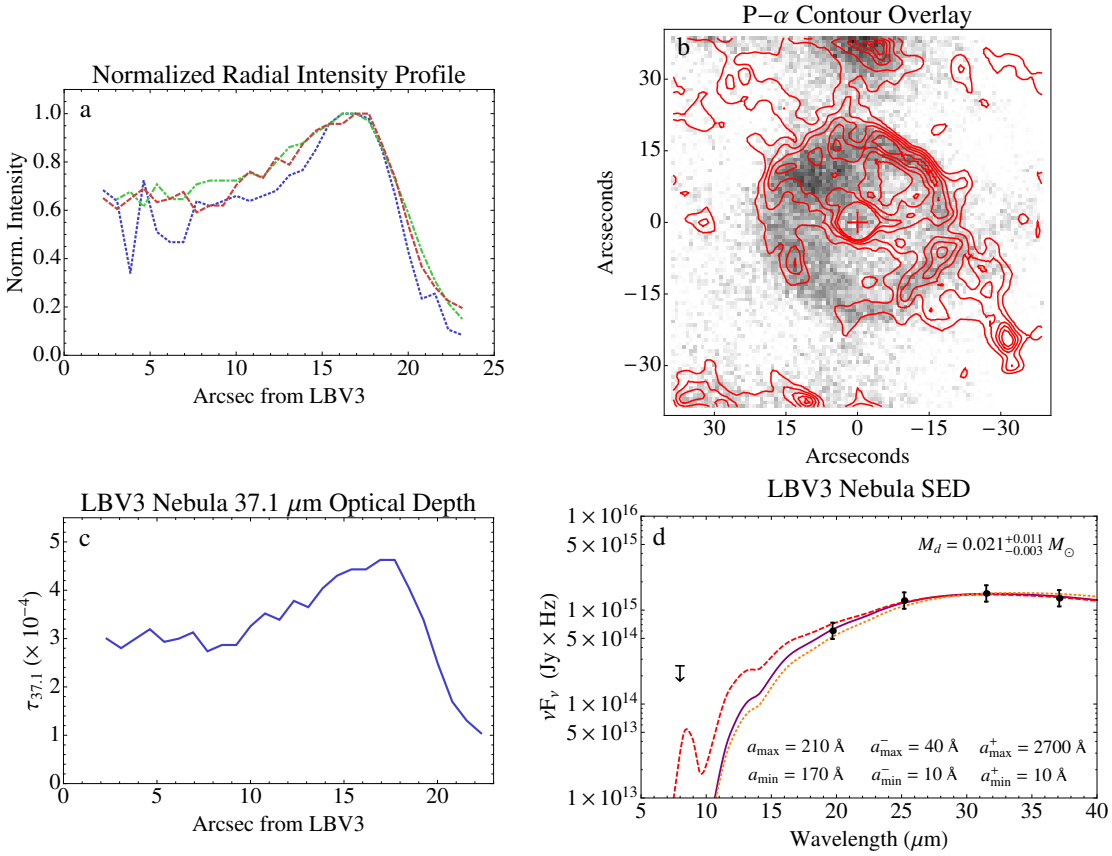

Figure 3.6: (a) Normalized radial intensity profile of the LBV3 nebula at 25.2 (blue dotted), 31.5 (green dot-dashed), and 37.1 (red dashed) μm. (b) 31.5 μm image of the LBV3 nebula overlaid with linear Paschen-α contours with levels corresponding to 150, 175, 200, 225, and 250 μJy/pixel. (c) Radial profile of the 37.1 μm optical depth of the LBV3 nebula. (d) DustEM model fits to the observed LBV3 FORCAST fluxes constraining the properties of the dust composing the LBV3 nebula.

to ionize the gas in the LBV3 nebula assuming it exhibits same electron temperature as that of the Pistol nebula, T_e = 3600 K (Lang, Goss, & Wood (1997). Adopting an electron temperature of 7000 K, a value similar to typical HII regions, only changes the Lyman-continuum flux estimate by less than 20%.

With a luminosity and effective temperature of $4 \times 10^6 L_\odot$ (Mauerhan et al. 2010) and 12000 K, respectively, LBV3 is unable to provide the ionizing flux to satisfy the observations. This suggests that the Arches Cluster, which produces

$\sim 4 \times 10^{51}$ (Figer et al. 2002) Lyman-continuum photons s^{-1} and is located ~ 10 pc away in projection from LBV3, is ionizing the nebula. Assuming the distance between LBV3 and the Arches Cluster is $\sqrt{2} \times 10$ pc we derive that the cluster contributes $\sim 2.5 \times 10^{48}$ Lyman-continuum photons s^{-1} to ionizing the nebula, which is consistent with required ionizing flux. Although the Quintuplet Cluster does not produce as many ionizing photons as the Arches it is closer in projection to the nebula and may also provide a significant fraction of the ionizing photons. Assuming a distance of $\sqrt{2} \times 7$ pc between the QC and the nebula we find that it contributes $\sim 10^{48}$ Lyman-continuum photons s^{-1}.

Observed and Predicted LBV3 Dust Properties

From the observed 19.7 and 37.1 μm fluxes of the nebula we derive a dust temperature of 105 ± 8 K assuming the silicate emissivity power law with an index of $\beta = 2$. Given a dust temperature of 105 K and the 37.1 μm intensity profile we derive the radial 37.1 μm optical depth profile shown in Fig. 3.6c. We find that τ_{37} peaks at the edges of the nebula with a value of $\sim 4.5 \times 10^{-4}$ and that it averages $\sim 3.5 \times 10^{-4}$ over the entire nebula. The optical depth profile suggests that the dust is arranged in a shell-like morphology.

We can estimate the equilibrium temperature expected for the dust in the nebula from Eq. 4.5, assuming that the heating is dominated by LBV3. For 50 Å-size silicate-type grains and a heating source with an effective temperature of 12000 K, a total luminosity of $4 \times 10^6 L_\odot$, and at a distance from the star of 0.7 pc, we derive a theoretical dust equilibrium temperature of 93 K. As with the Pistol nebula, the estimated dust equilibrium temperature may be slightly cooler than the observed temperature derived from the 19/37 flux ratio due to the presence

of very small grains.

Including the heating from the Arches Cluster, which is approximated as a 35000 K blackbody with a luminosity of 6.5 $\times$ 10^7 $L_\odot$ (Figer et al. 2002) at a presumed distance of 14 pc from the nebula, we find that the dust equilibrium temperature rises to 98 K. This dust temperature estimate is more consistent with the observed temperature than in the case with only central heating by LBV3, which suggests that, while the dust heating is dominated by LBV3 (70%), there is an additional radiative heating contribution from the Arches Cluster. This scenario is consistent with the nebula being externally ionized by the Arches Cluster since the LBV3 star has an effective temperature of 12000 K and is unable to provide enough ionizing photons.

LBV3 SED and IR Luminosity

We utilize the DustEM code to model the observed SED of the dust emission from the nebula and assume the nebula is symmetric about LBV3 and heated by both LBV3 and the Arches Cluster. LBV3 and the Arches Cluster are approximated as the same 12000 K Kurucz model star as for the Pistol model and a 6.5×10^7 $L_\odot$ blackbody source (Figer et al. 2002) with an effective temperature of 35000 K, respectively. Fig. 3.6d shows three DustEM fits to the emission from the nebula at 19.7, 25.2, 31.5, and 37.1 μm: the best fit, the 1-σ maximum grain size cutoff upper limit fit, a^+, and the 1-σ maximum grain size cutoff lower limit fit, a^-. The 1-σ upper limit of the minimum grain size cutoff is 600 Å. Also shown in 3.6d is the background continuum flux at 8 μm detected by Spitzer/IRAC. Owing to the non-detection of this background in the mid-IR, and to the "flatness" of the LBV3 SED, we are unable to tightly constrain the grain size distribution

of the nebula. The dust mass and integrated IR luminosity derived from the best-fit DustEM model are $\sim 0.021^{+0.011}_{-0.003}\ M_{\odot}$ and $8^{+1.5}_{-0.5} \times 10^4\ L_{\odot}$, respectively. The fitting parameters and results of the model are summarized in Tab. 3.3.

3.3.4 Gas to Dust Mass Ratio

We derive the total gas mass of the nebulae from the observed Paschen-α flux. For the Pistol nebula we approximate its volume as that of a spherical shell with a thickness of 0.1 pc as determined by the high-resolution Paschen-α observations by Figer et al. (1999) and an inner radius of 0.6 pc. Assuming that the entire Pistol nebula is ionized and exhibits a 6 cm flux of 0.5 Jy (Lang, Goss & Wood 1997) we determine a total gas mass of 9.3 $M_{\odot}$. Figer et al. (1999) derive a slightly greater gas mass (11 $M_{\odot}$); however, they assume a smaller volume for the nebula and that only half the nebula is ionized. From our gas mass calculation and dust model fit to the SED ($\sim 0.03\ M_{\odot}$) we derive a gas-to-dust mass ratio of 310^{+77}_{-52} for the Pistol nebula.

For the LBV3 nebula we adopt the same volume as the Pistol and estimate a total gas mass of 6.2 $M_{\odot}$. Taking the ratio of the total gas mass with the dust mass determined from DustEM model fits to the LBV3 nebula SED ($\sim 0.02\ M_{\odot}$) provides a gas-to-dust ratio of 293^{+73}_{-101}, which is similar to that of the Pistol.

These gas-to-dust mass ratio estimates of $\sim$ 300 are a factor of $\sim$ 3 times larger than that of the ISM. A majority of the LBV nebulae summarized by Nota et al. (1995) also exhibit gas-to-dust mass ratios that are factors of 3 or larger than the ISM value, which is suggestive that a larger gas-to-dust mass ratio is typical for LBV nebulae. This larger mass ratio might be expected given the

constraints on dust condensation and growth around such massive, luminous stars (Sec. 3.4.3).

3.4 Discussion

3.4.1 LBV3 Symmetric Shell Intensity Model

To understand the structure and heating of the LBV3 nebula we model the emission as originating from a spherically symmetric shell in which the dust is centrally heated by LBV3 and uniformly heated by the Arches Cluster. Input parameters are the inner shell radius, r_1, outer shell radius, r_2, the inner radius temperature, T_0, the inner shell gas density, n_0, the exponent of the power-law radial density profile, α, and the minimum and maximum grain size cutoffs. The gas-to-dust mass ratio is set to 293 and the minimum and maximum grain size cutoffs are identical to that of the southern Pistol nebula ($a_{\rm min}$ = 10 Å and $a_{\rm max}$ = 60 Å). The remaining parameters are fit with the values shown in Tab. 3.4. Fig. 3.7a and b show the 31.5 μm image of the LBV3 nebula and the intensity model convolved to the observed 31.5 μm PSF, respectively. We plot the azimuthally-averaged intensity profile of the model and the observed nebula excluding the northeast quadrant of enhanced emission in Fig. 3.7c. The slight discrepancy between the model and the observed intensities in the inner regions of the nebula (< 10″) may be attributed to confusion with the emission from the lower part of the Sickle at the northern and southeastern regions of the nebula. The best-fit model predicts a gas density of 300 cm^{-3} with a flat radial density profile between the inner and outer radii and a total dust mass of 0.02

Table 3.4. LBV3 nebula Intensity Model Parameters

r_1 (pc)	r_2 (pc)	n_0[a](cm^{-3})	$T_0(K)$	$a_{\min}$ (Å)	$a_{\max}$ (Å)	M_d $(M_\odot)$
0.66	0.78	300	95	10	60	0.02

[a]We assume a flat radial density profile

$M_\odot$, consistent with the DustEM model fits to the observed SED. We note the degeneracy between the radial density power law and inner radius parameters: a model with a steep $\alpha = 10$ radial density power-law and an inner shell radius near the center also provides an appropriate fit. Despite the degeneracy, the agreement between both $\alpha = 0$ and $\alpha = 10$ models and the observed results show that the morphology of LBV3 is that of a shell where the density rises rapidly at some radius.

3.4.2 Evidence for Complete Ionization of the Nebulae

The similar morphologies of the dust distribution, which is fully illuminated in both nebulae, and the Paschen-α emission strongly suggests that the two nebulae are completely ionized. The absence of molecular material associated with the Pistol nebula (Serabyn & Gusten 1991) also supports the claim of full ionization. From the Stromgren equation (Osterbrock & Ferland 2006), we can estimate the depth that Lyman-continuum photons from the Quintuplet Cluster stars can penetrate into the Pistol nebula, Δs, assuming the stars produce 10^{51} ionizing photons per second (Figer et al. 1999) and are located $d_N = 2.0$ pc from the Pistol.

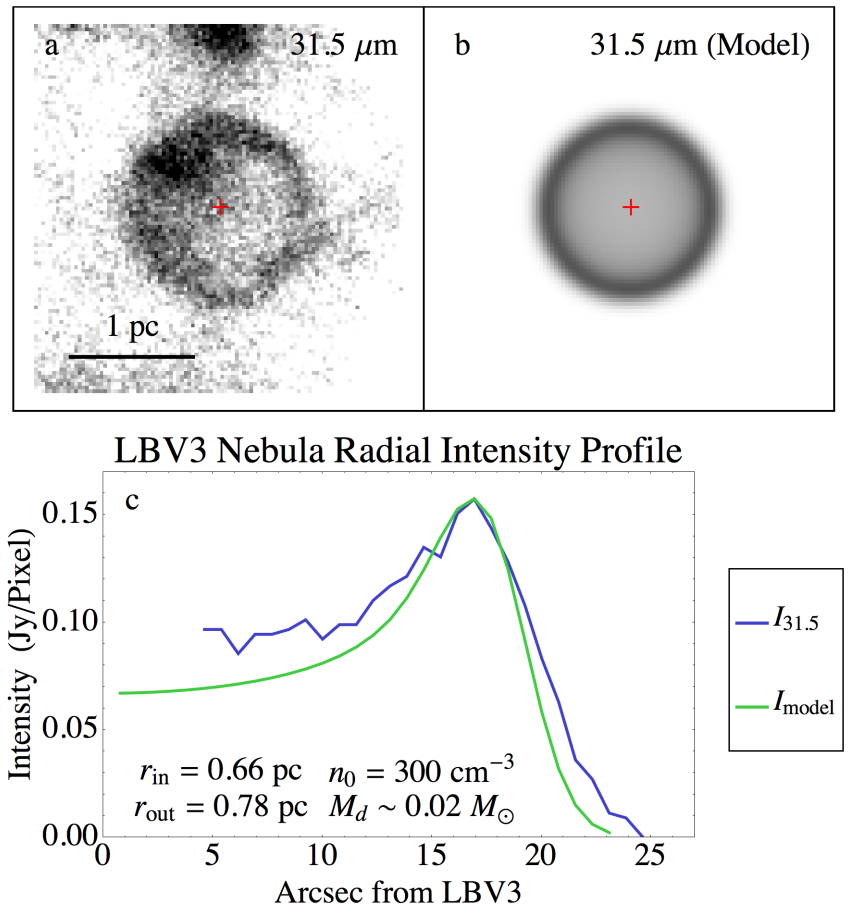

Figure 3.7: (a) Observed 31.5 μm image of the LBV3 nebula. (b) 31.5 μm symmetric shell intensity model. (c) Azimuthally averaged radial intensity profile of the LBV3 nebula extracted from the observed and modeled 31.5 μm images; the northeast quadrant of the nebula has been ignored in determining the observed radial profile.

$$\Delta s = \left(\frac{N_{\mathrm{LyC}}}{4/3\pi\alpha_B n_e^2} + d_N^3 \right)^{1/3} - d_N \tag{3.4}$$

Given a density of $n_e \sim 700\,cm^{-3}$ for the Pistol nebula, which we derive from the 6 cm flux (Lang, Goss, & Wood 1997) and the volume of the nebula, we find that the ionizing photons can penetrate to a depth of $\sim$ 1.5 pc which is roughly the diameter of the Pistol nebula and an order of magnitude greater than the observed thickness. Even if the nebula were located 5 pc away from

the Quintuplet Cluster stars the Lyman-continuum photons would still be able to fully ionize the nebula. We therefore conclude that the Pistol nebula must be entirely ionized.

For the LBV3 nebula we determine an ionization depth of ~ 1.2 pc assuming a density of $n_e \sim 300\, cm^{-3}$ and that the Arches Cluster produces 4×10^{51} ionizing photons per second. Despite the fact that the dust in the LBV3 nebula is primarily heated by the central star, the nebula is fully ionized externally assuming that the Lyman-continuum flux originates from the Arches Cluster as we have argued in Sec 3.3.1.

3.4.3 Evolution of the LBV Nebulae

Both the Pistol and LBV3 nebulae exhibit similar sizes ($r \sim 0.7$ pc), indicating that they also share similar dynamical timescales. An expansion velocity of 60 km/s (Figer et al. 1999), which is not unlike those found for other LBV nebulae (Kochanek 2011), gives a dynamical timescale of $\sim 10^4$ yrs.

We interpret the nebulae as being primarily composed of dust and gas formed in the outflows of the stars rather than being swept-up interstellar material. As suggested by Lamers et al. (2001), the medium surrounding LBVs has been evacuated by the winds during their main-sequence phase and therefore exhibits densities of $\sim 10^{-3}$ cm^{-3}. This implies that for a spherical nebula with a radius of 0.7 pc a total of only $3.5 \times 10^{-5}\, M_\odot$ of material will be swept up, which is significantly less than their estimated total mass ($\sim 6 - 9\, M_\odot$). Additionally, in the case of the Pistol nebula, Lang et al. (1997) find an enhancement of helium with respect to the nearby Sickle HII region which suggests a stellar origin.

In the following subsections we address the distinguishing characteristics of all three LBVs in the context of their evolution and environment.

Dust Formation in LBV Outbursts

Dust production around massive stars poses a difficult challenge to explain, given their greater luminosities and effective temperatures. We suggest that the formation scenario of the dust in the LBV nebulae is that proposed by Kochanek (2011): dust is formed during a short outburst phase ($\sim$ 1000 yrs) of the LBV with extreme mass-loss rates ($\sim 10^{-3}\,M_{\odot}$) and dense winds to shield dust formation regions from UV photons that would otherwise photoevaporate the small grains. In their quiescent state LBVs have too high an effective temperature ($\sim$ 15000 K) and too low a mass loss rate ($\sim 10^{-5}\,M_{\odot}/yr$) for dust grains to form or survive. LBVs may also exist in cool states where they expand and exhibit effective temperatures of $\sim$ 7000 K; however, the soft UV photons will still photoevaporate small grains and thus impede dust formation. We therefore require a high mass-loss rate to both initiate the collisional growth of the dust grains as well as produce a dense wind to shield the grains. From the momentum conservation of the radiatively-driven winds, $\dot{M}v_{\infty} \sim \tau_V L/c$, where τ_V is the optical depth of the winds and L is the luminosity of the star. In order for the winds to be self-shielding we require $\tau_V \gtrsim 1$; therefore, for a star with $L = 10^6\,L_{\odot}$ and $v_{\infty} = 100$ km/s, $\dot{M}$ must be $\gtrsim 10^{-3.5}\,M_{\odot}$. Since the swept-up mass is negligible, the size, mass, and expansion velocity of the nebulae reflects the history of the mass-loss rate from the LBVs.

Maximum Grain Size and Mass Loss Rate

From the maximum grain size it is possible to approximate the mass-loss rate during grain formation, assuming the grains grow by accretion of gas particles with mass m_g (Kochanek 2011). Assuming 100% sticking probability, the collisional growth rate can be expressed as

$$\frac{dN}{dt} = \frac{\dot{M} X_g \, \pi a^2 \, v_t}{4\pi R^2 \, v_w \, m_g}, \tag{3.5}$$

where $\dot{M}$ is the mass-loss rate, X_g is the mass fraction of the condensible dust species, v_t is the thermal velocity of the particles, and v_w is the velocity of the stellar winds. The number of collisions with the gas particles can be related to the grain size by $N = \frac{\frac{4}{3}\pi a^3 \rho_b}{m_g}$, where ρ_b is the bulk density of a grain (~3 gm cm^{-3}), and we can then derive the grain growth rate as

$$\frac{da}{dt} = \frac{\dot{M} X_g \, v_t}{16\pi R^2 \, v_w \, \rho_b}. \tag{3.6}$$

Since the gas will cool as it expands, v_t can be expressed in terms of R, the radius, and R_f, the grain formation radius (~ 10^{15} pc), as $v_t(R) = v_{t0} \left(\frac{R}{R_f}\right)^{-n}$, where $n = 2/3$ for cooling by adiabatic expansion (Kochanek 2011). After integrating, the grain size as a function of radius can be expressed as

$$a(R) \approx \frac{\dot{M} X_g \, v_{t0}}{16\pi R_f v_w^2 \rho_b \, (1 + 2/3)} \left[1 - \left(\frac{R_f}{R}\right)^{1+2/3}\right]. \tag{3.7}$$

Assuming that the grains stop growing and reach their maximum size when the growth rate drops to 10% of the initial rate, or at a distance of $R \simeq 3R_f$, we find that

$$a_{\max} \sim 60 \left(\frac{\dot{M}}{10^{-3}\, M_{\odot}/yr}\right)\left(\frac{X_g}{0.003}\right)\left(\frac{v_{t0}}{1\,\mathrm{km/s}}\right)\left(\frac{100\,\mathrm{km/s}}{v_w}\right)^2 \text{ Å}. \tag{3.8}$$

Dust Evolution in the Pistol Nebula

We suggest that the Pistol star produced silicate grains with sizes ranging from 10 – 60 Å during the outburst that formed the nebula. The selection of this size distribution is based on the parameters of the SED fit to the southern region of the nebula (Fig. 3.5) which appears to be freely expanding with little or no interaction with the winds from the nearby, northern WC stars.

We estimate a mass-loss rate of $\sim 10^{-3}\ M_{\odot}$/yr during the nebula's dust forming phase from Eq. 3.8, assuming that $a_{\max} = 60$ Å, $X_g = 0.003$, $v_{t0} = 1$ km/s, $R_f \sim 10^{15}$ pc, $v_w = 100$ km/s and $\rho_b = 3$ g cm^{-3}. Although this mass-loss rate implies the duration of the dust production is about the dynamical timescale of the nebula, given a total nebular mass of ~9 $M_{\odot}$, we note that in our derivation of the grain growth rate we assumed 100% sticking probabilities for the grain collisions and ignored the possible exhaustion of the condensible species. This mass-loss rate should therefore be treated as a lower limit.

The gradient of decreasing maximum grain size from the south to the north of the Pistol nebula (Fig. 3.5e) suggests that the grains are being sputtered by the high velocity $v_w \sim 2000$ km/s winds from the nearby WC stars north of the nebula. A grain encountering the WC star winds of velocity, v_{WC}, is sputtered at a rate of

$$\frac{dN}{dt} = 2\pi\, a\, v_{WC}\, n_H\, A_i\, Y_i(E_i), \tag{3.9}$$

where a is the grain size, n_H is the hydrogen density of the wind, A_i is the sputtering ion abundance, and $Y_i(E_i)$ is the sputtering yield as a function of sputtering ion's kinetic energy, E_i. The rate the grain size decreases can then be given by

$$\frac{da}{dt} = \frac{m_g}{2\rho_b} v_{WC}\, n_H\, A_i\, Y_i(E_i), \tag{3.10}$$

where m_g is the mass of the sputtered atom and ρ_b is the bulk density of the grain.

With the analytically derived sputtering yields from Tielens et al. (1994) we find that the total change in grain size due to sputtering from the WC winds over 10^4 yrs is $\sim$ 20 Å at the north of the nebula, assuming a fixed distance of 1 pc from the WC stars (a factor of $\sqrt{2}$ times the projected distance). With a varying separation distance between the WC stars and the northern edge of the nebula (2 to 1 pc) based on the expansion velocity of the nebula (Figer et al. 1999), we determine a grain size decrease of $\sim$ 15 Å, which is similar to our fixed distance calculation.

Our calculated grain size change due to sputtering is consistent with the difference in the maximum grain sizes we observe between the northern and the southern regions of the nebula (Fig. 3.5c and e). The preferential sputtering at the north will lead to a deficit of grains in that region, which is what we observe based on the fractional column density around the Pistol Star (Fig. 3.4d).

Pistol Nebula Dust Dynamics

The geometry of our interpretation of the nebula and WC wind interaction agrees with the observed compression at the north of the nebula. Assuming

the WC stars decelerate the projected northern portion of the nebula as it does the back side, we expect a northern expansion velocity of $\sim$ 10 km/s (Figer et al. 1999). From the observed initial and final nebula expansion velocities we can approximate the deceleration of the northern edge and derive the expected distance from the Pistol Star after 10^4 yrs. The initial expansion velocity, v_{N0}, is approximated as the Pistol star wind velocity (100 km/s; Figer et al. 1999 & Mauerhan et al. 2010) and the final expansion velocity, v'_{N0}, is the observed value of 10 km/s (Figer et al. 1999). We therefore predict the northern edge to be $\sim$ 0.5 pc from the Pistol Star, which is consistent with the observations.

Using conservation of momentum we derive the following expression for the total mass of the WC winds, M_w, required to decelerate the northern edge:

$$M_w = M_{p,N}\left(\frac{v_{N0} - v'_{N0}}{v_w - v'_{N0}}\right) = M_{p,N} \times 0.045. \tag{3.11}$$

$M_{p,N}$ is the mass of the northern half of the nebula, and v_w is the WC wind velocity. Assuming that $M_{p,N} \sim 4.5\ M_\odot$, half of the observed total nebula mass, the northern edge must encounter $\sim 0.2\ M_\odot$ of particles from the WC winds. The mass flux from the WC winds through the solid angle of the nebula is $\sim 0.12 \times 10^{-4}\ M_\odot$/yr given a WC mass-loss rate of $10^{-4}\ M_\odot$/yr; therefore, over 10^4 yrs we approximate the total WC wind mass swept up by the northern edge of the nebula to be $\sim 0.12\ M_\odot$, which agrees with the M_w derived from Eq. 3.11.

The Pistol Nebula vs the LBV3 Nebula

Unlike the Pistol nebula, the LBV3 nebula freely expands into its surroundings since there are no nearby stars with strong winds that will interact with the neb-

ula. Due to the lack of near and mid-IR detections of the nebula we are unable to tightly constrain its grain size distribution; however, the distribution of our model fit of the southern Pistol nebula SED ($\sim$ 10 – 60 Å) lies within the 1-σ constraints derived from the DustEM model fits to the LBV nebula SED. The sputtered distribution of the northern Pistol nebula (10 – 25 Å) does not fall within the constraints (Fig. 3.6c). Given the similar nature of the stars themselves (Mauerhan et al. 2010), we may therefore treat the LBV3 nebula as an identical twin to the Pistol nebula with the differences in their appearances only due to the influence of the surrounding environment. Besides the sputtering and compression from external winds, the same evolutionary arguments made for the Pistol can be applied to LBV3.

Non-detection of a qF362 Nebula

There are multiple explanations for the non-detection of nebular emission surrounding qF362, for example: the star has already ejected a nebula that is too diffuse to detect, it has undergone an outburst with a mass-loss rate too low to form grains, or it is less evolved than the Pistol and LBV3 and has yet to go through an outburst phase. Although we cannot test all the cases we can rule out and comment on the feasibility of several of them given the history of H-recombination line observations.

We first address the possibility that qF362 may have already formed a nebula that is now too diffuse for detection. From the expression for the optical depth of a dusty shell, $\tau_V = \frac{M\kappa_V}{4\pi v_{exp}^2 t^2}$, where M is the mass of the shell and κ_V ($\sim$ 100 $cm^2\ g^{-1}$) is the visual opacity of the dust, we can estimate the timescale, t, for detectability. Assuming that the nebula has properties similar to the LBV3 and

Pistol nebulae ($M \sim 6\ M_{\odot}$ and $v_{exp} \sim 70$ km/s) and that we can detect the nebula until $\tau_V = 0.01$, the average optical depth of the Pistol nebula, it should be observable for $\sim 1.5 \times 10^4$ yrs. If indeed the LBV lifetime is $\sim 10^4$ yrs we rule out the possibility of qF362 having formed already formed such a nebula.

The recent HST/NICMOS Paschen-α observations (Dong et al. 2011) taken in June 2008 reveal that, unlike the Pistol and LBV3, qF362 is not producing a strong Paschen-α emission line; however, from May 1999 spectral observations of qF362 in the H and K band, Najarro et al. (2009) found that it had similar H-recombination line strengths to that of the Pistol Star. This implies that qF362 is either expanding and cooling or entering an outburst phase of increased mass-loss.

If it is currently undergoing dust formation we would expect the flux at 8 and 19.7 μm of the optically thick dust shell surrounding the star to be $\sim$ 170 and $\sim$ 40 Jy, respectively, assuming it has a radius of 10^{15} cm, the formation radius, and a temperature of 1500 K. We conclude that dust is unlikely to be forming since a source with a 19.7 flux of 40 Jy would be easily detectable given our integration time and sensitivity. The 8 μm Spitzer/IRAC only detects a 2.2 Jy source at the location of qF362 (Stolovy et al. 2006) which is more consistent with a star having a luminosity and effective temperature identical to that of the Pistol.

3.5 Conclusions

We have presented imaging of the Pistol and LBV3 nebulae at 19.7, 25.2, 31.5, and 37.1 μm, tracing the warm dust emission. Our conclusions on the proper-

ties and evolution of the LBV3 and Pistol nebulae are summarized in Tab. 3.5. The analysis suggests that both nebulae formed under very similar stellar conditions; however, the differences in their surrounding environments have differentiated their morphologies. Due to its proximity to the Quintuplet Cluster, the dust in the Pistol nebula is luminous, compressed, and externally heated while the dust in the LBV3 nebula is dim, symmetric, and centrally heated. Interestingly, the gas in the LBV3 nebula is externally ionized by the Arches Cluster and possibly the Quintuplet Cluster, while the gas in the Pistol nebula is externally ionized by the Quintuplet Cluster. Both nebulae share identical size scales, gas-to-dust mass ratios, as well as total gas masses.

We hypothesize that the Pistol nebula is composed of a population of very small, transiently-heated grains that are preferentially sputtered at the northern region of the nebula where it is colliding with the high-velocity winds from the nearby WC stars. Although the grain composition is not as well determined for the LBV3 nebula as for the Pistol, we find that the non-sputtered southern grain distribution of the Pistol appears to resemble that of LBV3, and thereby supports our interpretation of LBV3 as a twin of the Pistol nebula.

The non-detection of any emission surrounding qF362 in any the FORCAST wavebands suggests that it is the only one of the three LBVs in the region to not have undergone a dust-forming outburst phase. Any dust that might have been produced by qF362 in sufficient quantities to enshroud the star would have easily been observed by either FORCAST or IRAC.

Table 3.5. Pistol vs LBV3

	Pistol Nebula	**LBV3 Nebula**
Morphology	· Shell-like and compressed at north and west edge. Shaped by interaction with winds from nearby WC stars.	· Shell-like and spherically symmetric about star.
Obs. Dust Properties	· $T_{19/37} \sim 100 - 180$ K decreasing from north to south and $\bar{\tau}_{37} \sim 5 \times 10^{-4}$	· $T_{19/37} \sim 105$ K and $\bar{\tau}_{37} \sim 3.5 \times 10^{-4}$
Ionization	· Externally ionized by Quintuplet Cluster	· Exernally ionized by Arches Cluster and possibly the Quintuplet Cluster
Model Dust Properties	· Composed of silicates with sizes $10 - \sim 25 - 60$ Å with maximum sizes decreasing from the south to the north. · $T_d \sim 125$ K, $M_d \sim 0.03\ M_\odot$, and $L_{\rm IR} \sim 5 \times 10^5\ L_\odot$ · Gas-to-dust mass ratio of 310^{+77}_{-52}	· Composed of silicates with minimum grain size < 600 Å and maximum size $40 - 2700$ Å. · $T_d \sim 95$ K, $M_d \sim 0.02\ M_\odot$, and $L_{\rm IR} \sim 10^5\ L_\odot$ · Gas-to-dust mass ratio of 293^{+73}_{-101}
Nebular Evolution	· Ejected $\sim 10^4$ yrs ago with a mass loss rate of $\sim 10^{-3}\ M_\odot$/yr. · High velocity winds from WC stars decelerate and sputter grains in the northern regions. · Dust heating dominated externally by Quintuplet Cluster	· Ejected $\sim 10^4$ yrs ago with a mass loss rate of $\sim 10^{-3}\ M_\odot$/yr. · Freely expanding · Dust heating dominated centrally by LBV3

CHAPTER 4

DUSTY CRADLES IN A TURBULENT NURSERY: THE SGR A EAST HII REGION COMPLEX NEAR THE GALACTIC CENTER

4.1 Introduction

The extreme environment in the Galactic center presents unique conditions for star formation given the hot, turbulent medium that is influenced by a strong tidal field, cloud-cloud collisions, stellar winds, and supernovae shocks (Morris & Serabyn 1996). At least three young, clusters of massive stars exist within the inner 50 pc of the Galactic center (Nagata et al. 1995; Okuda et al. 1990; Krabbe et al. 1991), which provides strong evidence that the conditions in the region favor sudden events of massive star formation. Because molecular clouds in the central molecular zone require a high density in order to withstand the Galactic tidal force, the most extreme among them are prone to forming such massive clusters (Morris & Serabyn 1996). Recently, however, numerous ($\sim$ 19) isolated Wolf-Rayet and O supergiants were found scattered throughout the inner 50 pc of the Galactic center with no association to the three massive clusters (Dong et al. 2011; Mauerhan et al. 2010; Dong et al. 2012). The existence of both the isolated stars and the massive, young clusters raises interesting questions about the conditions leading to massive star formation in the Galactic center region.

Located 6 pc in projection to the northeast of Sgr A* is a string of three compact HII regions and one ultra compact HII region (Ekers et al. 1983) known as

Submitted to ApJ as Lau, Herter, Morris, and Adams 2014

G-0.02-0.07, or Sgr A East A-D. These HII regions appear coincident with the eastern edge of a prominent north-south ridge in the dense 50 km/s molecular cloud, M-0.02-0.07 (Goss et al. 1985; Serabyn et al. 1992), and exhibit identical radial velocities. Interestingly, this molecular cloud is apparently being impacted at the west by the Sgr A East supernova remnant (SNR); however, the star formation linked to the HII region complex, G-0.02-0.07, is completely unrelated to the SNR based on the dynamics of the SNR and the timescales required for the emergence of the HII regions (Serabyn et al. 1992). Despite not being a product of supernova-triggered star formation, G-0.02-0.07 is of great interest since it is a site of most recent confirmed star formation within $\sim$ 10 pc of the Galactic center.

The HII regions Sgr A East A-D are believed to each host a single late O-type star with stellar temperatures $\sim$ 35000 K (Serabyn et al. 1992) and exhibit ages of $\sim 10^4 - 10^5$ years, with region D being the youngest given its nebular size. Studies of the extinction towards the HII regions suggest that regions A, B, and C lie on the surface of the 50 km/s molecular cloud while region D is more deeply embedded within the cloud (Serabyn et al. 1992; Mills et al. 2011). Observations of the dust emission from the HII regions can therefore aid in characterizing the properties of the heating sources and their interaction with the 50 km/s molecular cloud.

Recently, the HII regions have been studied by Yusef-Zadeh et al. (2010) and Mills et al. (2011) using observations of hot dust and ionized gas. Ground-based observations of the 12.8 μm [NeII] line revealed that the kinematics of regions A - C appear consistent with that of a bow shock produced by eastward moving O-stars through molecular gas, as opposed to a pressure-driven "blister" result-

ing from a large density gradient from the molecular cloud to the surrounding medium (Yusef-Zadeh et al. 2010). Yusef-Zadeh et al. (2010) interpret the dual-lobed structure and the kinematics of region D as the result of a bipolar outflow collimated by an accretion disk. Based on Paschen-α (1.87 μm) observations of region D, Mills et al. (2011) agree with the bipolar outflow interpretation; however, Mills et al. (2011) find that the continuum source seen at 1.87 and 1.90 μm, which is slightly displaced from the 6 cm radio emission peak, is likely the central heating source of the region, as opposed to enhanced emission due to scattered light of a density clump as suggested by Yusef-Zadeh et al. (2010). Mills et al. (2011) generated a high-resolution extinction map of the HII regions that reveals the extinctions towards regions A - C are nearly identical ($A_V \sim 45$) while $A_V \sim 70$ for region D.

In this chapter we present 19.7, 25.2, 31.5, and 37.1 μm observations that trace the warm dust emission of the G-0.02-0.07 complex and reveal the presence of two faint infrared sources to the east of region C. These observations were taken by FORCAST aboard the Stratospheric Observatory for Infrared Astronomy (SOFIA). We discuss the morphology, energetics, and composition of the emitting dust in the G-0.02-0.07 complex to characterize the young stellar objects and explore the star formation environment in a dense molecular cloud at the Galactic center.

4.2 FORCAST Observations

Observations were made using FORCAST (Herter et al. 2012) on the 2.5-m telescope aboard SOFIA. FORCAST is a 256 $\times$ 256 pixel dual-channel, wide-field

mid-infrared camera sensitive from 5 – 40 μm with a plate scale of 0.768″ per pixel and field of view of 3.4′ × 3.2′. The two channels consist of a short wavelength camera (SWC) operating at 5 – 25 μm and a long wavelength camera (LWC) operating at 28 – 40 μm. An internal dichroic beam-splitter enables simultaneous observation from both long and short wavelength cameras. A series of bandpass filters is used to image at selected wavelengths.

SOFIA/FORCAST observations of the Sgr A East HII complex were made on the OC1-B Flight 131 on September 17, 2013 (altitude ~ 39,000 ft.) at 19.7, 25.2, 31.5, and 37.1 μm. Measurements at 19.7 and 31.5 μm, as well as 25.2 and 31.5 μm, were observed simultaneously in dual-channel mode, while the 37.1 μm observations were made in single-channel mode. Chopping and nodding were used to remove the sky and telescope thermal backgrounds. An asymmetric chop pattern was used to place the source on the telescope axis, which eliminates optical aberrations (coma) on the source. The chop throw was 7′ at a frequency of ~ 4 Hz. The off-source chop and nod fields (regions of low mid-infrared Galactic emission) were selected from the Midcourse Space Experiment (MSX) 21 μm image of the Galactic center.

The source was dithered over the focal plane to allow removal of bad pixels and to mitigate response variations. The on-source integration time at each dither position was ~ 10 sec, which includes inefficiencies from chopping. The images were reduced and combined at each wavelength according to the pipeline steps described in Herter et al. (2013). Total on-source integration time was ~ 100 sec at 19.7 and 25.2 μm, ~ 200 sec at 31.5 μm, and ~ 50 sec at 37.1 μm. The quality of the images was consistent with near-diffraction-limited imaging at the longest wavelength; the full width at half maximum (FWHM) of the point

spread function (PSF) was 3.2″ at 19.7 μm and 3.8″ at 37.1 μm.

Calibration of the images was performed by observing standard stars and applying the resulting calibration factors as described in Herter et al. (2013). Color correction factors were negligible ($\lesssim$ 5%) and were therefore not applied. The 1-σ uncertainty in calibration due to photometric error, variation in water vapor overburden, and airmass is ±7%; however, due to flat field variations ($\sim$ 15%), which we are unable to correct for, we conservatively assume a 1-σ uncertainty of ±20%.

4.3 Results and Analysis

A composite, false color image of the Sgr A East HII complex is shown in Fig. 4.1 with the 19.7, 31.5, and 37.1 μm emission corresponding to the colors blue, green, and red, respectively. Fig. 4.2a - d shows the individual-band images of the complex at 19.7, 25.2, 31.5, and 37.1 μm. The image reveals the warm dust emission from the four HII regions, Sgr A East A - D, two newly discovered faint infrared sources (FIRS 1 and 2), and the presence of diffuse dust structures throughout the region. Detections of regions A - D are made with a significance greater than 10-σ above the background and FIRS 1 and 2 are detected at 6-σ above the background. The 1-σ levels at 19.7, 25.2, 31.5, and 37.1 μm are 0.013, 0.032, 0.015, and 0.031 Jy, respectively. Given the high signal-to-noise ratio of the HII regions, we perform a Richardson-Lucy deconvolution routine using a Gaussian with the horizontal (RA) full-width at half maximum (FWHM) of the point-source-like region D to characterize the point spread function (PSF). The deconvolution routine provides a uniform 3.0″ FWHM Gaussian PSF at all

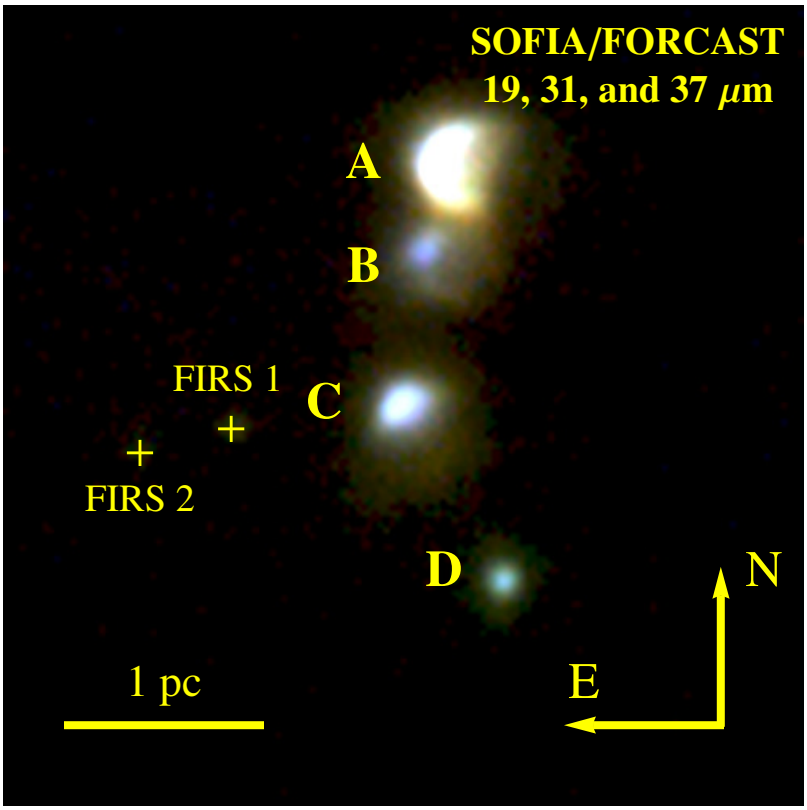

Figure 4.1: 19.7 (blue), 31.5 (green), and 37.1 (red) μm false color image of the Sgr A East HII Complex. The locations of the faint infrared sources (FIRS) 1 and 2 are given by the yellow crosses.

wavelengths.

In this section we present and analyze the morphology, dust energetics, and heating source properties the HII regions and the faint IR sources. Their fluxes and properties are summarized in Tab. 4.1 and Tab. 4.2, respectively. We take the Sgr A East HII complex to be located in the Galactic center at a distance of 8000 pc (Reid 1993).

Table 4.1. Observed fluxes of the Sgr A East HII Regions and Faint IR Sources in Jy

Region	$F_{3.6}$[a]	$F_{4.5}$[a]	$F_{5.8}$[a]	$F_{8.0}$[a]	$F_{12.8}$[b]	$F_{19.7}$	$F_{25.2}$	$F_{31.5}$	$F_{37.1}$
A	0.28	0.40	1.85	5.80		119	271	354	389
B	0.18	0.39	1.16	3.14		35.6	80.5	106	116
C	0.15	0.26	1.05	3.76		57.7	110	120	119
D	0.19	0.75	2.22	4.47	7.50	11.7	32.5	35.3	28.9
FIRS 1	$\lesssim$0.0048	0.055	0.29	0.48		0.63	2.45	3.55	4.00
FIRS 2			0.04	0.10		0.42	2.29	3.02	3.35

[a]Fluxes from Spitzer/IRAC (Stolovy et al. 2006)

[b]Flux from IRTF/TEXES (Yusef-Zadeh et al. 2010)

4.3.1 Interstellar Extinction

Large column densities of dust and gas lead to extreme extinction along lines of sight towards the Galactic center ($A_V \sim 40$; Cardelli et al 1989). We adopt the extinction curve derived by Fritz et al. (2011) from hydrogen recombination line observations of the minispiral, the HII region in the inner 3 pc of the Galactic center, at 1 - 19 μm made by the Short Wave Spectrometer (SWS) on the Infrared Space Observatory (ISO) and the Spectrograph for Integral Field Observations in the Near Infrared (SINFONI) on the Very Large Telescope (VLT). We normalize the Fritz et al. (2011) extinction curve to the $A_{1.87}$ values derived by Mills et al. (2011) in their extinction study of the Sgr A East HII region complex from Paschen-α ($\lambda = 1.87\,\mu$m) and 6 cm observations, yielding $A_{1.87} = 3.7$ for regions A - C. For region D the 1.87 μm extinction is 2 magnitudes greater (Mills et al. 2011).

4.3.2 Dust and Gas Morphology

Regions A - C

The 19.7 - 37.1 μm observations (Fig. 4.2a-d) resolve the extended nature of regions A - C. The dust emission at all the observed IR bands from region A exhibits a semi-circular, limb-brightened morphology with a diameter of $\sim$ 0.45 pc and is the brightest of all the sources in the complex. The ionized gas morphology traced by the Paschen-α emission agrees with the dust morphology at the eastern edge flux peak of the region, as shown in the contour overlay in Fig. 4.3a and the emission line cut profile in Fig. 4.3b; however, the south-north line cut profile (Fig. 4.3c) shows that the 19.7 μm emission at the southern edge decreases by $\sim$ 40% relative to the northern edge. This discrepancy between the 19.7 and 31.5 μm emission profiles strongly suggests a dust temperature gradient decreasing from north to south. Paschen-α emission extends slightly more than the dust into the central cavity.

Region B exhibits a slightly more complete circular morphology than region A, with a diameter of $\sim$ 0.34 pc. The dust emission at all observed IR bands peaks at an identical location on the northeastern edge of region B, but the Paschen-α flux peak is offset by several arcseconds to the west (Fig. 4.3e); however, the 31.5 μm emission peak agrees with the Paschen-α peak at the southern edge. Interestingly, of the three resolved HII regions, B is the only one that exhibits this displacement of the Paschen-α peak with respect to the dust emission peak. Similar to region A, both the 31.5 μm and Paschen-α emission extend further into the center of region B than the 19.7 μm emission.

The dust in region C exhibits an elongated morphology along the southeast

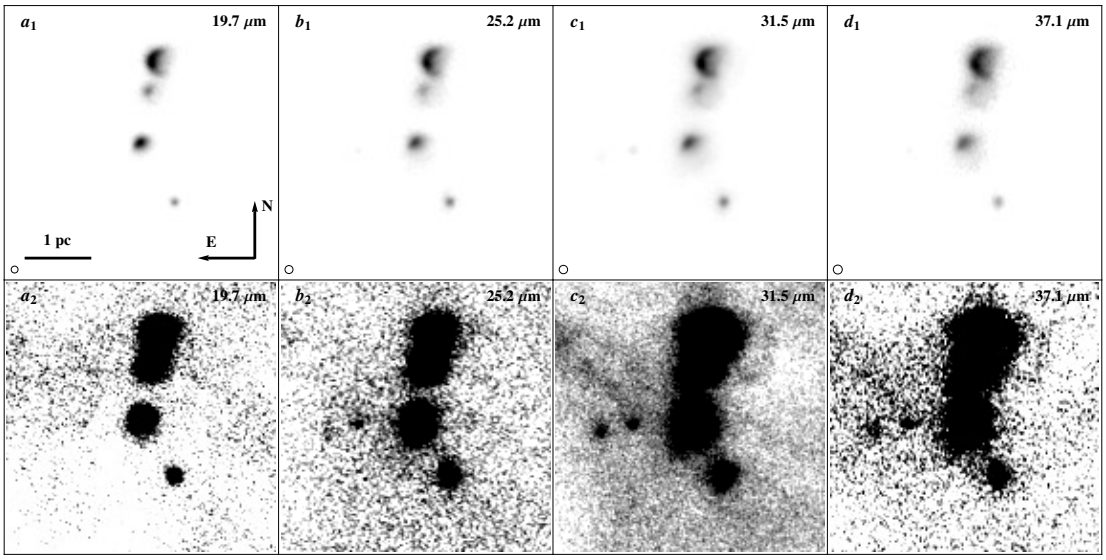

Figure 4.2: Observed (a) 19.7, (b) 25.2, (c) 31.5, and (d) 37.1 μm images of the Sgr A East HII Complex at two different stretches to show bright (top panels) and faint (lower panels) emission. The approximate beamsizes are shown in the lower left corner in each image.

and northwest that appears more extended and concave with increasing wavelength, which is consistent with the concave morphology of the ionized gas. Although the effect is not as pronounced as regions A and B, the 31.5 μm and Paschen-α emission still appears to extend slightly further into the center of curvature of region C than the 19.7 μm emission. A linear filament located $\sim 9.5''$ to the southwest of the dust emission peak of the region is apparent in the Paschen-α emission (Fig. 4.8) and is barely detected in the 31.5 and 37.1 μm maps. This southwestern filament appears elongated parallel to the main, bright segment of C.

Region D and The Faint IR Sources

Region D is the most compact and southern source in the HII complex. The dust in the region exhibits a slight north-south elongation at 31.5 and 37.1 μm:

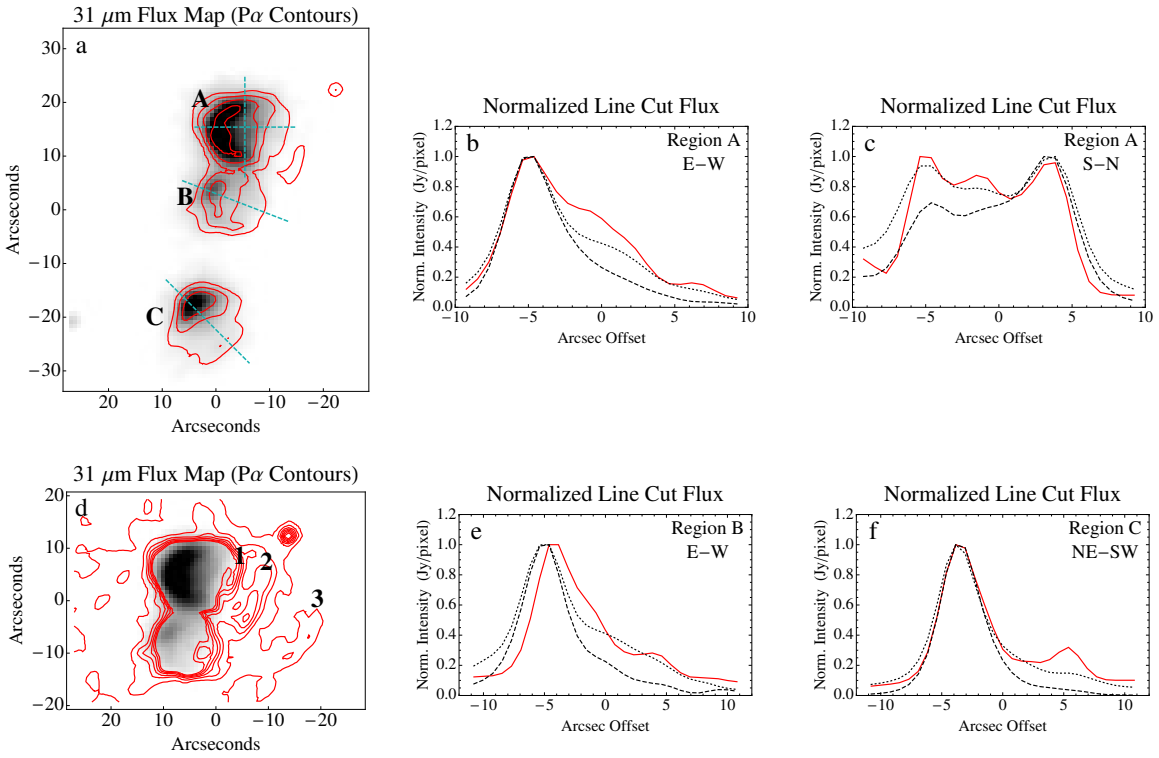

Figure 4.3: (a) Paschen-α contours and line cuts overlaid on the 31.5 μm flux map of the Sgr A East HII Complex and normalized line cut flux plots through regions (b and c) A, (e) B, and (f) C of the Paschen-α (red solid), 19.7 μm (black dashed), and 31.7 μm (black dotted) emission. The Paschen-α emission has been convolved to match the beam size of the deconvolved 19.7 μm and 31.5 μm maps and the Paschen-α contour levels correspond to 0.25, 0.50, 1.0, and 2.0 mJy/pixel. (d) 31 μm flux map zoomed in on regions A and B overlaid with Paschen-α contours labeled with the locations of "ridges" 1, 2, and 3 with levels corresponding to 0.10, 0.15, 0.20, 0.25, 0.30, 0.35, and 0.40 mJy/pixel.

the vertical FWHM is $\sim$ 15% larger than the horizontal FWHM at both wavelengths. At 19.7 and 25.2 μm the vertical FWHM is only $\sim$ 5 – 10% larger than the horizontal FWHM. This elongation observed from the dust emission is consistent with the north-south extension of the ionized gas morphology seen in Paschen-α emission.

Two faint IR sources (FIRS), designated 1 and 2, are detected 23″ and 35″ to the east of region C (Fig. 4.2). FIRS 1 is unresolved and has a $\sim$ 15% greater

far-IR flux (19 - 37 μm; Tab. 4.1) than FIRS 2 which appears partially resolved, with a FWHM of $\sim$ 5.0″ at 31.5 μm. Unlike the four HII regions, there is no detectable ionized gas counterpart in Paschen-α or 6 cm emission (Yusef-Zadeh et al. 1987) for FIRS 1, which suggests the heating source has a relatively cool effective temperature. FIRS 2, however, has a dim, shell-like ionized gas counterpart observed at 6 cm (Zhao, Morris, & Goss 2014) with an angular diameter of $\sim$ 5″, consistent with the 31.5 μm FWHM. Emission from both faint IR sources is detected in the mid-IR at 5.8, and 8.0 μm by Spitzer/IRAC (Stolovy et al. 2006), and only FIRS 1 is observed at 4.5 μm. FIRS 2 is partially resolved At 5.8 and 8.0 μm with a FWHM of $\sim$ 5.0″, which is also consistent with the FWHM observed at 31.5 μm. The Spitzer/IRAC fluxes from FIRS 1 is $\sim 5-8$ times greater than that of FIRS 2. FIRS 1 appears coincident with the southern edge of a long linear filament observed at 31.5 and 37.1 μm southeast of regions A - C (Fig. 4.2c and d; also, see Fig. 3 from Mills et al. 2011). Ionized gas emission is also detected from this filament in Paschen-α, and it has been suggested that the filament traces the surface of the 50 km/s molecular cloud (Mills et al. 2011).

Western "Ridges"

Three faint ionized curved "ridges" are located approximately 7″ (ridge 1), 14″ (ridge 2), and 26″ (ridge 3) to the west of region A (Mills et al. 2011), the most extended of which can be seen in Fig. 4.2c and d in dust emission, and Fig. 4.3d in Paschen-α emission. Only the two furthest ridges from region A are resolved and detected at 31.5 and 37.1 μm at a flux level greater than 4-σ and 2-σ for ridges 2 and 3, respectively. Ridge 1 is confused with the extended dust emission from region A. The dust emission from ridges 2 and 3 extends to angular

Table 4.2. Summary of the Sgr A East HII Complex and FIRS 1 Properties

Region	d (pc)	$T_{\rm d}$[a](K)	L_*[a]($10^4\,L_\odot$)	$L_{\rm IR}/L_*$	$M_{\rm dust}$[a]($M_\odot$)	$\frac{M_{\rm HII}}{M_{\rm dust}}$ [b]	$\frac{Y_{\rm VSG}}{Y_{\rm LG}}$ [a]	$\frac{Y_{\rm PAH}}{Y_{\rm VSG}}$ [a]
A	0.45	100	22	0.74	0.037	60	0.010	0.78
B	0.34	100	19	0.28	0.011	72	0.040	0.28
C		114	7.1	0.19	0.008	50	0.015	0.71
D	0.16*	131	4.7	1.0	0.002	50	0.36	$\lesssim 0.4$
FIRS 1		171	1.6	1.0	0.0002		0.018	$\lesssim 0.03$

Note. — d is the observed diameter of the region, T_d is the the volume-average dust temperature, L_* is the heating source luminosity, $L_{\rm IR}/L_*$ is the integrated IR to heating source luminosity ratio, $M_{\rm dust}$ is the dust mass, $\frac{M_{\rm HII}}{M_{\rm dust}}$ is the gas-to-dust ratio, $\frac{Y_{\rm VSG}}{Y_{\rm LG}}$ is the VSG-to-LG abundance ratio, and $\frac{Y_{\rm PAH}}{Y_{\rm VSG}}$ is the PAH-to-VSG abundance ratio.

[a]Determined by DustEM model fit to the SEDs

[b]$M_{\rm HII}$ derived from free-free/Paschen-α emission (Mills et al. 2011)

*Vertical FWHM

sizes of $\sim 17''$ and $\sim 31''$, respectively, and is roughly cospatial with their apparent Paschen-α counterparts; however, the dust emission from ridge 3 extends further north and arcs back towards region A, whereas its Paschen-α counterpart appears to end at the same declination as the southern edge of region A.

The Paschen-α and 6 cm emission measurements of ridges 2 and 3 indicate that there is additional extinction along lines of sight towards ridge 3. Extinction estimates towards ridge 2 are found to be nearly identical to that of regions A - C, which appears consistent with the extinction map produced by Mills et al. (2011). The 1.87 μm extinction increases by $\Delta\tau_{P_\alpha} \lesssim 0.8$ magnitudes between ridges 2 and 3. Comparison of the 1.87 μm extinction between ridges 1 and 2 reveals that ridge 1 has $\sim 0.6 \pm 0.2$ magnitudes less extinction. It is important to note that the non-thermal radio emission from the supernova remnant Sgr A

Table 4.3. Dust Properties of the Region A "Ridges"

Ridge	$d_{\rm proj}$ (pc)	$T_{31/37}$ (K)	T_{eq} (K)	τ_{37}	A_{P_α}
1	0.4				3.1 ± 0.2
2	0.5	64 ± 4	60	~ 0.01	3.7 ± 0.2
3	1.0	40 ± 4	47	$\gtrsim 0.04$	$\lesssim 4.5$

Note. — $d_{\rm proj}$ is projected distance of the ridges from region A, $T_{31/37}$ is the observed 31/37 color temperature, T_{eq} is the predicted dust temperature assuming a distance of $d_{\rm proj}$ multiplied by a $\sqrt{2}$ projection factor, τ_{37} is the 37.1 μm optical depth, and A_{P_α} is the extinction magnitude at 1.87 μm.

East may be contaminating the thermal emission from ridge 3. A subtraction of the non-thermal emission was attempted when calculating the extinction; however, there are large uncertainties since the emission is non-uniform and the extinction towards ridge 3 should therefore be treated as an upper limit. The projected locations, extinction, dust properties of the ridges are provided in Tab. 4.3.

4.3.3 Color Temperature and Optical Depth

The color temperature maps are derived from the ratio of the deconvolved 19.7 and 37.1 μm flux maps assuming the emission is optically thin and takes the form of $F_\nu \propto B_\nu(T_d)\,\nu^\beta$, where a value of 2 for β is adopted. With the dust temperature and deconvolved 37.1 μm flux maps, the 37.1 μm optical depth over the pixel solid angle, Ω_p, is simply:

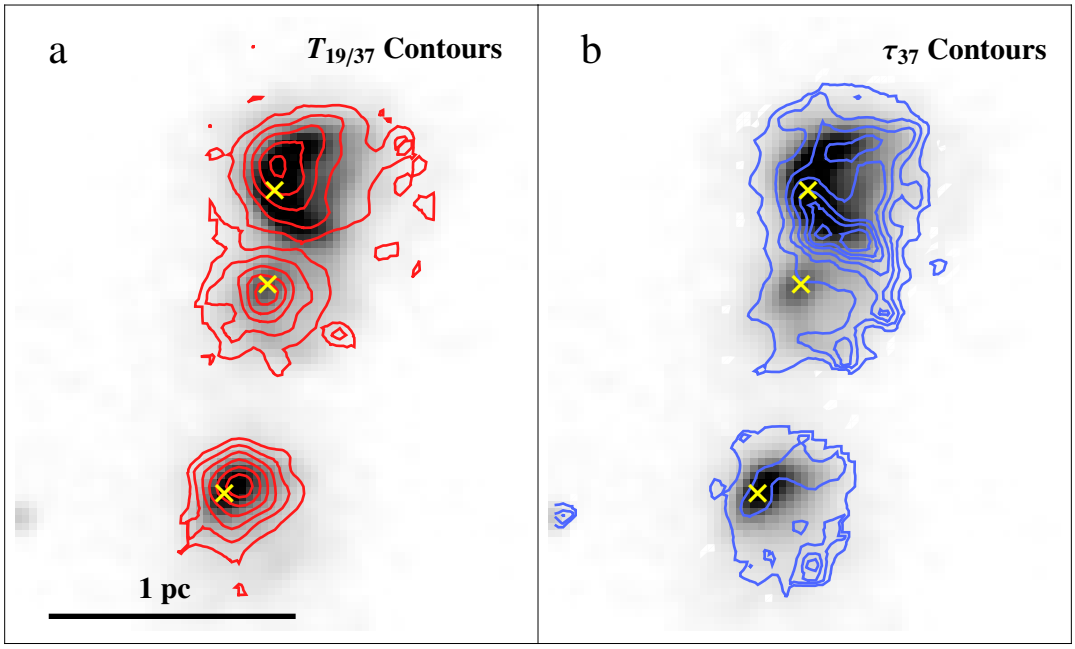

Figure 4.4: 31 μm flux map of the Sgr A East HII Complex overlaid with contours of the (a) 19/37 dust temperature and (b) 37 μm optical depth. The location of the 31 μm flux peak in each region is indicated by the yellow cross. The levels of the temperature contours correspond to 90, 100, 110, 120, 130, and 140 K. The levels of the 37 μm optical depth contours correspond to 0.001, 0.0025, 0.004, 0.0055, 0.0075, 0.009, and 0.011.

$$\tau_{37.1} = \frac{F_{37.1}}{\Omega_p \, B_\nu(T_d)}. \tag{4.1}$$

The color temperature and column density contours of the complex are overlaid on the 31.5 μm flux map in Fig. 4.4.

The color temperature of region A peaks at a value of 135 K at the location $\sim$ 4″ north of the dust emission peak at the eastern edge, and exhibits an average temperature of 107 ± 7 K. Westward of the peak, the temperature of region A decreases approximately linearly to a value of $\sim$ 90 K at a distance of 12″ from the peak. The symmetry of the color temperature map is significantly different from the 31.5 μm emission map: the dust emitting at the north is $\sim$ 15 K hotter than the dust at the south while the flux from those regions are similar within

$\sim$ 15%.

The 37.1 μm optical depth of region A peaks at the southern edge of the dust emission at a value of $\sim$ 0.011. Northwards and clockwise along the emitting dust, the optical depth decreases to a minimum of $\sim$ 0.005 at approximately the 10 o'clock position and then increases to $\sim$ 0.006 at 11 and 12 o'clock positions along the northern edge. Despite the symmetry of the dust emission at 31.5 μm, a majority of the dust is located at the southern edge of the region. Similar to the dust emission intensity, the optical depth sharply decreases to the east of the region. To the west of the center of curvature there is a slight increase in the optical depth before falling off sharply.

Region B exhibits a color temperature peak of 135 K located at the northeast dust emission edge of the region and within $\sim$ 2″ of the dust emission intensity peak. The average temperature is similar to that of region A at a value of 106 ± 6 K. The temperature decreases symmetrically in all directions to a value of $\sim$ 85 K at a location 7″ from the peak. Interestingly, the 37.1 μm optical depth of region B appears almost perfectly anti-correlated with both the dust and ionized gas emission. The dust and ionized gas emission peak along the eastern edge of the region; however, the optical depth is lowest at the east and increases towards the west along the rim of the shell to values $\sim$ 3 times that of the east.

The dust temperature of region C peaks at a value of 145 K and is consistent with the location of the Paschen-α emission peak, but is slightly offset by $\sim$ 3″ to the northwest of the dust emission peak. The region exhibits an average temperature of 115 $\pm$ 10 K and decreases to $\sim$ 75 K at the linear filament to the southwest (Fig. 4.3f and Fig. 4.8c). The 37.1 μm optical depth contours trace the concave morphology of the Paschen-α and dust emission. At the southwest fil-

ament the optical depth is approximately twice that of the brighter, main region in C, which is similar to what is observed in region B.

After correcting for the additional extinction ($\Delta A_{P\alpha} \sim 2$; Mills et al. 2011), region D exhibits a 19/37 color temperature of 130 K. Assuming the extinction towards FIRS 1 and 2 is identical to that of regions A - C, they would both exhibit color temperatures of $\sim$ 90 K. However, dust models fit to the SEDs of FIRS 1 suggest that there is much more intervening dust than along the lines of sight towards Region A - C ($\Delta A_{P\alpha} \sim 7$; Sec. 4.3.4). Dereddening the 19 and 37 μm flux of FIRS 1 with $\Delta A_{P\alpha} \sim 7$ provides a 19/37 color temperature of 173 K.

The 31/37 color temperatures of ridges 2 and 3, located to the west of region A, decrease with projected distance from region A: ridges 2 and 3 exhibit temperatures of 63 and 40 K, respectively. The 37.1 μm optical depths increase with projected distance from region A: ridges 2 and 3 are $\sim$ 0.01 and $\gtrsim$ 0.04, respectively. Since 37.1 μm is far on the Wien side of the Planck function at a temperature of $T = 40$ K and the uncertainty in the 31/37 color temperature is $\pm$4 K, the 37.1 μm optical depth for ridge 3 is not well constrained; however, even at the lower limit the 37.1 μm optical depth of ridge 3 is still a factor of 4 times greater than that of ridge 2.

4.3.4 SEDs and Dust Modeling

To better understand the nature of the grains and their thermal behavior, we construct physical models of the grain energy balance and subsequent emission spectrum with the aim of reproducing the observed SEDs. This is done for both spatially integrated SEDs for all the sources (Fig. 4.5) and for selected regions

of A (Fig. 4.6). A detailed spatial model for A is constructed based on the dust properties of the regional models (Fig. 4.7). Details of the models and the resulting constraint on dust properties are given in this section.

Evidence of Very Small Grains

The inclusion of the mid-IR observations of the HII regions and FIRS 1 taken by Spitzer/IRAC (Stolovy et al. 2006) in their SEDs (Fig. 4.5) reveals that dust models composed of a distribution of strictly large grains ($a = 100 - 1000\,\text{Å}$; dotted yellow line in Fig. 4.5b - f), which agree with the observed flux at 19 - 37 μm, fail to fit the observed flux at 3.6 - 8 μm by more than an order of magnitude. The enhanced emission at the IRAC wavelengths is attributed to the presence of very small ($a < 100\,\text{Å}$), transiently heated grains in the region. Very small grains (VSGs) such as Polycyclic Aromatic Hydrocarbons (PAHs; $a \sim 4 - 12\,\text{Å}$) can reach temperatures much greater than equilibrium-heated large grains since they have small heat capacities that result in large temperature spikes after absorbing single photons. The emissivity of small grains can be characterized as

$$j_\nu = \int \mathrm{d}a \frac{\mathrm{d}n}{\mathrm{d}a} \int \mathrm{d}T \left(\frac{\mathrm{d}P}{\mathrm{d}T}\right)_a \sigma_{\text{abs}}(\nu, a) B_\nu(T), \tag{4.2}$$

where n is the dust density and $\frac{\mathrm{d}P}{\mathrm{d}T}$ is a probability distribution function with $P(T)$ being the probability that a grain will have a temperature less than or equal to T. For large grains in radiative equilibrium the probability distribution function is simply a delta function at the equilibrium temperature. The steady state probability distribution function for small grains, which is much broader than the large grain function, can be solved for analytically (Guhathakurta & Draine

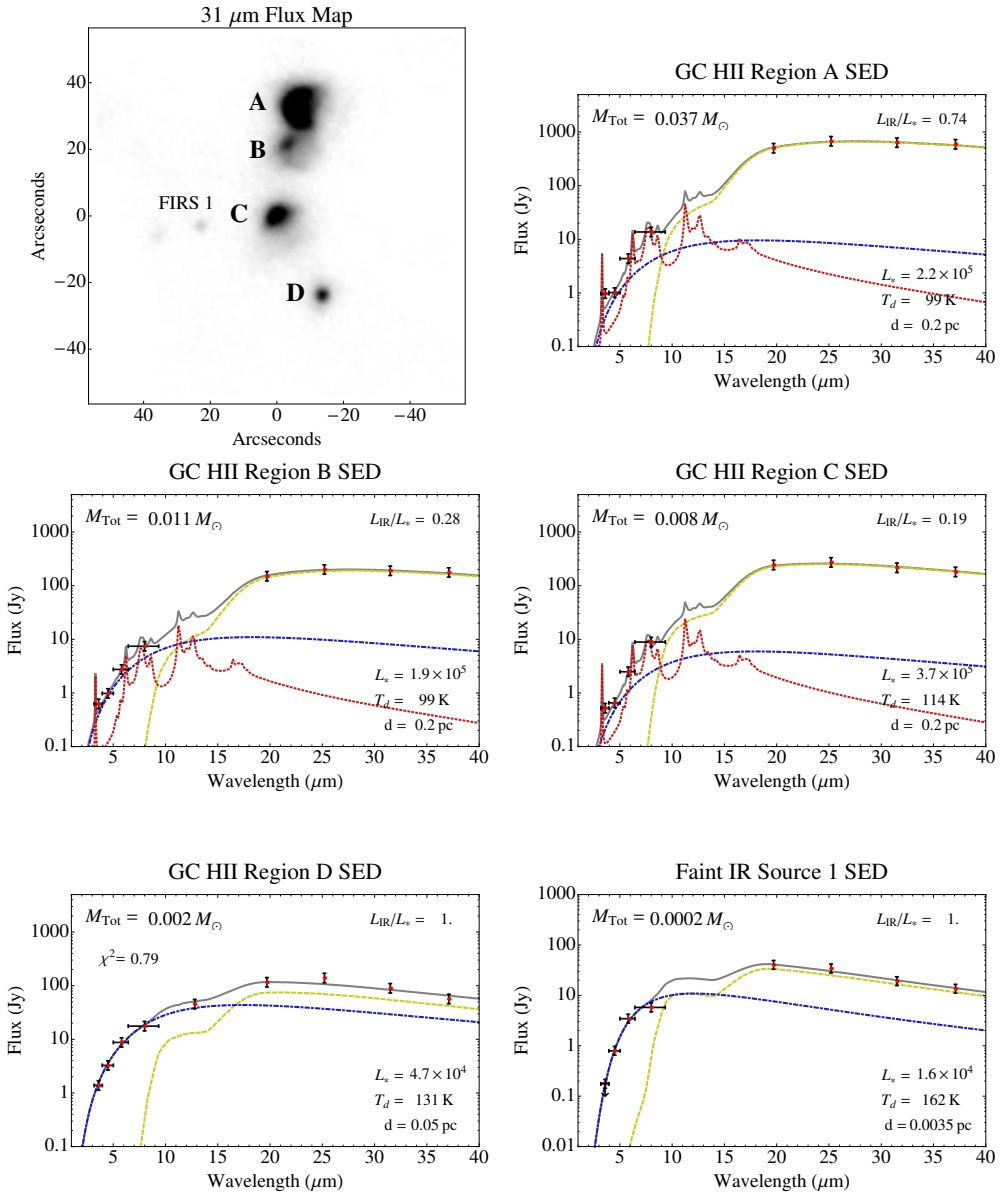

Figure 4.5: 31 μm flux map of the Sgr A East HII Complex and DustEM fits (solid grey line) to the dereddened SEDs of regions A - D and the FIRS 1. The DustEM models of regions A - D assume the dust is composed of LGs (a_{LG} : 100 – 1000 Å;), VSGs (a_{VSG} : 6 – 25 Å), and PAHs (a_{PAH} : 6 – 10 Å). DustEM models of FIRS 1 assume the same dust composition as the HII region models except the maximum grain size cutoff of the VSGs is 100 Å. The dotted red lines, dot-dashed blue lines, and dashed yellow lines correspond to the PAH, VSG, and LG emission components, respectively. The total dust mass, $M_{\rm Tot}$, and the infrared to total heating source luminosity ratio, L_{IR}/L_*, are given at the top of each plot. The heating source luminosity, L_*, the volume-average dust temperature, T_d, and the distance between the heating source and the dust, d, are given at the bottom right of each plot.

1989; Draine & Li 2001).

DustEM SED Models

The DustEM code (Compiègne et al. 2011) is utilized to model the SEDs of the HII regions and the faint IR sources. DustEM is capable of modeling the emission from stochastically heated VSGs using the formalism of Desert et al. (1986) to derive the temperature probability function of the grains. In the models, it is assumed that there are three populations of dust in the region: large silicate grains (LGs), VSGs composed of carbonaceous material, and PAHs. For the models of regions A - D, the LGs, VSGs, and PAHs have sizes ranging from 100 - 1000 Å, 6 - 25 Å, and 6 - 10 Å respectively. VSG size distributions with larger upper grain size cutoffs such as $a_{\rm max}$ = 100 μm result in very poor or physically unreasonable fits to the SEDs of regions B and D. Regions A and C models with an upper VSG size cutoff of 100 μm do not predict the same dust abundances as the $a_{\rm max}$ = 25 μm models; however, they predict dust temperatures, stellar luminosities, and dust masses identical to the $a_{\rm max}$ = 25 μm models. The dust model for FIRS 1 is identical to the previous models except the VSGs range from 6 - 100 Å in size since the 6 - 25 Å VSG model over-predicts the emission at 3.6 μm. The minimum grain sizes for the VSGs and PAHs are determined such that their maximum temperature reached is less than their sublimation temperatures, which is $\sim$ 1800 K for the carbonaceous VSGs and $\sim$ 1500 K for PAHs (Draine 2011).

A grain size distribution power-law index of $\alpha = -3$, which is similar to the index adopted for the interstellar dust model from Desert et al. (1990), is assumed for all the grain populations. A standard MRN distribution grain size

power law index of $\alpha = -3.5$ provides similar results to $\alpha = -3$. Castelli & Kurucz (2004) stellar atmospheres are utilized to model the radiation field heating the dust. An O7 model is assumed for the source heating region A, O8.5 for regions B and C, and O9 for region D (Mills et al. 2011; Martins et al. 2005). Since there is no radio or Paschen-α counterpart to FIRS 1, which indicates the absence of ionized gas, a $T_* = 7000$ K blackbody stellar atmosphere is adopted for the FIRS 1 heating source.

For regions A - C, the DustEM models are fit to the SEDs with the stellar luminosity, L_*, and the grain mass abundances $Y_{\rm LG}$, $Y_{\rm VSG}$, and $Y_{\rm PAH}$ as free parameters, and the dust is assumed to be confined to a shell located 0.2 pc from the heating source. The free parameters for the region D models are similar to those of the regions A - C models, where the differences are the inclusion of the heating source distance as a free parameter and fixing the $L_{\rm IR}/L_*$ ratio to a value of 1 since region D is likely embedded in the molecular cloud. The FIRS 1 models include the same free parameters as the region D models as well as an additional parameter $\Delta A_{P\alpha}$, the local extinction relative to the extinction along the lines of sight towards regions A - C. Similar to the region D models, the IR to stellar luminosity ratio is fixed at 1 for FIRS 1. Very poor fits resulted from attempts to model the FIRS 2 SED under the assumptions that the heating source is embedded ($L_{\rm IR}/L_* = 1$) and that the emitting dust is confined to a 0.1 pc ($\sim 3''$) radius shell. DustEM analysis of FIRS 2 is omitted in this chapter due to the difficulties of constraining the models to fit its SED; however, this will be addressed in future work with further observations.

The DustEM model fits to the SEDs of the HII regions and FIRS 1 are shown in Fig. 4.5 and the model parameters are given in Tab. 4.2. The dust temperature

provided, T_d, is the volume-average dust temperature,

$$T_d = \frac{\int \mathrm{d}a \frac{\mathrm{d}n}{\mathrm{d}a} T(a)\, m(a)}{\int \mathrm{d}a \frac{\mathrm{d}n}{\mathrm{d}a} m(a)}. \tag{4.3}$$

In the models $dn/da \propto a^{-3}$, and since $m(a) \propto a^3$, Eq. 4.3 can be reduced to

$$T_d = \frac{\int \mathrm{d}a\, T(a)}{\int \mathrm{d}a}. \tag{4.4}$$

The stellar luminosities fit to heating sources of region A - D are consistent with the Lyman continuum flux required to ionize the regions as determined by Mills et al. (2011) from radio observations. The resulting integrated IR to stellar luminosity ratios derived for regions A - C (L_{IR}/L_*), which can be related to the fractional coverage of the dust around the heating source, agree with the apparent dust morphology of each region: A appears as an almost complete spherical shell which suggests a high fractional coverage ($L_{\mathrm{IR}}/L_* \sim 0.74$) while C appears as an arc with a large opening angle which suggests a lower fractional coverage ($L_{\mathrm{IR}}/L_* \sim 0.19$).

Presence of PAHs

The presence of PAHs is required for the DustEM model fits to the SEDs of regions A - C due to the enhanced 3.6 μm emission. The Spitzer/IRAC bandwidth of the 3.6 μm filter includes the 3.3 μm PAH feature. Without PAHs in the dust models, the VSG emission alone would fall short by greater than an order of magnitude from the observed 3.6 μm emission. As can be seen in Fig. 4.5, the fits to the region D and FIRS 1 SEDs do not require any PAHs; however, the 1-σ upper limit of $\frac{Y_{\mathrm{PAH}}}{Y_{\mathrm{VSG}}}$ for region D is as high as ~ 0.4, which is comparable to

$\frac{Y_{\rm PAH}}{Y_{\rm VSG}}$ for regions A - C. The disparity of PAHs is more constrained in the FIRS 1 models, where the 1-σ upper limit of $\frac{Y_{\rm PAH}}{Y_{\rm VSG}}$ is ~ 0.03.

Relative Extinction Towards Faint IR Source 1

Fits to the FIRS 1 SED require an additional extinction relative to the extinction along the line of sight towards regions A - C, where $A_{P\alpha} = 3.7$ (Mills et al. 2011). In the FIRS 1 models, the additional extinction is taken to be at the Paschen-α wavelength (1.87 μm) and is designated as $\Delta A_{P\alpha}$. The best-fit models for the SED require $\Delta A_{P\alpha} = 7 \pm 2$. Both the upper and lower 1-σ models do not require the presence of PAHs. The estimated luminosity of the heating source is $1.6^{+1.2}_{-0.6} \times 10^4$ $L_\odot$.

Region A SEDs and Heating Source Location

We now determine the location of the heating source in region A. Assuming the composition of the emitting dust does not change appreciably across the source, we can pick three points within the nebula and triangulate the position of the heating source. The distance, d, from the heating source determines its temperature from energy balance, which for spherical, large grains is:

$$\pi a^2 Q_*(a) \frac{L_*}{4\pi d^2} = 4\pi a^2 \, Q_{\rm dust}(T_d, a) \, \sigma_{\rm SB} \, {T_d}^4, \tag{4.5}$$

where $Q_{\rm dust}$ is the dust emission efficiency averaged over the Planck function of dust grains of size a and temperature T_d, Q_* is the dust absorption efficiency averaged over the incident radiation field, and L_* is the total integrated stellar luminosity. Taking silicate grains with a 0.01 μm radius heated radiatively by an

O7 star, the radiation field-averaged absorption efficiency, Q_*, is ~ 0.5 and the dust-averaged emission efficiency can be expressed as $Q_{\rm dust}(a) = 1.3 \times 10^{-7} \frac{a}{0.01\,\mu{\rm m}}$ (Draine 2011).

The location of the heating source is given by the star in Fig. 4.6a and b which is at the intersection of the three annuli that represent the radius from the three regions at which the heating source must be located at to be consistent with the model dust temperature of the 100 Å-sized grains, T_d. The outer and inner dashed rings show the radii at $1 - \sigma$ deviations of the stellar luminosity. Since the highest dust temperatures are exhibited at the north and east of region A, the heating source is inferred to be displaced $\sim 3''$ to the north east of the center of curvature which is consistent with the location of the peak color temperature given by the orange '×'.

DustEM models were fit to the SEDs from the north, east, and south sections of region A (Fig. 4.6). Grain properties, heating source luminosity, and effective temperature were fixed to the values determined for the region A model. The distance from the dust to the heating source is as determined above. The free parameters are the relative abundances of the three grain populations. Local mechanisms that increase with density such as dust backscattering and trapped Lyman-alpha are minor contributors to the heating and thus are not responsible for the dust temperature asymmetry. The dust mass determined at the south is ~ 2 times greater than the mass at the north and east, which agrees with the positive north-south gradient in the 37.1 μm optical depth contours (Fig. 4.4b).

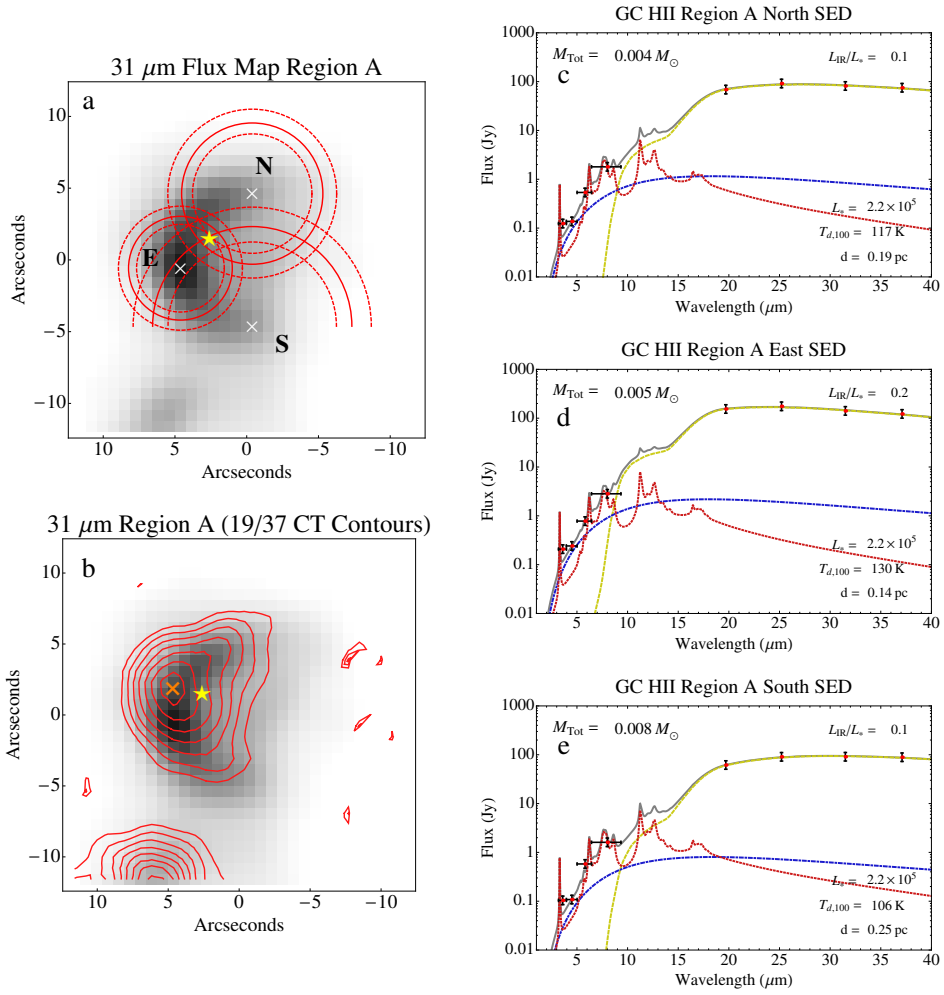

Figure 4.6: (a) 31 μm flux map of region A overlaid with annuli representing the possible locations of the heating source centered on the north, east, and south positions, which are marked by white ×'s. The outer and inner dashed rings represent the 1-σ ($\sim$ 20%) uncertainty in the inferred heating source luminosity. The star indicates the implied location of the heating source, the intersection of the three annuli. (b) 31 μm flux map of region A (greyscale) overlaid with the location of the peak 19/37 color temperature, which is shown as the orange "×", and contours corresponding to 100, 105, 110, 115, 120, 125, and 130 K. (c) - (e) DustEM model fits (solid grey line) to SEDs at the north, east, and south positions of region A . $T_{d,100}$ is the temperature of the 100 Å-sized grains determined by the DustEM models. The dotted red lines, dot-dashed blue lines, and dashed yellow lines correspond to the PAH, VSG, and LG emission components, respectively.

Region A Dust Emission Model

In order to understand the structure and heating of the dust in region A, a dust emission model is generated assuming the dust is arranged in a hemispherical shell and heated by a single O7 star. Three different gas densities are used to model the emission: n_S is the density of the southern half of the shell, n_C the central quarter, and n_N the northern quarter. The densities are related to each other as

$$n_S = 2n_C, n_N = 1.5n_C, \tag{4.6}$$

which is consistent with the relative column densities in the 37.1 μm optical depth map. The other free parameters are the shell thickness, Δt, and inner shell radius, r_0. A fixed, uniform grain size distribution of 0.01 μm-sized silicates with a gas-to-dust mass ratio of 100 and a flat radial density profile across the shell is assumed for the model. The location of the heating source is as determined in the previous section: 3'' to the east and 1'' to the north of the center of curvature. Parameters for the emission model are given in Table 4.4.

The 31 μm emission model, which has been convolved to the resolution of the observed 31 μm map, is shown in Fig. 4.7a and is overlaid with the model 19/31 color temperature contours. Both the color temperature contours and the 31 μm dust emission of the model agree very well with the observed temperature contours and dust emission (Fig. 4.7b), especially the displacement of the emission peak from the temperature peak. Fig. 4.7c shows the close agreement of the vertical (red) and horizontal (blue) line cuts through both the model (solid) and observed (dotted) 31 μm maps.

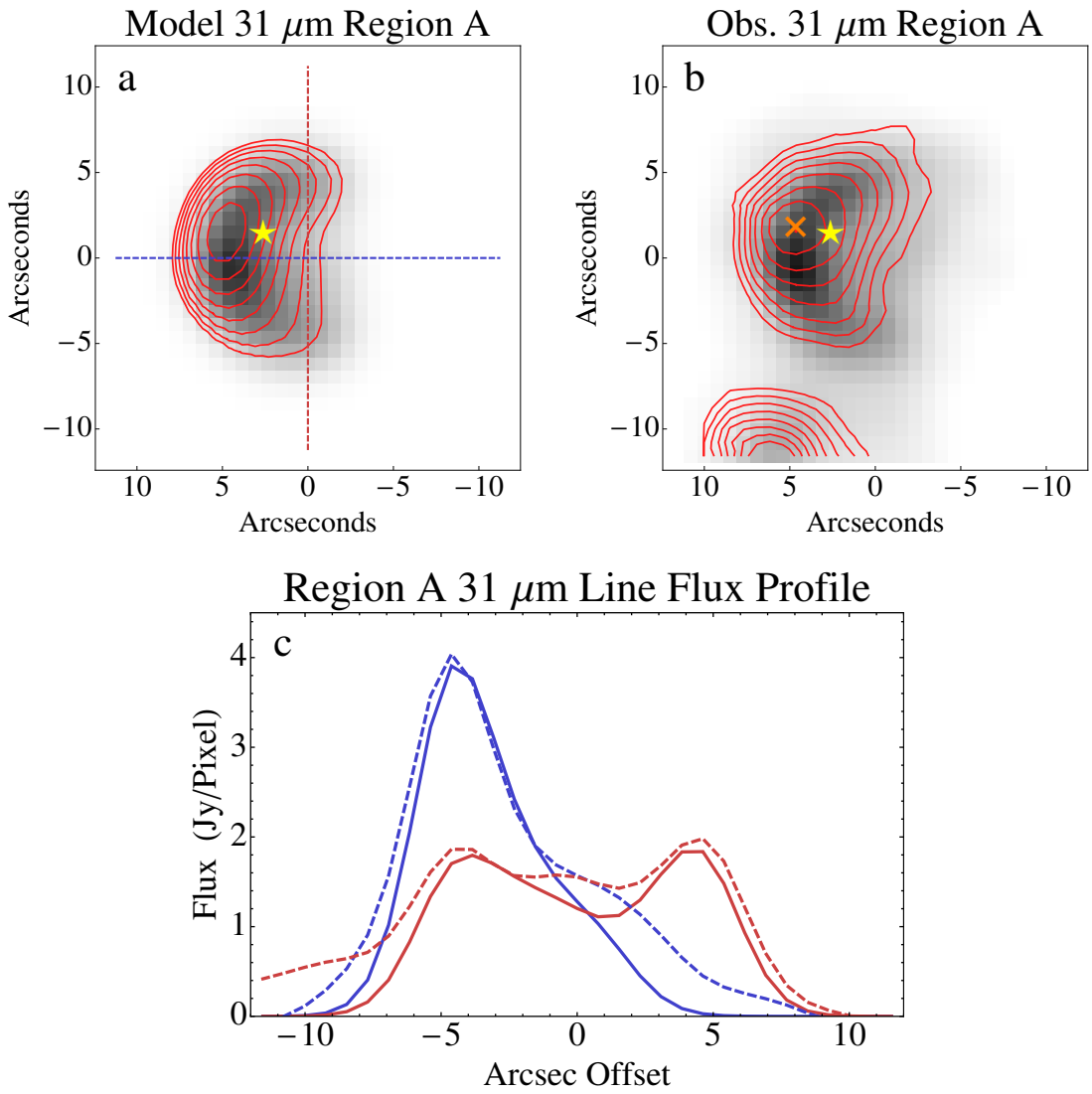

Figure 4.7: (a) 31 μm hemispherical shell emission model of region A overlaid with the position of the heating source and 19/31 model color temperature contours with levels corresponding to 100, 105, 110, 115, 120, 125, 130, and 135 K. (b) 31 μm observed flux map of region A overlaid with the position of the heating source and the observed 19/31 color temperature peak with contours corresponding to 100, 105, 110, 115, 120, 125, and 130 K. (c) Vertical (red) and horizontal (blue) flux cuts along the lines overlaid in (a) of both the observed (dashed) and model (solid) 31 μm emission.

Table 4.4. Region A Dust Emission Model Parameters

r_0 (pc)	Δt (pc)	n_S (cm^{-3})	L_* ($L_\odot$)	Δx	Δy	a (Å)
0.18	0.06	2100	2×10^5	-3″	+1″	100

Note. — r_0 is the inner radius, Δt is the thickness of the shell, n_S is the gas density in the southern half of the shell, L_* is the stellar luminosity of the heating source, Δx and Δy are the RA and dec displacement of heating source with respect to the center of the shell, and a is the size of the silicate grains in the shell.

Gas-to-Dust Mass Ratio

The dust mass of the HII regions and FIRS 1 can be derived from the DustEM models based on the number of LGs, VSGs, and PAHs required to fit the observed SEDs, although in general the dust mass is dominated by the LGs. Dust mass estimates for the HII regions are consistent with the mass derived from the observed integrated column densities of each region assuming a uniform distribution of 0.01 μm-sized grains. HII masses estimated from Paschen-α and 6 cm observations (Mills et al. 2011) give gas-to-dust mass ratios of 60, 72, 50, and 50 for Regions A, B, C, and D, respectively. These mass ratio estimates are slightly lower than the average value for the ISM ($\sim$ 100); however, the estimates are a lower limit since dust is heated at the molecular cloud interface outside the HII region.

4.4 Discussion

4.4.1 Dust Heating by Trapped Lyman-α

Lyman-α photons within dusty HII regions are rapidly absorbed and reemitted by hydrogen atoms until they are eventually absorbed by the dust grains. This dust heating mechanism is therefore proportional to the free-free emission from the region. The contribution to the infrared ($\sim 6 - 40$ μm) luminosity from the dust, L_α, can be expressed as

$$L_\alpha = \frac{S_{\nu,\mathrm{obs}}}{j_{\nu,ff}(n_e, T_e)} n_e^2 (\alpha_B - \alpha_{2s1}) h\nu_{Ly\alpha}\, 4\pi d^2, \tag{4.7}$$

where $S_{\nu,\mathrm{obs}}$ is the observed radio continuum flux, α_B is the type-B recombination coefficient, and α_{2s1} is the recombination coefficient for the two-photon process ($\alpha_{2s1} < \alpha_B$; Osterbrock & Ferland 2006). Given the electron temperatures ($\sim$ 6000 – 7000 K; Goss et al. 1985) and the 8.4 GHz flux ($\sim 0.1 - 0.6$ mJy; Mills et al. 2011) of the regions, the trapped Lyman-α heating contributes only $\sim 10\%$ of the total IR luminosity derived from the DustEM models (Tab. 4.2). If the dust heating from trapped Lyman-α were significant, the dust temperature would trace the density distribution and there would be a strong correlation between the color temperature and the optical depth maps (Fig. 4.4); such a correlation is not observed since the dust heating is dominated by the stellar radiation.

4.4.2 Region A: Bow Shock or Blister

The difference in the pressure between the ionized gas and the surrounding medium as well as high velocity ($\sim$ 2000 km/s) stellar winds from the ionizing star can play important roles in driving the expansion of HII regions. By comparing the rate of expansion from both mechanisms, Shull (1980) found that stellar winds dominate the dynamics over gas pressure if the following condition is satisfied

$$\left(\frac{L_w}{10^{36}\,\mathrm{ergs\,s^{-1}}}\right) > 0.33\left(\frac{Q_0}{10^{49}\,\mathrm{s^{-1}}}\right)^{3/2}\left(\frac{n_0}{10^5\,\mathrm{cm^{-3}}}\right)^{-1/3}, \tag{4.8}$$

where L_w is the mechanical power of the wind, and Q_0 is the number of ionizing photons emitted per second. For a star with a mass-loss rate of $10^{-6}\,M_\odot/yr$ and wind velocities of $\sim$ 2000 km/s, which are typical values for massive O-type stars, the mechanical power of the wind is $\sim 10^{36}$ erg/s. Assuming the values determined by Mills et al. (2011) of the four HII regions for n_e ($\sim$ 5000 – 20000 cm^{-3}) and Q_0 ($\sim 0.1 - 1 \times 10^{48}$ s^{-1}), Eq .4.8 is satisfied for all and their expansion is likely dominated by the stellar winds. This is consistent with the interpretation of the position-velocity data made by Yusef-Zadeh et al. (2010), where they conclude that the regions A - C are in fact bow shocks driven by stellar winds and the relative motion of the stars through the molecular cloud as opposed to "blisters" resulting from pressure driven flows at the surface of the molecular cloud.

The agreement between the dust emission model, location of the 19/37 color temperature peak, and DustEM model fits to the SEDs around the region strongly suggest that the heating source is displaced to the north east from the center of curvature. This northeast offset of the star is likely due to its motion

relative to the surrounding medium. The northeast motion of the star as well as its stellar winds are producing the bow shock that characterizes region A. This interpretation agrees with the steep radial velocity gradient at the east (Yusef-Zadeh et al. 2010), whereas a "blister" would produce the opposite signature with a steep velocity gradient at the west, which is the direction of the decreasing pressure gradient from the cloud to the ambient medium. By analyzing the kinematics of the bow shock driven into the 50 km/s molecular cloud, Yusef-Zadeh et al. (2010) infer that the star has a velocity of $\sim$ 30 km/s relative to the cloud towards the east and in our direction by an angle of 30°. The star may therefore have formed $\sim$ 2.5 pc in projection to the east of its current position given an age of $\sim 10^5$ yrs which is consistent with the location of western regions of the molecular cloud.

In a bow shock the stagnation radius, the distance from the star to where the momentum flux of the wind balances the ram pressure of the surrounding medium, can be expressed as

$$r_s \sim 0.04 \left(\frac{\dot{M}}{10^{-6}\, M_\odot\, \mathrm{yr}^{-1}}\right)^{1/2} \left(\frac{v_w}{2\times 10^3\, \mathrm{km\,s^{-1}}}\right)^{1/2} \left(\frac{n_0}{5\times 10^3\, \mathrm{cm^{-3}}}\right)^{-1/2} \left(\frac{v_*}{30\, \mathrm{km\,s^{-1}}}\right)^{-1} \mathrm{pc}. \tag{4.9}$$

Given the parameters assumed above for the values of $\dot{M}$, v_w, n_0, and v_*, the stagnation radius is $\sim$ 0.04 pc, which is roughly consistent the observed distance between the star and the location nearest to it on the shell ($\sim$ 0.07 pc). Since the thickness of the bow shock is unresolved, it is difficult to constrain the separation distance between the star and the shell to ±0.03 pc.

4.4.3 The Western "Ridges"

The decreasing 31/37 color temperatures of the ridges from east to west suggest they are heated by a source in the vicinity of region A. Assuming the dust in the ridges is composed of 0.1 μm-sized silicate grains and heated by the stellar radiation from the region A heating source at a distance of $\sqrt{2}$ times the projected distance, Eq. 4.5 can be used to predict equilibrium-heated dust temperatures of 60 and 47 K for ridges 2 and 3, respectively. The close agreement of the predicted dust temperatures with the color temperatures is strongly indicative that the ridges are heated by the same source. Interestingly, this excludes heating by the hot, young stars in the central cluster around Sgr A*, which is located $\sim$ 140″ to the southwest of ridge 3. At this distance with no intervening extinction, the central cluster would dominate the dust heating of ridge 3 and contribute significantly to heating dust in ridge 2. The additional heating from the central cluster ($L_{\rm cent} \sim 2 \times 10^7\ L_\odot$) would drive the dust temperatures of ridges 2 and 3 up to 65 K and 60 K, respectively. Since the difference between the observed 31/37 color temperatures of ridges 2 and 3 is much greater than the difference between these predicted dust temperatures it does not appear likely that the central cluster contributes significantly to heating the dust in the ridges. This is possibly due to the blockage of the UV light from the central cluster by the intervening presence of the dense circumnuclear disk (Latvakoski et al. 1999), or by the dense ridge of molecular gas int he 50 km/s cloud lying to the west of the HII regions.

Position-velocity maps of the ridges from Yusef-Zadeh et al. (2010) show that ridges 1 and 2, which are the only ridges in the slit, exhibit radial velocities of $\sim$ 50 km/s, identical to the median velocity of the molecular cloud. Given their

similar velocities to the molecular cloud and the increasing differential extinction from east to west, the ridges are likely elongated density enhancements on the surface of the 50 km/s molecular cloud heated and ionized by the radiation field of the region A heating source.

4.4.4 Heating Source Candidates

Regions A - C

The 1.87 and 1.90 μm images reveal that numerous point-sources appear coincident along the line of sight within each of the regions A - C (Fig. 4.8a), which imposes difficulties in trying to determine the single heating source of the regions. Estimates of the projected location and total luminosity of the heating sources from the dust SED models provide possible candidates in the 1.87 and 1.90 μm fields (Tab. 4.5). The stars enclosed in the orange, dotted square in Fig. 4.8a and b exhibit a 1.9 μm flux consistent within 20% of the 1.90 μm flux predicted by the heating sources of the DustEM SED models (assuming an O7 stellar atmosphere for the region A heating source and an O8.5 atmosphere for the region B and C heating source). These heating source candidates are also suggestively located nearby the observed 19/37 color temperature peak.

In the case of region A, the candidate lies only $\sim$ 0.05 pc away in projection from the approximated location of the heating source, which falls within the 20% error of the total luminosity in deriving the location. The source $\sim$ 0.2 pc to the southwest of the candidate for A may also be a viable heating source given its eastern displacement from the center of curvature; however, its flux at 1.90 μm is greater than twice the predicted value, which would imply dust

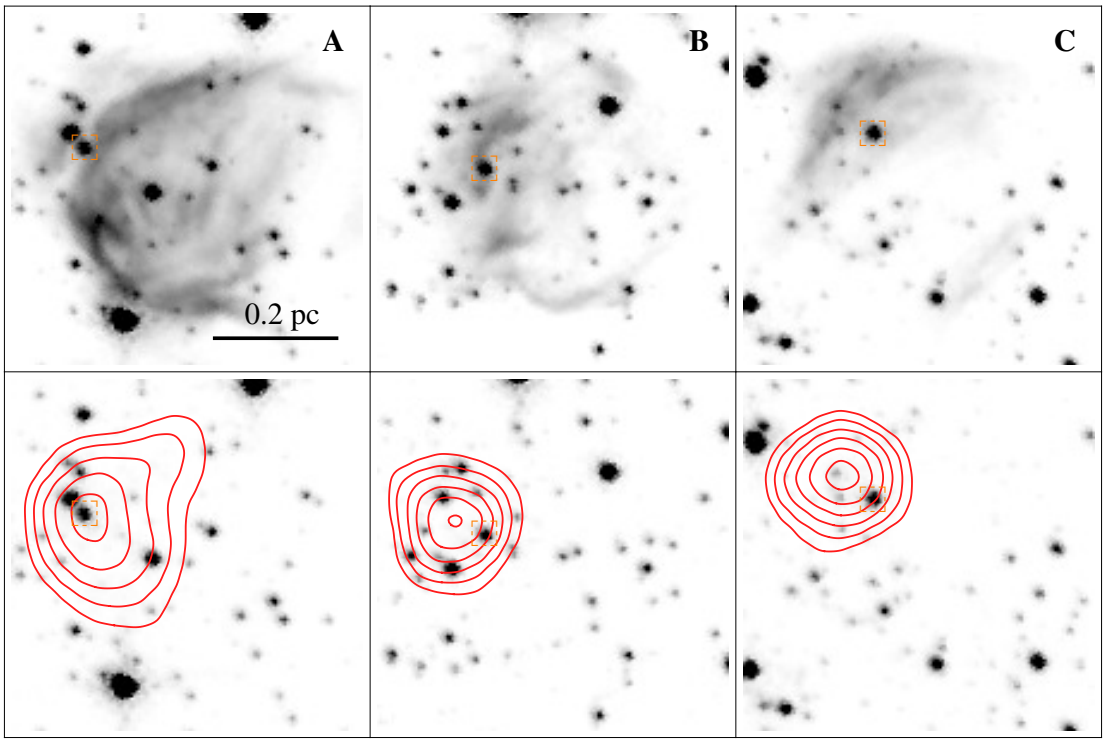

Figure 4.8: (top row) Paschen-α (1.87 μm) continuum image of regions A, B, and C with the heating source candidate marked in the orange, dotted squares. (bottom row) 1.90 μm image of the same fields as the top row with the same heating source candidates marked overlaid with the 19/37 color temperature contours. Color temperature contours correspond to 110, 115, 120, 125, and 130 K for A, 110, 115, 120, 125, 130, and 135 K for B, and 120, 125, 130, 135, 140, and 145 K for C.

temperatures ~ 15 K greater than the temperature determined for region A (T_d ~ 100 K). It is interesting that the region A candidate is the same source identified by Mills et al. (2011), who claim it may be linked to the "dark lane" structure at the northeastern edge that appears to separate the main shell of region A from a protrusion of emission at the northeast in Paschen-α. Radio images of the region exhibit an identical structure to that seen in Paschen-α (Mills et al. 2011).

Table 4.5. Dereddened Candidate Heating Source and Model 1.90 μm Fluxes

	A	B	C	D[a]
Candidate $F_{1.90}$ (Jy)	0.088	0.060	0.12	0.83
Model $F_{1.90}$ (Jy)	0.07	0.074	0.15	0.020
$A_{P\alpha}$	3.7	3.7	3.7	5.8

[a]The candidate flux is that of the heating source proposed by Mills et al. (2011)

Region D

A prominent point source appears coincident with the center of the western lobe of region D at 1.87 and 1.90 μm. The nature of this point source and its relation to region D has been disputed: Yusef-Zadeh et al. (2010) claim it is scattered light from a clump of gas and dust, and Mills et al. (2011) argue that it is actually the emission from the young stellar object that heats the region. Mills et al. (2011) claim that the source is unlikely a clump of dust and gas since that would imply enhanced emission from the ionized gas, which is not observed at Paschen-α or radio wavelengths. The 1.87/1.90 flux ratio also suggests the source has a purely stellar continuum (Mills et al. 2011). Our interpretation of this point source disagrees with both the claims of it being a gas and dust clump or the young stellar object based on its observed 1.90 μm flux. The 1.90 μm flux from this source is $\sim$ 40 times greater than the 1.90 μm flux predicted by the model heating source fitted to the region D SED, in which a stellar atmosphere of an O9 star (Mills et al. 2011) and an interstellar extinction value of $A_{P\alpha}$ = 5.8 (Mills et al. 2011) is assumed. Even if the amount of extinction towards the source was similar to that of regions A - C ($A_{P\alpha}$ = 3.7), the observed 1.90 μm flux would

still be almost an order of magnitude greater than predicted. The point source is therefore most likely a star that is coincident with region D along the line of sight.

Based on the heating source luminosity from the SED model and an interstellar extinction value of $A_{P\alpha} = 5.8$, the source should have a dereddened 1.90 μm flux of 0.02 Jy, whereas the bright point source has a dereddened 1.90 μm flux of 0.83 Jy. There is no 0.02 Jy source detected in the vicinity of region D at 1.90 μm; however, the emission may be confused with the point spread function of the bright point source.

4.5 Summary

We have presented and studied images of the warm dust emissions from the Sgr A East HII region complex G-0.02-0.07 at 19.7, 25.2, 31.5, and 37.1 μm and arrive at the following conclusions:

- The general dust morphology of the three resolved HII regions (A, B, and C) agrees with that of the ionized gas as detected at Paschen-α. However, in the case of region B, the ionized gas emission peaks several arcseconds interior to the dust emission peak at the northeast.

- Two faint IR sources, which are labeled as FIRS 1 and 2, are revealed at the FORCAST wavelengths. FIRS 1 is unresolved and has no ionized gas counterpart, and FIRS 2 is partially resolved (FWHM $\sim$ 5″ at 31.5 μm) and has a faint ionized gas counterpart observed in 6 cm emission (Zhao, Morris, & Goss 2014). FIRS 1 appears coincident with the southern edge of a long linear fila-

ment, which is seen at 31.5 and 37.1 μm as well as Paschen-α and seemingly traces the surface of the 50 km/s molecular cloud (Mills et al. 2011). Models fits to the SED of FIRS 1 performed with DustEM show that it is heavily extinguished relative the regions A, B, and C and must therefore be deeply embedded in the molecular cloud. The models indicate that the heating source must have a total luminosity of $\sim 1.6 \times 10^4$ $L_\odot$ assuming that it is equivalent to the total, integrated IR luminosity. DustEM models fail to constrain the FIRS 2 SED.

- Two of the three Paschen-α "ridges" to the west of region A as revealed by Mills et al. (2011) are detected and resolved at 31.5 and 37.1 μm. Based on the Paschen-α and 6 cm emission, there is a gradient of decreasing extinction west of ridge 1; however, the extinction estimates towards ridge 3 should be treated as an upper limit since there is non-thermal radio emission originating from the Sgr A East supernova remnant along the lines of sight. Given the extinction gradient as well as a gradient of decreasing 31/37 color temperature from east to west, the ridges are interpreted as elongated density enhancements on the far surface of the 50 km/s molecular cloud heated and ionized by the region A heating source.

- DustEM models fit to the SEDs of regions A - D and FIRS 1 reveal the luminosity of the heating sources as well as the mass of the emitting dust (Tab. 4.2). The fitted stellar luminosities are consistent with the required Lyman continuum flux as determined by Mills et al. (2011). The independently derived gas (Mills et al. 2011) and dust masses suggest a gas-to-dust mass ratio of $\sim$ 60, which we treat as a lower-limit since the emission from the dust traces deeper into the molecular cloud than the ionized gas emission. The presence of PAHs are required for the DustEM model fits to the SEDs of regions A - C.

- DustEM models fit to SEDs at north, east, and south locations in region A provide an estimate of the location of the heating source that is displaced northeast from the center of curvature (Fig. 4.7). A hemispherical shell emission model of region A with the heating source at the estimated location agrees with the observed dust emission. The northeast displacement of the heating source and the kinematic properties of the gas of the region (Yusef-Zadeh et al. 2012) indicate the region is a bow shock driven by stellar winds as opposed to being an expanding blister formed by the overpressure of the ionized gas.

- Candidate heating sources are identified for regions A - C in the Paschen-α continuum and 1.90 μm maps of the region that agree with the estimated flux of the heating sources as determined by the DustEM models. The positions of the candidate heating sources are also consistent with the locations 19/37 color temperature peaks.

- The bright point source coincident with the center of the western lobe of region D at 1.87 and 1.90 μm was claimed to be either the young stellar object heating and ionized the gas and dust (Mills et al. 2011) or scattered light from a clump of gas and dust (Yusef-Zadeh et al. 2010). The source appears stellar in nature; however, the observed 1.90 μm flux is $\sim$ 40 times greater than the flux predicted by heating source in the DustEM SED model. We therefore interpret this bright point source as a star coincident along the line of sight with region D.

CHAPTER 5

CONCLUSIONS AND FUTURE PLANS

5.1 Summary

In this thesis, I have used IR observations of dust emission as a diagnostic to study the properties of three regions containing hot, dusty features in the inner 60 pc of the GC. The primary focuses of this work has been characterizing the nature of the stellar heating sources, searching for evidence of star formation, and studying the interaction between the dust and the extreme environment of the GC.

Chapter 2 covers our work on the observations of the CNR, the clumpy ring of gas and dust surrounding Sgr A*. Given the high spatial resolution of the observations, we were able to resolve the thickness of the CNR and determine the depth of the PDR. The 19.7 μm map traces dust in the HII region of the CNR, while the 31.5 and 37.1 μm emission maps preferentially trace the PDR, which is displaced radially outward of the 19.7 μm emission. This result as well as the temperature gradient present in the 19/37 color temperature map provide strong confirmation of central, radiative heating by the massive, young stars in the central cluster near Sgr A *. The general azimuthal symmetry of the temperature map suggest that there is no active star formation occurring within the CNR, which is consistent with our density estimates that indicate the densities are more than an order of magnitude below the Roche limit at a distance of 1.4 pc from Sgr A* ($\sim 10^7$ cm^{-3}). The dust column density maps reveal the presence of $\sim$ 0.1 pc-sized dust clumps along the inner edge of the ring. They exhibit gas densities of $\sim 10^5$ cm^{-3}, which is too low to be gravitationally stable, and

should therefore shear out due to the differential velocity across the clump on timescales shorter than orbital period ($\lesssim 10^5$ yrs). The relatively short destruction timescales of these clumps is suggestive that the CNR is transient in nature.

Chapter 3 presents an interesting study on nature vs. nurture in the context of LBV nebulae in and near the Quintuplet Cluster, one of the three young, massive stellar clusters in the GC. The contrasting appearances of the dust emission from the Pistol and LBV3 nebulae are determined to be due to the difference in their proximity to the Quintuplet Cluster. The asymmetry of the Pistol nebula is explained by the deceleration of dust at the northern edge by its interaction with high-velocity winds from WR stars in the Quintuplet Cluster. The LBV3 nebula is much more circularly symmetric since it is located sufficiently far away from same WR stars that shape the Pistol nebula. Dust temperatures exhibited by the nebulae agree with this claim that the Quintuplet Cluster stars are only influencing the dust composing the Pistol nebula: the dust in the Pistol nebula is much too hot to be heated by a single, central LBV, whereas the temperatures are consistent for a single heating source for the LBV3 nebula. Our studies also reveal the similarity between the two nebulae. Both nebulae exhibit identical radii of $\sim$ 0.7 pc, which suggests they have similar dynamical timescales of $\sim 10^4$ yrs assuming an expansion velocity of 60 km/s. The gas-to-dust mass ratio of both nebulae is determined to be $\sim$ 300, and they are both likely composed of a distribution of very small silicate-type grains ($a \sim 10 - 60$ Å). These similarities provide a nice consistency with the interpretation of the LBVs as "twins" and that the contrasting appearance of their nebulae is primarily due to external influences.

Chapter 4 describes the observations of the dust emission from the Sgr A

East HII region, a region consisting of the most recent star formation in the inner 10 pc of the GC ($\sim 10^4 - 10^5$ yrs; Wood and Churchwell 1989, Yusef-Zadeh et al. 2010). In this work we model the SEDs of the HII regions and a faint IR source (FIRS 1) and characterize the properties of the emitting dust as well as the luminosity of the stellar heating source. The luminosities determined for the HII region heating sources ($\sim 0.5 - 2 \times 10^5\, L_\odot$) are consistent with the predicted ionizing flux derived from Paschen-α and 6 cm radio observations (Mills et al. 2011). Given the high spatial resolution of the observations, we utilized a technique to triangulate the position of the heating source within region A. A dust emission model of region A was generated with the heating source placed at the predicted location and was found to agree very well with the observed maps of the dust emission. Based on the color temperature maps and derived heating source luminosities, we identified heating source candidates for regions A, B, and C in the 1.87 and 1.90 μm maps of the Paschen-α and stellar continuum emission (Dong et al. 2011, Wang et al. 2010). Interestingly, we found that the bright point source coincident with region D is unlikely to be the heating source since its 1.90 μm flux is $\sim$ 40 times greater than the flux predicted by our SED models. For the SED modeling, we required the presence of both large and very small grains in all of the HII regions and FIRS 1. Additionally, the inclusion of PAHs was necessary for regions A, B, and C.

5.2 Further Studies of the Galactic Center

The work presented in this thesis reveals many interesting threads for possible follow-up observations and analysis. Such work is very important in solidifying our fundamental understanding of the Galactic center as well as other galaxies.

With better intuition on the nature of the GC, much more refined studies characterizing the star formation properties of other galaxies can be preformed. In this section, I discuss future work and possible extensions based on the results and analysis performed in Chapters 2, 3, and 4.

5.2.1 Pursuing the Clumps in the CNR

The presence of dust clumps at semi-regular intervals along the inner edge of the CNR is intriguing given the its proximity to Sgr A* and the strong tidal fields. The mechanism forming these clumps must therefore occur on timescales shorter than an orbital period ($\sim$ 80000 yrs). One possibility for the clump formation mechanism is Rossby wave instabilities (Lovelace et al. 1999), which are anticyclonic vortices that can appear azimuthally periodic within non-self-gravitating disks and trap dust. In addition to a theoretical analysis of the clump formation, we plan to utilize recently acquired SOFIA/FORCAST observations of the CNR tracing the PAH emission at 7.7 μm. Since the drag force is stronger for larger grains, an anticorrelation between the spatial distribution of PAHs and large grains might suggest that Rossby wave instabilities are the dominant mechanism of the clump formation. Studying the relative abundances of PAHs, very small grains, and large grains and comparing them to the relative abundances of other HII regions within the Galactic center may also provide insight into the age of the CNR.

5.2.2 Warm Dust in the Sickle HII Region

The SOFIA/FORCAST fields that capture the twin LBV nebulae also reveal the warm dust emission from the "Sickle" HII region, the ionized edge of a dense molecular cloud illuminated by the hot stars in the Quintuplet Cluster (Lang, Goss, & Wood 1997; Simpson et al. 1997). A study of the Sickle and its interaction with the Quintuplet Cluster would provide an interesting comparison with the interaction between the CNR and the central cluster since both structures are heated by the hot stars in a nearby cluster as well as encountering the stellar winds from the cluster. Future work on the Sickle would entail of studying its association with the Quintuplet Cluster and searching for evidence of star formation that may have been triggered by interactions with the cluster winds. Similar to the work on the Sgr A East HII regions, an analysis of the dust SEDs would provide estimates of the total cluster luminosity as well as an angular coverage factor.

5.2.3 Tracing Dust Processing in HII Regions

The Sgr A East HII regions provide an ideal target to study the processing of dust in the vicinity of a young hot star since regions A - D are associated with the same dense molecular cloud and exhibit a range of ages ($\sim 10^4 - 10^5$ yrs). In our analysis of the dust SEDs we were unable to robustly constrain the dust composition due to the lack of spectral information and the assumption of a three dust component distribution consisting of large grains, very small grains, and PAHs. Further observations with SOFIA/FORCAST in spectroscopy mode may be able to constrain the dust models and produce robust estimates of the

relative dust abundances of each region. Comparing the relative dust abundances across the regions could reveal evidence of dust processing.

5.2.4 Characterizing Dusty Nebulae around Massive Evolved Stars

Our results from the observations of the twin LBV nebulae motivate further studies of LBV and Wolf-Rayet (WR) nebulae found throughout the Galaxy. Such nebulae might be characterized as "Pistol-like" if they are found near their birth cluster that also dominates the heating of the dust, or as "LBV3-like" if they are isolated and primarily illuminated by the central star. A survey of LBV and WR nebulae could provide insight into this relatively short, post main-sequence evolutionary phase of these high initial mass stars. Analysis of the dust emission from these nebulae can produce estimates of mass-loss history, constrain the dust composition, and reveal information on how their birth clusters may be influencing their appearance or evolution. Unfortunately, the sensitivity of SOFIA/FORCAST is too low to perform follow-up observations of the LBV and WR nebulae identified by Spitzer/MIPS and Spitzer/IRAC (Wachter et al. 2010). Any further observations of such sources in the mid to far-IR will likely have to wait for the launch of JWST.

5.2.5 Warm Dust Survey of the Galactic Center

Despite all of the work on the prominent IR dust emission sources at the GC presented in this thesis, there remains a plethora of interesting regions to explore

with the capabilities of SOFIA/FORCAST. A rather ambitious future project would be to perform a far-IR survey of the inner $\sim$ 100 pc of the GC with SOFIA/FORCAST and apply the same dust emission analysis techniques utilized in this thesis. Surveys of the GC have been completed at submillimeter and millimeter wavelengths (Pierce-Price et al. 2000; Bally et al. 2010) as well as at near to mid-IR wavelengths (Stolovy et al. 2006). 24 μm observations of the GC were attempted by Spitzer/MIPS; however, the images are mostly saturated. A survey with SOFIA/FORCAST at 19, 25, 31, and 37 μm would therefore provide results that are complementary to the previous surveys in addition to producing images with better spatial resolution than Spitzer. Submillimeter and millimeter maps are primarily sensitive to cool ($\sim$ 40 K) dust and do not trace the regions where a majority of the dust heating by stellar sources is occurring. In the opposite sense, the near to mid-IR observations mostly trace small dust grains that are transiently heated and consequently appear very hot ($\gtrsim$ 200 K). Far-IR observations can reveal sources with warm dust ($\sim$ 100 K) such as LBV nebulae, embedded protostars, large-scale shocks, compact HII regions, planetary nebulae, and supernova remnants.

BIBLIOGRAPHY

J. D. Adams, T. L. Herter, G. E. Gull, J. Schoenwald, C. P. Henderson, L. D. Keller, J. M. De Buizer, G. J. Stacey, and T. Nikola. FORCAST: a first light facility instrument for SOFIA. In *Society of Photo-Optical Instrumentation Engineers (SPIE) Conference Series*, volume 7735 of *Society of Photo-Optical Instrumentation Engineers (SPIE) Conference Series*, July 2010. doi: 10.1117/12.857049.

J. D. Adams, T. L. Herter, G. E. Gull, J. Schoenwald, C. P. Henderson, L. D. Keller, J. M. De Buizer, G. J. Stacey, T. Nikola, W. D. Vacca, L. Hirsch, J. Wang, and L. A. Helton. The FORCAST mid-infrared facility instrument and in-flight performance on SOFIA. In *Society of Photo-Optical Instrumentation Engineers (SPIE) Conference Series*, volume 8446 of *Society of Photo-Optical Instrumentation Engineers (SPIE) Conference Series*, Sept. 2012. doi: 10.1117/12.926600.

B. Balick and R. L. Brown. Intense sub-arcsecond structure in the galactic center. *ApJ*, 194:265–270, Dec. 1974. doi: 10.1086/153242.

J. Bally, J. Aguirre, C. Battersby, E. T. Bradley, C. Cyganowski, D. Dowell, M. Drosback, M. K. Dunham, N. J. Evans, II, A. Ginsburg, J. Glenn, P. Harvey, E. Mills, M. Merello, E. Rosolowsky, W. Schlingman, Y. L. Shirley, G. S. Stringfellow, J. Walawender, and J. Williams. The Bolocam Galactic Plane Survey: λ = 1.1 and 0.35 mm Dust Continuum Emission in the Galactic Center Region. *ApJ*, 721:137, Sept. 2010. doi: 10.1088/0004-637X/721/1/137.

E. E. Becklin, I. Gatley, and M. W. Werner. Far-infrared observations of Sagittarius A - The luminosity and dust density in the central parsec of the Galaxy. *ApJ*, 258:135–142, July 1982. doi: 10.1086/160060.

R. A. Bernstein, W. L. Freedman, and B. F. Madore. The First Detections of the

Extragalactic Background Light at 3000, 5500, and 8000 . I. Results. *ApJ*, 571: 56–84, May 2002. doi: 10.1086/339422.

J. A. Cardelli, G. C. Clayton, and J. S. Mathis. The relationship between infrared, optical, and ultraviolet extinction. *ApJ*, 345:245–256, Oct. 1989. doi: 10.1086/167900.

J. E. Chiar and A. G. G. M. Tielens. Pixie Dust: The Silicate Features in the Diffuse Interstellar Medium. *ApJ*, 637:774–785, Feb. 2006. doi: 10.1086/498406.

M. H. Christopher, N. Z. Scoville, S. R. Stolovy, and M. S. Yun. HCN and HCO^+ Observations of the Galactic Circumnuclear Disk. *ApJ*, 622:346–365, Mar. 2005. doi: 10.1086/427911.

J. S. Clark, V. M. Larionov, and A. Arkharov. On the population of galactic Luminous Blue Variables. *A&A*, 435:239–246, May 2005. doi: 10.1051/0004-6361:20042563.

M. Compiègne, L. Verstraete, A. Jones, J.-P. Bernard, F. Boulanger, N. Flagey, J. Le Bourlot, D. Paradis, and N. Ysard. The global dust SED: tracing the nature and evolution of dust with DustEM. *A&A*, 525:A103, Jan. 2011. doi: 10.1051/0004-6361/201015292.

J. A. Davidson, M. W. Werner, X. Wu, D. F. Lester, P. M. Harvey, M. Joy, and M. Morris. The luminosity of the Galactic center. *ApJ*, 387:189–211, Mar. 1992. doi: 10.1086/171071.

F. X. Desert, F. Boulanger, and S. N. Shore. Grain temperature fluctuations - A key to infrared spectra. *A&A*, 160:295–300, May 1986.

H. Dong, Q. D. Wang, A. Cotera, S. Stolovy, M. R. Morris, J. Mauerhan, E. A. Mills, G. Schneider, D. Calzetti, and C. Lang. Hubble Space Telescope Paschen

α survey of the Galactic Centre: data reduction and products. *MNRAS*, 417: 114–135, Oct. 2011. doi: 10.1111/j.1365-2966.2011.19013.x.

B. T. Draine. Interstellar Dust Grains. *ARAA*, 41:241–289, 2003. doi: 10.1146/annurev.astro.41.011802.094840.

B. T. Draine. *Physics of the Interstellar and Intergalactic Medium*. 2011.

B. T. Draine and N. Anderson. Temperature fluctuations and infrared emission from interstellar grains. *ApJ*, 292:494–499, May 1985. doi: 10.1086/163181.

B. T. Draine and H. M. Lee. Optical properties of interstellar graphite and silicate grains. *ApJ*, 285:89–108, Oct. 1984. doi: 10.1086/162480.

B. T. Draine and A. Li. Infrared Emission from Interstellar Dust. I. Stochastic Heating of Small Grains. *ApJ*, 551:807–824, Apr. 2001. doi: 10.1086/320227.

M. Etxaluze, H. A. Smith, V. Tolls, A. A. Stark, and E. González-Alfonso. The Galactic Center in the Far-infrared. *AJ*, 142:134, Oct. 2011. doi: 10.1088/0004-6256/142/4/134.

D. F. Figer, I. S. McLean, and M. Morris. Two New Wolf-Rayet Stars and a Luminous Blue Variable Star in the Quintuplet (AFGL 2004) near the Galactic Center. *ApJL*, 447:L29, July 1995. doi: 10.1086/309551.

D. F. Figer, F. Najarro, M. Morris, I. S. McLean, T. R. Geballe, A. M. Ghez, and N. Langer. The Pistol Star. *ApJ*, 506:384–404, Oct. 1998. doi: 10.1086/306237.

D. F. Figer, I. S. McLean, and M. Morris. Massive Stars in the Quintuplet Cluster. *ApJ*, 514:202–220, Mar. 1999a. doi: 10.1086/306931.

D. F. Figer, M. Morris, T. R. Geballe, R. M. Rich, E. Serabyn, I. S. McLean, R. C. Puetter, and A. Yahil. High-Resolution Infrared Imaging and Spectroscopy of

the Pistol Nebula: Evidence for Ejection. *ApJ*, 525:759–771, Nov. 1999b. doi: 10.1086/307927.

D. F. Figer, F. Najarro, D. Gilmore, M. Morris, S. S. Kim, E. Serabyn, I. S. McLean, A. M. Gilbert, J. R. Graham, J. E. Larkin, N. A. Levenson, and H. I. Teplitz. Massive Stars in the Arches Cluster. *ApJ*, 581:258–275, Dec. 2002. doi: 10.1086/344154.

T. K. Fritz, S. Gillessen, K. Dodds-Eden, D. Lutz, R. Genzel, W. Raab, T. Ott, O. Pfuhl, F. Eisenhauer, and F. Yusef-Zadeh. Line Derived Infrared Extinction toward the Galactic Center. *ApJ*, 737:73, Aug. 2011. doi: 10.1088/0004-637X/737/2/73.

T. R. Geballe, K. Krisciunas, T. J. Lee, I. Gatley, R. Wade, W. D. Duncan, R. Garden, and E. E. Becklin. Observations of broad helium and hydrogen lines in the very center of the galaxy. *ApJ*, 284:118–125, Sept. 1984. doi: 10.1086/162390.

T. R. Geballe, F. Najarro, and D. F. Figer. A Second Luminous Blue Variable in the Quintuplet Cluster. *ApJL*, 530:L97–L101, Feb. 2000. doi: 10.1086/312501.

R. Genzel. The Circumnuclear Disk (review). In M. Morris, editor, *The Center of the Galaxy*, volume 136 of *IAU Symposium*, page 393, 1989.

R. Genzel, D. M. Watson, C. H. Townes, H. L. Dinerstein, D. Hollenbach, D. F. Lester, M. Werner, and J. W. V. Storey. Far-infrared spectroscopy of the galactic center - Neutral and ionized gas in the central 10 parsecs of the Galaxy. *ApJ*, 276:551–559, Jan. 1984. doi: 10.1086/161644.

R. Genzel, M. K. Crawford, C. H. Townes, and D. M. Watson. The neutral-

gas disk around the galactic center. *ApJ*, 297:766–786, Oct. 1985. doi: 10.1086/163574.

A. M. Ghez, S. Salim, N. N. Weinberg, J. R. Lu, T. Do, J. K. Dunn, K. Matthews, M. R. Morris, S. Yelda, E. E. Becklin, T. Kremenek, M. Milosavljevic, and J. Naiman. Measuring Distance and Properties of the Milky Way's Central Supermassive Black Hole with Stellar Orbits. *ApJ*, 689:1044–1062, Dec. 2008. doi: 10.1086/592738.

S. Gillessen, F. Eisenhauer, S. Trippe, T. Alexander, R. Genzel, F. Martins, and T. Ott. Monitoring Stellar Orbits Around the Massive Black Hole in the Galactic Center. *ApJ*, 692:1075–1109, Feb. 2009. doi: 10.1088/0004-637X/692/2/1075.

R. Guesten, R. Genzel, M. C. H. Wright, D. T. Jaffe, J. Stutzki, and A. I. Harris. Aperture synthesis observations of the circumnuclear ring in the Galactic center. *ApJ*, 318:124–138, July 1987. doi: 10.1086/165355.

P. Guhathakurta and B. T. Draine. Temperature fluctuations in interstellar grains. I - Computational method and sublimation of small grains. *ApJ*, 345: 230–244, Oct. 1989. doi: 10.1086/167899.

T. L. Herter, J. D. Adams, J. M. De Buizer, G. E. Gull, J. Schoenwald, C. P. Henderson, L. D. Keller, T. Nikola, G. Stacey, and W. D. Vacca. First Science Observations with SOFIA/FORCAST: The FORCAST Mid-infrared Camera. *ApJL*, 749:L18, Apr. 2012. doi: 10.1088/2041-8205/749/2/L18.

W. T. Irons, J. H. Lacy, and M. J. Richter. Ionized Gas in the Galactic Center: New Observations and Interpretation. *ApJ*, 755:90, Aug. 2012. doi: 10.1088/0004-637X/755/2/90.

Z. Ivezic and M. Elitzur. Self-similarity and scaling behaviour of infrared emission from radiatively heated dust - I. Theory. *MNRAS*, 287:799–811, June 1997.

J. M. Jackson, N. Geis, R. Genzel, A. I. Harris, S. Madden, A. Poglitsch, G. J. Stacey, and C. H. Townes. Neutral gas in the central 2 parsecs of the Galaxy. *ApJ*, 402:173–184, Jan. 1993. doi: 10.1086/172120.

C. S. Kochanek. The Astrophysical Implications of Dust Formation during the Eruptions of Hot, Massive Stars. *ApJ*, 743:73, Dec. 2011. doi: 10.1088/0004-637X/743/1/73.

A. Krabbe, R. Genzel, A. Eckart, F. Najarro, D. Lutz, M. Cameron, H. Kroker, L. E. Tacconi-Garman, N. Thatte, L. Weitzel, S. Drapatz, T. Geballe, A. Sternberg, and R. Kudritzki. The Nuclear Cluster of the Milky Way: Star Formation and Velocity Dispersion in the Central 0.5 Parsec. *ApJL*, 447:L95, July 1995. doi: 10.1086/309579.

R. L. Kurucz. Model Atmospheres (Kurucz, 1979). *VizieR Online Data Catalog*, 6039:0, Oct. 1993.

J. H. Lacy, C. H. Townes, T. R. Geballe, and D. J. Hollenbach. Observations of the motion and distribution of the ionized gas in the central parsec of the Galaxy. II. *ApJ*, 241:132–146, Oct. 1980. doi: 10.1086/158324.

J. H. Lacy, J. M. Achtermann, and E. Serabyn. Galactic center gasdynamics - A one-armed spiral in a Keplerian disk. *ApJL*, 380:L71–L74, Oct. 1991. doi: 10.1086/186176.

H. J. G. L. M. Lamers, A. Nota, N. Panagia, L. J. Smith, and N. Langer. Chemical Composition and Origin of Nebulae around Luminous Blue Variables. *ApJ*, 551:764–780, Apr. 2001. doi: 10.1086/320229.

C. C. Lang, W. M. Goss, and O. S. Wood. VLA H92α and H115β Recombination Line Observations of the Galactic Center H II Regions: The Sickle (G0.18-0.04) and the Pistol (G0.15-0.05). *ApJ*, 474:275–291, Jan. 1997.

N. Langer, W.-R. Hamann, M. Lennon, F. Najarro, A. W. A. Pauldrach, and J. Puls. Towards an understanding of very massive stars. A new evolutionary scenario relating O stars, LBVs and Wolf-Rayet stars. *A&A*, 290:819–833, Oct. 1994.

H. M. Latvakoski, G. J. Stacey, G. E. Gull, and T. L. Hayward. Kuiper Widefield Infrared Camera Far-Infrared Imaging of the Galactic Center: The Circumnuclear Disk Revealed. *ApJ*, 511:761–773, Feb. 1999. doi: 10.1086/306689.

R. M. Lau, T. L. Herter, M. R. Morris, E. E. Becklin, and J. D. Adams. SOFIA/FORCAST Imaging of the Circumnuclear Ring at the Galactic Center. *ApJ*, 775:37, Sept. 2013. doi: 10.1088/0004-637X/775/1/37.

R. M. Lau, T. L. Herter, M. R. Morris, and J. D. Adams. Nature versus Nurture: Luminous Blue Variable Nebulae in and near Massive Stellar Clusters at the Galactic Center. *ApJ*, 785:120, Apr. 2014. doi: 10.1088/0004-637X/785/2/120.

K. Y. Lo and M. J. Claussen. High-resolution observations of ionized gas in central 3 parsecs of the Galaxy - Possible evidence for infall. *Nature*, 306:647–651, Dec. 1983. doi: 10.1038/306647a0.

R. V. E. Lovelace, H. Li, S. A. Colgate, and A. F. Nelson. Rossby Wave Instability of Keplerian Accretion Disks. *ApJ*, 513:805–810, Mar. 1999. doi: 10.1086/306900.

D. Lutz. ISO observations of the Galactic Centre. In P. Cox and M. Kessler,

editors, *The Universe as Seen by ISO*, volume 427 of *ESA Special Publication*, page 623, Mar. 1999.

S. Martín, J. Martín-Pintado, M. Montero-Castaño, P. T. P. Ho, and R. Blundell. Surviving the hole. I. Spatially resolved chemistry around Sagittarius A*. *A&A*, 539:A29, Mar. 2012. doi: 10.1051/0004-6361/201117268.

J. C. Mauerhan, M. R. Morris, A. Cotera, H. Dong, Q. D. Wang, S. R. Stolovy, C. Lang, and I. S. Glass. Discovery of a Luminous Blue Variable with an Ejection Nebula Near the Quintuplet Cluster. *ApJL*, 713:L33–L36, Apr. 2010. doi: 10.1088/2041-8205/713/1/L33.

A. Moneti, J. A. D. L. Blommaert, F. Najarro, D. Figer, and S. Stolovy. Spectroscopy of the Pistol and Quintuplet stars in the Galactic centre. In P. Cox and M. Kessler, editors, *The Universe as Seen by ISO*, volume 427 of *ESA Special Publication*, page 723, Mar. 1999.

A. Moneti, S. Stolovy, J. A. D. L. Blommaert, D. F. Figer, and F. Najarro. Mid-infrared imaging and spectroscopy of the enigmatic cocoon stars in the Quintuplet Cluster. *A&A*, 366:106–120, Jan. 2001. doi: 10.1051/0004-6361:20000192.

M. Montero-Castaño, R. M. Herrnstein, and P. T. P. Ho. Gas Infall Toward Sgr A* from the Clumpy Circumnuclear Disk. *ApJ*, 695:1477–1494, Apr. 2009. doi: 10.1088/0004-637X/695/2/1477.

M. Morris and E. Serabyn. The Galactic Center Environment. *ARAA*, 34:645–702, 1996. doi: 10.1146/annurev.astro.34.1.645.

F. Najarro, D. F. Figer, D. J. Hillier, T. R. Geballe, and R. P. Kudritzki. Metallicity in the Galactic Center: The Quintuplet Cluster. *ApJ*, 691:1816–1827, Feb. 2009. doi: 10.1088/0004-637X/691/2/1816.

A. Nota, M. Livio, M. Clampin, and R. Schulte-Ladbeck. Nebulae around Luminous Blue Variables: A Unified Picture. *ApJ*, 448:788, Aug. 1995. doi: 10.1086/176006.

D. E. Osterbrock and G. J. Ferland. *Astrophysics of gaseous nebulae and active galactic nuclei*. 2006.

A. Pasquali, F. Comerón, and A. Nota. The birth-cluster of the galactic luminous blue variable WRA 751. *A&A*, 448:589–596, Mar. 2006. doi: 10.1051/0004-6361:20053977.

B. Pegourie and R. Papoular. The optical properties of dust in the mid-IR silicate bands. *A&A*, 142:451–460, Jan. 1985.

D. Pierce-Price, J. S. Richer, J. S. Greaves, W. S. Holland, T. Jenness, A. N. Lasenby, G. J. White, H. E. Matthews, D. Ward-Thompson, W. R. F. Dent, R. Zylka, P. Mezger, T. Hasegawa, T. Oka, A. Omont, and G. Gilmore. A Deep Submillimeter Survey of the Galactic Center. *ApJL*, 545:L121–L125, Dec. 2000. doi: 10.1086/317884.

M. J. Reid. The distance to the center of the Galaxy. *ARAA*, 31:345–372, 1993. doi: 10.1146/annurev.aa.31.090193.002021.

M. J. Reid and A. Brunthaler. The Proper Motion of Sagittarius A*. II. The Mass of Sagittarius A*. *ApJ*, 616:872–884, Dec. 2004. doi: 10.1086/424960.

M. A. Requena-Torres, R. Güsten, A. Weiß, A. I. Harris, J. Martín-Pintado, J. Stutzki, B. Klein, S. Heyminck, and C. Risacher. GREAT confirms transient nature of the circum-nuclear disk. *A&A*, 542:L21, June 2012. doi: 10.1051/0004-6361/201219068.

G. H. Rieke, M. J. Rieke, and A. E. Paul. Origin of the excitation of the galactic center. *ApJ*, 336:752–761, Jan. 1989. doi: 10.1086/167047.

D. A. Roberts and W. M. Goss. Multiconfiguration VLA H92-alpha observations of Sagittarius A West at 1 arcsecond resolution. *ApJS*, 86:133–152, May 1993. doi: 10.1086/191773.

P. F. Roche and D. K. Aitken. An investigation of the interstellar extinction. I - Towards dusty WC Wolf-Rayet stars. *MNRAS*, 208:481–492, June 1984.

F. Salgado, O. Berné, J. D. Adams, T. L. Herter, G. Gull, J. Schoenwald, L. D. Keller, J. M. De Buizer, W. D. Vacca, E. E. Becklin, R. Y. Shuping, A. G. G. M. Tielens, and H. Zinnecker. First Science Results from SOFIA/FORCAST: The Mid-infrared View of the Compact H II Region W3A. *ApJL*, 749:L21, Apr. 2012. doi: 10.1088/2041-8205/749/2/L21.

E. Serabyn and R. Guesten. The H II region G0.18-0.04: ionization of a molecular cloud by impact with a strong magnetic field. *A&A*, 242:376–387, Feb. 1991.

E. Serabyn and J. H. Lacy. Forbidden NE II observations of the galactic center - Evidence for a massive block hole. *ApJ*, 293:445–458, June 1985. doi: 10.1086/163250.

E. Serabyn, J. H. Lacy, C. H. Townes, and R. Bharat. High-resolution forbidden NE II observations of the ionized filaments in the Galactic center. *ApJ*, 326: 171–185, Mar. 1988. doi: 10.1086/166078.

J. P. Simpson. IRAS low-resolution spectral observations of the 10 and 18 micron silicate emission feature. *ApJ*, 368:570–579, Feb. 1991. doi: 10.1086/169721.

J. P. Simpson, S. W. J. Colgan, A. S. Cotera, E. F. Erickson, M. R. Haas, M. Morris,

and R. H. Rubin. Infrared Observations of G0.18-0.04. *ApJ*, 487:689–703, Oct. 1997.

G. J. Stacey, T. L. Hayward, H. Latvakoski, and G. E. Gull. KWIC: a wide-field mid-infrared array camera/spectrometer for the KAO. In A. M. Fowler, editor, *Infrared Detectors and Instrumentation*, volume 1946 of *Society of Photo-Optical Instrumentation Engineers (SPIE) Conference Series*, pages 238–248, Oct. 1993.

C. M. Telesco, J. A. Davidson, and M. W. Werner. 10–30 Micron Maps of the Central 5 Parsecs of the Galaxy: Heating of the Cavity and Neutral Gas Disk. *ApJ*, 456:541, Jan. 1996. doi: 10.1086/176678.

A. G. G. M. Tielens, C. F. McKee, C. G. Seab, and D. J. Hollenbach. The physics of grain-grain collisions and gas-grain sputtering in interstellar shocks. *ApJ*, 431:321–340, Aug. 1994. doi: 10.1086/174488.

S. Wachter, J. C. Mauerhan, S. D. Van Dyk, D. W. Hoard, S. Kafka, and P. W. Morris. A Hidden Population of Massive Stars with Circumstellar Shells Discovered with the Spitzer Space Telescope. *AJ*, 139:2330–2346, June 2010. doi: 10.1088/0004-6256/139/6/2330.

Q. D. Wang, H. Dong, A. Cotera, S. Stolovy, M. Morris, C. C. Lang, M. P. Muno, G. Schneider, and D. Calzetti. HST/NICMOS Paschen-α Survey of the Galactic Centre: Overview. *MNRAS*, 402:895–902, Feb. 2010. doi: 10.1111/j.1365-2966.2009.15973.x.

D. O. S. Wood and E. Churchwell. The morphologies and physical properties of ultracompact H II regions. *ApJS*, 69:831–895, Apr. 1989. doi: 10.1086/191329.

F. Yusef-Zadeh and M. Morris. Structural details of the Sagittarius A complex - Evidence for a large-scale poloidal magnetic field in the Galactic center region. *ApJ*, 320:545–561, Sept. 1987. doi: 10.1086/165572.

J.-H. Zhao, M. R. Morris, W. M. Goss, and T. An. Dynamics of Ionized Gas at the Galactic Center: Very Large Array Observations of the Three-dimensional Velocity Field and Location of the Ionized Streams in Sagittarius A West. *ApJ*, 699:186–214, July 2009. doi: 10.1088/0004-637X/699/1/186.